OPTICAL AND MAGNETO-OPTICAL PROPERTIES OF RARE-EARTH IONS IN NON-CRYSTALLINE OXIDES

Koji FUJITA

1999

Contents

5   Magneto-optical properties of Eu^{2+} ions in glasses   153

General introduction

Glasses containing rare-earth (RE) ions play an important role in the field of optoelectronics. The interest in the study on RE-containing glasses has grown rapidly with the development of lasers at the beginning of the 1960s. Many attempts have been made to control the radiative and non-radiative properties of bulk glasses and fibers doped with RE ions, and to apply these materials to gain media for lasers. Nd^{3+}:glass lasers [1] and Er^{3+}-doped fiber amplifiers [2] are two examples of the success of the use of doped glass to perform an optical function. Another resurgence of interest and activity began in the late 1970s following the application of the technique of laser spectroscopy to the study of glasses containing RE ions. The advent of high-resolution or nonlinear laser spectroscopy responds to the search for glass materials with new optical functions such as hole-burning memories and upconversion lasers for high-density optical storage systems, which are required for high-speed and high-density data processing in today's information-oriented society.

In addition to the technological promise, the high-resolution laser technique is also useful for scientific studies on RE-doped glasses. The major goal is to overcome the resolution limit imposed by the inhomogeneous linewidth originating from structural disorder. By eliminating the influence of the inhomogeneous linewidth, it is possible to obtain information on the homogeneous linewidth arising from the interaction of a RE ion with its surrounding amorphous host. Consequently, considerable work has been carried out in the last year to understand the dynamics of glasses, especially at low temperatures.

It has been found that the temperature dependence and magnitude of homogeneous linewidth are very different from those in crystals below $\sim$40 K. The first optical measurements on inorganic glasses doped with RE ions at low temperatures were performed between 10 and 90 K for the $4f-4f$ transition of Eu^{3+} in a silicate glass by means of fluorescence line-narrowing (FLN) spectroscopy [3]. The results revealed the homogeneous linewidth which was more than one order of magnitude larger than in crystals at about 80 K, and its temperature dependence was found to be quadratic, instead of T^7 in crystals. Such a T^2 -dependence was also found for other RE -doped inorganic glasses between 10 and 800 K using the FLN technique [4–8]. Thus, special attention has been paid to the homogeneous linewidth for RE -doped glasses at low temperatures.

The most common oxidation state of RE ions is usually a trivalent one. The $4f-4f$ transitions of trivalent RE -doped glasses bring about interesting optical properties and functions as described above. On the other hand, some RE ions such as Sm, Eu and Yb can be present as a divalent oxidation state as well. In contrast to the trivalent RE ions, the divalent RE ions in solids manifest unique characteristics as follows.

- The change of the valence state occurs easily by irradiation with visible light, ultraviolet light, X-ray and γ-ray.

- The $4f-5d$ transition appears in the visible region for divalent RE ions, although it lies in the ultraviolet region for trivalent RE ions. The $4f-5d$ transition is parity-allowed, and therefore, the oscillator strength is much stronger than that of parity-forbidden $4f-4f$ transition. Furthermore, the energy levels of $5d$ orbitals are largely influenced by the ligand field compared with those of $4f$ orbitals.

Such features of divalent RE ions give rise to the possibility of inducing novel

and striking optical functions.

A typical example of utilizing the change of the valence state of divalent RE ions is persistent spectral hole burning due to photoionization. This phenomenon occurs when a frequency-selected subset of optical absorption band is modified by the photoionization removal of RE ions, as was first shown in $CaF_2 : Sm^{2+}$ [10] and subsequently in $BaClF : Sm^{2+}$ [11]. In these materials, however, the narrow inhomogeneous linewidth makes it impossible to burn hole at high temperatures because the hole linewidth becomes wider and hence comparable to the inhomogeneous linewidth as the temperature is raised. In order to design materials which exhibit the large inhomogeneous linewidth, many studies have been extensively performed for Sm^{2+} -doped mixed crystals and glasses, and room-temperature persistent spectral hole burning has been successfully observed for some of the mixed crystals and glasses [12–17]. In particular, the large inhomogeneous linewidth in glasses is advantageous to application of hole-burning materials to frequency-domain optical memories.

On the other hand, an interesting phenomenon associated with the $4f - 5d$ transition is magneto-optical properties such as Faraday effect, which is caused by the interaction between the electric field of light and the magnetization. The Faraday effect in glasses containing RE ions generally takes place as a result of the orientation of magnetic dipole under an applied dc magnetic field. The parity-allowed transitions between $4f$ and $5d$ levels of RE ions, which bring about the Faraday effect, occur in the range of the visible to ultraviolet wavelength. Consequently, these glasses become useful as an optical isolator, an optical modulator, a sensor of electric current, and a sensor of magnetic field which work in the visible light region. More recently, a blue laser diode composed of a (Ga,In)N semiconductor has been developed successfully [18]. The development of the blue laser diode will increase a demand for optical or magneto-optical devices which operate effectively in the short wavelength

region. Glasses containing divalent RE ions become promising materials for such a purpose because of the high transparency as well as the large Faraday rotation angle in the visible region.

As described above, the glasses containing RE ions exhibit interesting optical and magneto-optical properties from both fundamental and practical standpoints. However, there exist some unresolved problems which result from the inhomogeneous properties or structural disorders in glasses. For persistent spectral hole burning in glasses, not only the condition for the possibility of the persistent hole formation at high temperatures but also the mechanism which affects hole width and its temperature dependence at low temperatures still remains unclear. Besides, the local structure and distribution state of divalent RE ions in glasses, which dominate the optical and magneto-optical properties, are not understood completely. Furthermore, the relationship between the local structure and magneto-optical properties of glasses containing divalent RE ions is not clarified. This thesis is undertaken to resolve such problems. The contents of respective chapters are summarized as follows.

In Chapter 1, the results of Mössbauer effect measurements for Eu^{2+} ions incorporated in sodium borate and alkali silicate glasses are presented. The valence state of europium ions, the average coordination number for Eu^{2+} and the covalency of $Eu^{2+}-O$ bond are evaluated from the value of isomer shift. Besides, the ligand asymmetry at Eu^{2+} ion site is estimated from the magnitude of quadrupole interaction. In particular, the variations of the covalency and ligand asymmetry with glass composition are discussed in terms of the structural role of Eu^{2+}.

In Chapter 2, the results of fluorescence line-narrowing spectroscopy for Sm^{2+} and its isoelectronic Eu^{3+} in sodium borate glasses are described. In order to effectively obtain the site-dependent structural information, measurements are performed using a pulsed tunable dye-laser. The lifetime, as well

as the line-narrowing fluorescence, is investigated as a function of excitation energy, and the site-dependent optical properties for both ions are compared with each other.

In Chapter 3, hole-burning spectroscopy is applied to Eu^{3+}- and Pr^{3+}-doped silicate glasses. First, two types of hole-burning mechanisms of Eu^{3+}, a persistent and a transient one, are classified in sodium silicate and aluminosilicate glasses according to their hole characteristics. Based on the result, persistent spectral hole burning is used to measure the homogeneous linewidth for Eu^{3+} in the sodium aluminosilicate glass. The temperature dependence of homogeneous linewidth is discussed in connected with specific vibrational properties of glasses, such as localization of vibrational excitations and the presence of two-level system. Subsequently, the effect of Na_2O on persistent spectral hole burning of Pr^{3+} is examined in sodium silicate glasses. It is shown that the homogeneous linewidth and hole-burning efficiency vary with the composition of the sodium silicate glass. The origin of the low-frequency vibrational modes which contribute to both the homogeneous linewidth and hole-burning efficiency is suggested.

In Chapter 4, an attempt is made to realize high-temperature persistent spectral hole burning in Eu^{3+} -doped oxide glasses which usually show spectral hole burning only at very low temperatures. The thermal stability of persistent holes is of crucial importance for the implementation of frequency-domain information storage. The hole character of Eu^{3+} -doped silicate glasses is controlled by a melting atmosphere, and room-temperature persistent spectral hole burning is achieved in the glasses prepared under a nitrogen atmosphere. This is the first case where the hole with room-temperature stability is burned in Eu^{3+} -doped materials. Also, a possible hole-burning mechanism is suggested.

In Chapter 5, the results of Faraday effect measurements for sodium borate

and alkali silicate glasses containing a large amount of Eu^{2+} ions are presented. As a controlling factor of the Faraday effect of Eu^{2+}, the electronic structure of Eu^{2+} in the host glass is of particular importance. The relation between Faraday effect and electronic structure of Eu^{2+} is discussed based on the results of ^{151}Eu Mössbauer effect measurements in Chapter 1. Furthermore, an attempt is made to estimate the magneto-optical figure of merit, which is a significant factor from a practical viewpoint. It is shown that the silicate glasses containing a large amount of Eu^{2+} ions possess large magneto-optical figures of merit.

Finally, in Summary, the whole results and discussions in this thesis are summarized.

References

[1] C. J. Koester and E. Snitzer, Appl. Opt. **31**, 1182 (1964).

[2] R. J. Mears, L. Reekie, I. M. Jauncey, and D. N. Payne, Electron. Lett. **23**, 1026 (1987).

[3] P. Selzer, D. L. Huber, D. S. Hamilton, W. M. Yen, and M. J. Weber, Phys. Rev. Lett. **36**, 813 (1976).

[4] J. Hegarty and W. M. Yen, Phys. Rev. Lett. **43**, 1126 (1979).

[5] J. M. Pellegrino, W. M. Yen, and W. M. Weber, J. Appl. Phys. **51**, 6332 (1981).

[6] J. R. Morgan and M. A. El-Sayd, Chem. Phys. Lett. **84**, 213 (1981).

[7] G. Dixon, P. Powell, and X. Gang, Phys. Rev. B **33**, 2713 (1986).

[8] R. T. Brundage and W. M. Yen, Phys. Rev. B **33**, 4436 (1986).

[9] R. M. Shelby, Opt. Lett. **8**, 46 (1983).

[10] R. M. Macfarlane and R. M. Shelby, Opt. Lett. **9**, 533 (1984).

[11] A. Winnacker, R. M. Shelby, and R. M. Macfarlane, Opt. Lett. **10**, 350 (1985).

[12] R. Jaaniso and H. Bill, Europhys. Lett. **16**, 569 (1991).

[13] K. Hirao, S. Todoroki, and N. Soga, J. Lumin. **55**, 217 (1993).

[14] K. Hirao, S. Todoroki, D. H. Cho, and N. Soga, Opt. Lett. **18**, 1586 (1993).

[15] D. H. Cho, K. Hirao, K. Fujita, and N. Soga, J. Am. Ceram. Soc. **79**, 327 (1996).

[16] A. Kurita, T. Kushida, T. Izumitani, and M. Matsukawa, Opt. Lett. **19**, 314 (1994).

[17] M. Nogami, Y. Abe, K. Hirao, and D. H. Cho, Appl. Phys. Lett. **66**, 2952 (1995).

[18] S. Nakamura, Rev. Laser Eng. (Japan) **25**, 498 (1997).

Chapter 1

Local structure of divalent rare-earth ions in glasses

1.1 ^{151}Eu Mössbauer spectroscopy

Mössbauer effect, the recoil-free resonant absorption of γ-ray, is an effective tool for obtaining information on environment around Mössbauer-active elements. Since the discover of the phenomenon by Mössbauer in 1958 [1], the Mössbauer effect has been extensively applied to some aspects of physics, chemistry and biochemistry. The main subjects have been the bond character, valence state, coordination state and magnetism in solids.

Both naturally occurring isotopes of europium, ^{151}Eu (47.82%) and ^{153}Eu (52.18%) can be used for Mössbauer spectroscopy. After ^{57}Fe and ^{119}Sn, ^{151}Eu is one of the most studied Mössbauer isotopes. The reasons are as follows.

- ^{151}Sm which is used as a γ-ray source exhibits a simple spectrum, and has a long half-life of 90 years.

- Source and absorber have quite high recoil-free fraction, and spectra are observed at temperatures up to several hundred degrees centigrade.

- The relatively small linewidth of ^{151}Eu Mössbauer transition allows the easy observation of isomer shift and magnetic hyperfine interaction, although the observation of quadrupole interaction is less easy.

9

On the other hand, divalent rare-earth ions in glasses display a variety of interesting optical and magneto-optical properties. These properties are significantly affected by the local structure around divalent rare-earth ions. Hence, for the realization of glass materials with superior functions, the characterization of these properties should be done from structural viewpoints. ^{151}Eu Mössbauer effect measurements yield effective information about the local structure around rare-earth ions, which can not be obtained with other conventional spectroscopic techniques. In this chapter, the chemical and electronic states of Eu^{2+} ions in several oxide glasses will be discussed on the basis of three Mössbauer parameters, that is, isomer shift, quadrupole interaction, and magnetic hyperfine interaction. These three parameters are treated in the following sections.

1.1.1   Isomer shift

The energy difference between ground and excited states of nucleus is influenced by the environment around the nucleus. When the energy differences between the ground and excited states of absorber and source are E_A and E_S, respectively, isomer shift, δ, is expressed by

$$\delta = E_A - E_S. \tag{1.1}$$

The energy difference between the ground and excited states of nucleus is calculated by taking into account the monopolar interaction between the electron and the Zth nucleus with a finite size, and is expressed as follows:

$$E = \frac{2\pi}{5} Ze^2 |\Psi(0)|^2 \ (< r^2 >_e - < r^2 >_g), \tag{1.2}$$

where $< r^2 >_e$ and $< r^2 >_g$ denote the average radii of nucleus in ground and excited states, respectively, and $|\Psi(0)|$ is the electron density at the nucleus.
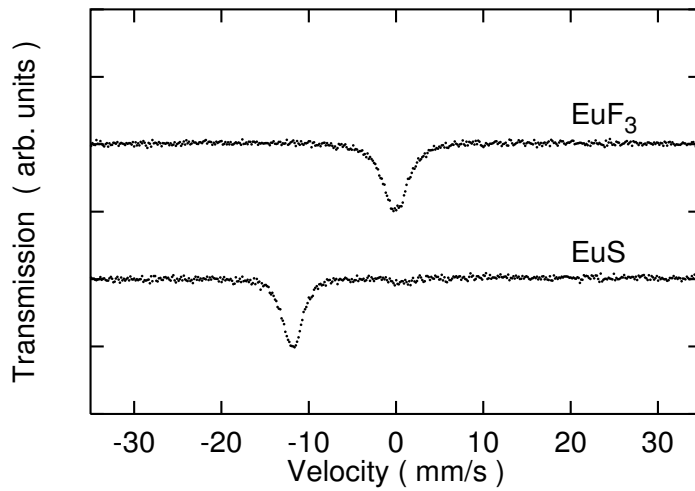
Figure 1.1: ^{151}Eu Mössbauer spectra of EuF$_3$ and EuS.

By using Eqs. (1.1) and (1.2), the isomer shift is given by

$$\delta = \frac{2\pi}{5} Ze^2 \{|\Psi_A(0)|^2 - |\Psi_S(0)|^2\} \times \Delta < r^2 >, \tag{1.3}$$

where $|\Psi_A(0)|^2$ and $|\Psi_S(0)|^2$ represent the electron densities at the nucleus of the absorber and source, respectively, and $\Delta < r^2 >$ is the difference between the average nuclear radii in the excited and ground states. In the case of ^{151}Eu, $\Delta < r^2 >$ is positive, the nuclear radius being larger in the excited state than in the ground state [2]. Therefore, the isomer shift of ^{151}Eu, δ, increases with an increase in the electron density at the nucleus, $|\Psi_A(0)|^2$.

The most common oxidation state of europium ion in ionic solids is the trivalent one with a $4f^6$ configuration. Europium can also exist as the divalent oxidation state with a $4f^7$ configuration. ^{151}Eu Mössbauer spectra of EuF$_3$ and EuS at room temperature are shown in Fig. 1.1. The difference in position of Mössbauer absorption lines of divalent and trivalent europium ions is about 14 mm/s, which is much greater than the natural linewidth (1.31 mm/s) [3]. Samuel and Delgass [4] calculated the relationship between the isomer shift and

the total electron density at the nucleus of ^{151}Eu as a function of the electronic configuration. The electron density at the nucleus of ^{151}Eu increases with an increase in the number of $6s$ electrons, while it decreases with an increase in the number of $4f$ and $5d$ electrons, because of a screening effect. The smaller isomer shift of Eu^{2+} compounds can be attributed to the smaller electron density of s-orbital at the nucleus, which is brought about by the shielding effect of the $4f$ electron on the $6s$ orbital. Thus the detailed information about the valence and electronic states of europium ions can be obtained from the isomer shift.

1.1.2   Quadrupole Interaction

The interaction of nuclear quadrupole moment with electric field gradient resulting both from the electronic states of an ion and from the surrounding ions partially removes the degeneracies of excited and ground states, and results in
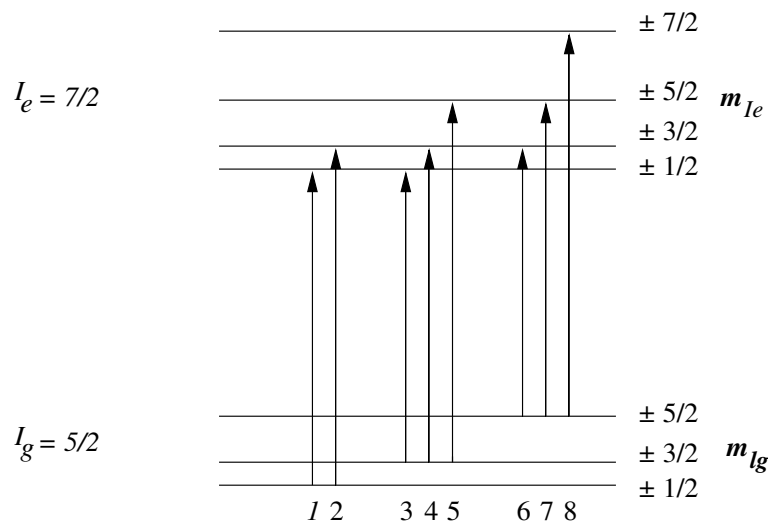

Figure 1.2: Nuclear energy levels of ^{151}Eu in the presence of quadrupole interaction.

a quadrupole splitting of the absorption. This arises from the fact that the nucleus is not a sphere. In the case of ^{151}Eu, since the ground and excited nuclear states have nuclear spins of 5/2 and 7/2, respectively, the ground state is split into three sublevels and the excited state into four sublevels, as shown in Fig. 1.2. For Eu^{3+} with the ground state $^7F_0$, the quadrupole interaction results from an anisotropy of $4f$ electrons as well as a lattice distortion. As for Eu^{2+} with the ground state $^8S_{7/2}$, on the other hand, the quadrupole interaction is only caused by the surrounding ligands because of the spherically symmetrical charge distribution.

The quadrupole Hamiltonian is written as

$$H_Q = \frac{eQV_{zz}}{4I(2I-1)}[3\hat{I}_z^2 - \hat{I}^2 + \frac{1}{2}\eta(\hat{I}_+^2 + \hat{I}_-^2)], \tag{1.4}$$

where e is the elementary electron charge, Q is the nuclear quadrupole moment, V_{zz} is the principal component of the electric field gradient tensor, I is the nuclear spin, $\hat{I}$ and $\hat{I}_z$, are the operators for the nuclear spin and for the z projection of the nuclear spin, $\hat{I}_+$ is $\hat{I}_x + i\hat{I}_y$, $\hat{I}_-$ is $\hat{I}_x - i\hat{I}_y$, and η is the asymmetry parameter of the electric field gradient and is equal to $(V_{xx} - V_{yy})/V_{zz}$ with the usual assumption that $|V_{xx}| < |V_{yy}| < |V_{zz}|$.

Hamiltonians such as Eq. (1.4) must be written for the ground and excited states, respectively. Assuming η is zero or close to zero, the nuclear state energies are given by

$$E_{m_I} = eQV_{zz}\left(1 + \frac{\eta^2}{3}\right)^{1/2}\frac{3m_I^2 - I(I+1)}{4I(2I-1)}, \tag{1.5}$$

where for the ground state, $Q = Q_g$, $I = I_g = 5/2$, $m_{I_g} = 5/2, 3/2, 1/2$, and for the excited state, $Q = Q_e = 1.34Q_g$ [5], $I = I_e = 7/2$, $m_{I_e} = 7/2, 5/2, 3/2, 1/2$. Hence the transition energies, E, are given by

Table 1.1: Normalized Mössbauer spectral transition intensities for ^{151}Eu perturbated by quadrupole interaction with $\eta = 0$.

m_{I_e}	m_{I_g}		
	5/2	3/2	1/2
7/2	0.25	0	0
5/2	0.0714	0.1786	0
3/2	0.0120	0.1190	0.1190
1/2	0	0.0357	0.2143

$$
\begin{aligned}
E &= eQ_g V_{zz} \left(1 + \frac{\eta^2}{3}\right)^{1/2} \times \\
&\left(\frac{1.34[3m_{I_e}^2 - I_e(I_e + 1)]}{4I_e(2I_e - 1)} - \frac{[3m_{I_g}^2 - I_g(I_g + 1)]}{4I_g(2I_g - 1)}\right).
\end{aligned} \tag{1.6}
$$

These energies are calculated for the different values of m_{I_g} and m_{I_e}. Then there are only eight allowed transitions, with $\Delta m_I = 0, \pm 1$ (see Fig. 1.2), the intensities of which are given by the square of the Clebsch-Gordan coefficients. Table 1.1 shows the intensities of $5/2 \rightarrow 7/2$ transitions which are the case of ^{151}Eu. In this table, the total intensity is normalized to one. If η is substantially different from zero, it is necessary to compute the eigenvalues of both the ground state and the excited state Hamiltonians, $E_{m_{I_g}}$ and $E_{m_{I_e}}$, so as to obtain the transition energies, and then to calculate the differences

$$
E = E_{m_{I_e}} - E_{m_{I_g}} \tag{1.7}
$$

for all the values of m_{I_e} and m_{I_g}, i.e., for 12 transitions. In Section 1.2, the magnitude of quadrupole interaction is evaluated using a method for calculat-

ing the energies and intensities of the 12 transitions developed by Shenoy and Dunlap [6].

1.1.3   Magnetic hyperfine interaction

Before considering the influence of magnetic interaction on ^{151}Eu Mössbauer spectra, some comments on the magnetic properties of europium ions will be useful. Eu^{2+} has a half-filled $4f^7$ electron configuration, which leads to a $^8S_{7/2}$ ground state with a zero resultant orbital angular momentum, but with a nonzero spin angular momentum; the effective magnetic moment of the divalent europium is 7.94 μ_B, where μ_B is the Bohr magneton. On the other hand, Eu^{3+} has a $4f^6$ electron configuration, which leads to a $^7F_0$ ground state with a zero resultant total angular momentum. Thus the effective magnetic moment of trivalent europium is virtually zero.
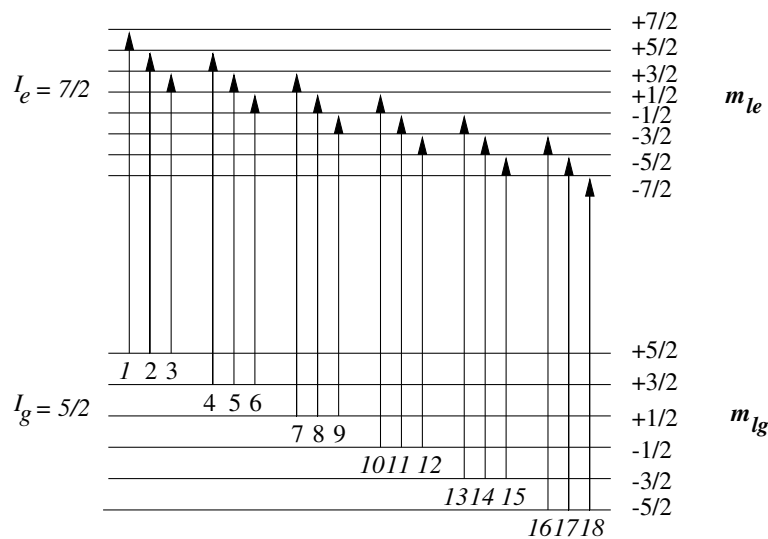
Figure 1.3: Nuclear energy levels of ^{151}Eu in the presence of magnetic hyperfine interaction.

In the presence of either an internal or external magnetic field, the degeneracies of the excited and ground states are completely removed, and hyperfine split spectrum is obtained (see Fig. 1.3). Although 18 transitions with $\Delta m_I = 0, \pm 1$ are allowed, the number of experimentally resolved lines is less because of the accidental superpositions of some of the transitions as well as the relatively broad linewidth of the transitions. The hyperfine splitting is usually observed with Mössbauer effect in ferro- or antiferromagnetic materials and in diamagnetic or paramagnetic materials with an external field. However, it

Figure 1.4: Mössbauer spectra of europium ions in (a) SiO$_2$ and (b) Al$_2$O$_3$ -doped SiO$_2$ glasses.

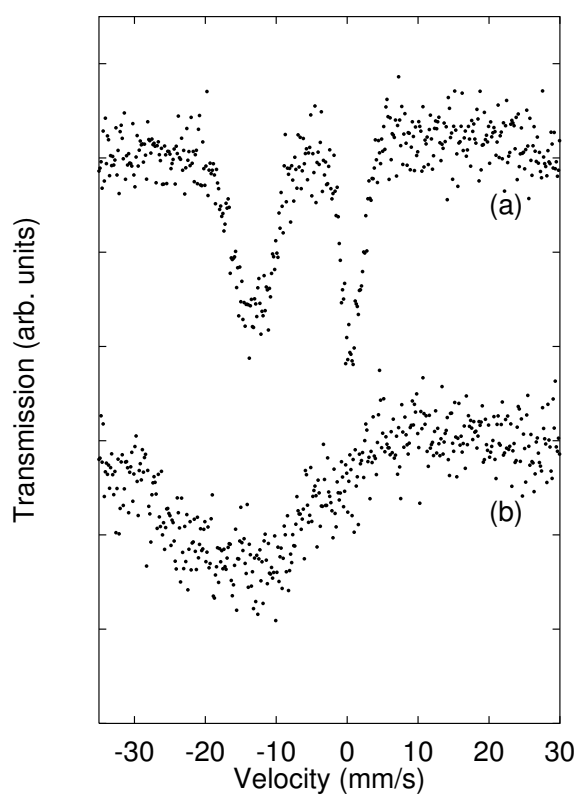should also be possible for the hyperfine splitting to be observed for paramagnetic materials without the application of an external field if the electron spin relaxation time, τ, is large compared to the reciprocal of the hyperfine interaction energy, A, that is,

$$\tau > \hbar/2A. \tag{1.8}$$

Figure 1.4 shows Mössbauer spectra of europium ions in pure SiO_2 and Al_2O_3 (3.05 wt%) -doped SiO_2 glasses at room temperature. These glasses were prepared by vapor-phase axial deposition (VAD) method in He (90)/H_2 (10) (vol%) atmosphere. The concentration of europium ions is 7000 ppm. For the SiO_2 glass, the spectrum is composed of two absorption bands at about –12 mm/s and 0 mm/s. These absorption bands are ascribed to Eu^{2+} and Eu^{3+} ions, respectively. As for the Al_2O_3 -doped SiO_2 glass, on the other hand, only one absorption band due to Eu^{2+} at around –13 mm/s appears as a broad spectrum. The broad absorption results from the paramagnetic hyperfine interaction as mentioned above. This is because Eu^{2+} ions are rather homogeneously distributed in the glass and the spin-spin relaxation time is long when the concentration of Eu^{2+} is low (7000 ppm). The magnetic hyperfine interaction due to the presence of ordered magnetic phases is probably ruled out because the magnetic transition temperature of oxide crystals containing Eu^{2+} ions is usually much lower than room temperature. On the contrary, the peak due to Eu^{2+} in pure SiO_2 glass is much sharper than that in Al_2O_3 -doped SiO_2 glass, as shown in Fig. 1.4. The result indicates that clustering or paring of Eu^{2+} ions takes place in the pure SiO_2 glass. The clustering or paring makes the spacing between Eu^{2+} ions short. As a result, the paramagnetic hyperfine splitting disappears in the SiO_2 glass because the spin-spin relaxation time becomes short; that is, the condition of Eq. (1.8) is no longer satisfied. Thus, the Mössbauer spectra of Eu^{2+} particularly give unique information about the magnetic properties in solids.

1.2   Mössbauer spectroscopy of Eu^{2+} ions in oxide glasses

1.2.1   Introduction

Glass materials containing divalent rare-earth ions have attracted considerable attention as optical and magneto-optical devices. Persistent spectral hole burning has been observed in Sm^{2+} -doped borate glasses at room temperature [7]. A large inhomogeneous linewidth in these glasses is advantageous for applications of the materials to frequency and time domain optical memories. As for Eu^{2+}, Shafer and Suits [8] prepared aluminoborate glasses containing a large amount of Eu^{2+} ions, and revealed that these glasses show a Faraday effect with a large Verdet constant in the visible light region. The paramagnetic Faraday effect can be used as magneto-optical devices such as an optical isolator, an optical switch and an optical shutter in the visible light region. Also, Eu^{2+} ions doped in glasses exhibit fluorescence in blue to green region due to the parity-allowed electric dipole transition from the outer $5d$ level to the $4f$ ground state, which is influenced to a much greater extent by the environment of the ions than the dipole-forbidden transition between intra-$4f$ levels [9].

^{151}Eu Mössbauer spectroscopy has been established as a useful and sensitive tool to investigate the local structure around europium ions in solids. In general, ^{151}Eu Mössbauer effect measurements on amorphous materials containing europium ions revealed absorption lines broader than that expected for Eu^{3+} and Eu^{2+} ions in a site with a cubic symmetry [10–15]. This results from the unresolved quadrupole splitting as well as the structural disorder of glass. Therefore, some attempts have made to analyze the line broadening, taking account of an electric quadrupole interaction between the electric field gradient and the electric quadrupole moment of the ^{151}Eu Mössbauer nucleus. For

the Mössbauer spectrum of Eu^{2+} in amorphous EuFe$_2$Si$_2$ measured by Hodge *et al.* [12], the absorption peak, a full width at half maximum (FWHM) of which was around 7 mm/s, was fitted using a convolution of Lorentzian multiplets, corresponding to a distribution of the quadrupole interaction parameter or to a distribution of the asymmetry parameter. Coey *et al.* [15] carried out Mössbauer effect measurements on Eu^{2+}-containing fluorozirconate glass and pointed out that the line broadening is due to not only the quadrupole interaction but also a variety of Eu^{2+} sites, i.e., isomer shifts.

In glasses, the ^{151}Eu Mössbauer resonance has been extensively applied to Eu^{3+}. In contrast, only a few Mössbauer studies have been reported on Eu^{2+}-containing glasses [13, 15]. Especially, no systematic studies have been made concerning the relationship between the glass composition and Mössbauer parameters, i.e., isomer shift and quadrupole interaction. One of the main reasons may be the fact that a glass must be prepared under a strong reducing condition.

The aim of this study is to prepare borate and silicate glasses containing various concentrations of Eu^{2+} ions and to obtain information about the chemical structures of the Eu^{2+} ions in these glasses. Moreover, the isomer shift and quadrupole interaction parameter are determined from the analysis of a full Hamiltonian method, and the results are discussed in connection with the structural changes and the optical basicity of glass.

1.2.2 Experimental procedure

1.2.2.1 Preparation of glass

Glass samples were prepared from reagent-grade Eu$_2$O$_3$, Li$_2$CO$_3$, Na$_2$CO$_3$, K$_2$CO$_3$, B$_2$O$_3$, Al$_2$O$_3$ and SiO$_2$ as starting materials. The compositions are summarized in Table 1.2. The notations for glasses containing more than

Table 1.2: Glass compositions and their notations.

(a) Borate glasses

Notation	Composition (mol%)
	xEuO$\cdot$(100 − x)(0.10Na$_2$O$\cdot$0.90B$_2$O$_3$)
	(x = 0.99, 5.0)
	xEuO$\cdot$(100 − x)(0.30Na$_2$O$\cdot$0.70B$_2$O$_3$)
	(x = 0.99, 2.96, 4.92)
90BN10E	10EuO$\cdot$90 (0.10Na$_2$O$\cdot$0.90B$_2$O$_3$)
70BN10E	10EuO$\cdot$90 (0.30Na$_2$O$\cdot$0.70B$_2$O$_3$)
90BN15E	15EuO$\cdot$85 (0.10Na$_2$O$\cdot$0.90B$_2$O$_3$)
85BN15E	15EuO$\cdot$85 (0.15Na$_2$O$\cdot$0.85B$_2$O$_3$)
80BN15E	15EuO$\cdot$85 (0.20Na$_2$O$\cdot$0.80B$_2$O$_3$)
75BN15E	15EuO$\cdot$85 (0.25Na$_2$O$\cdot$0.75B$_2$O$_3$)
70BN15E	15EuO$\cdot$85 (0.30Na$_2$O$\cdot$0.70B$_2$O$_3$)
65BN15E	15EuO$\cdot$85 (0.35Na$_2$O$\cdot$0.65B$_2$O$_3$)
90BN20E	20EuO$\cdot$80 (0.10Na$_2$O$\cdot$0.90B$_2$O$_3$)
70BN20E	20EuO$\cdot$80 (0.30Na$_2$O$\cdot$0.70B$_2$O$_3$)
75B25E	25EuO$\cdot$75B$_2$O$_3$
70B30E	30EuO$\cdot$70B$_2$O$_3$

Table 1.2: (*Continued.*)

(b) Silicate glasses

Notation	Composition (mol%)
78SN10E	10EuO·90 (0.22Na$_2$O·0.78SiO$_2$)
78SN16E	16.2EuO·83.8 (0.22Na$_2$O·0.78B$_2$O$_3$)
78SN20E	20EuO·80 (0.22Na$_2$O·0.78SiO$_2$)
78SN30E	30EuO·70 (0.22Na$_2$O·0.78SiO$_2$)
78SL20E	20EuO·80 (0.22Li$_2$O·0.78SiO$_2$)
78SK20E	20EuO·80 (0.22K$_2$O·0.78SiO$_2$)
67SAN20E	20EuO·80 (0.22Na$_2$O·0.11Al$_2$O$_3$·0.67SiO$_2$)
56SAN20E	20EuO·80 (0.22Na$_2$O·0.22Al$_2$O$_3$·0.56SiO$_2$)

10 mol% EuO were also shown in Table 1.2.

(a)Borate glasses

For 75B25E and 70B30E glasses, the raw materials were mixed thoroughly and the mixture was melted in a graphite crucible with high purity in an electric furnace consisting of a graphite heater, an insulator and a water jacket in Ar(95)/H$_2$(5) (vol%) gas at 1400 °C for 30 min. For ternary systems of xEuO· (100 − x)(0.3Na$_2$O·0.7B$_2$O$_3$)(x = 0.99, 2.91, 4.76) and xEuO· (100 − x)(0.1Na$_2$O·0.9B$_2$O$_3$) (x = 0.99), the mixture was melted in a platinum crucible in air at 1150 °C for 30 min so as to eliminate carbon dioxide from the melt. The melt was poured onto a stainless steel plate, and the resultant Eu^{3+} -containing glass was further melted in a carbon crucible under Ar(95)/H$_2$(5) (vol%) atmosphere at 1350∼1400 °C for 30 min. For ternary systems with the other compositions, it was difficult to prepare a homogeneous Eu^{3+}-containing glass at 1150∼1300 °C because of a phase separation as well

as a high melting temperature. Therefore, the glass was prepared as follows. Binary alkali borate glass was produced by melting a mixture of B_2O_3 and Na_2CO_3 in a platinum crucible at 1150 °C for 30 min in air. The melt was poured onto a stainless steel plate and a glass thus obtained was ground into a powder. Then Eu_2O_3 was added to the powder, and subsequently the mixture was melted in a carbon crucible under $Ar(95)/H_2(5)$ (vol%) atmosphere at 1350~1400 °C for 30 min. The resultant specimens were ascertained to be amorphous using X-ray diffraction analyses with CuKα radiation.

(b)Silicate glasses

Except 78SN30E and 56SAN20E glasses, the glasses were prepared as follows. The raw materials were mixed thoroughly and melted in a platinum crucible in air at 1300 °C for 1~2 h so as to eliminate carbon dioxide, and then remelted at 1600 °C for 2 h. The melt was poured onto a stainless steel plate. The resultant specimen was remelted using a carbon crucible under a $N_2(50)/Ar(47.5)/H_2(2.5)$ (vol%) atmosphere at 1550~1600 °C for 1 h. For 78SN30E composition, first Na_2CO_3 and SiO_2 were mixed, melted in air at 1300 °C to eliminate carbon dioxide, and remelted at 1600 °C for 2 h. Then the glass obtained by pouring the melt onto the stainless steel plate was pulverized and Eu_2O_3 was added. The mixture thus obtained was melted in a carbon crucible at 1550 °C in the reducing atmosphere for 1 h. For 56SAN20E composition, the mixture of raw materials was calcined at 1300 °C for 2 h in air. The calcination was repeated twice. The resultant specimen was melted in a carbon crucible in the reducing atmosphere at 1550 °C for 1 h.

1.2.2.2 Mössbauer measurement

The Mössbauer absorption spectra were obtained in a standard transmission geometry at room temperature, using a 21.5 keV γ-ray source of $^{151}Sm_2O_3$ with activity of 1.85 GBq. The velocity calibration was done with the magnetic hy-

perfine spectrum of α-Fe obtained using a 14.4 keV γ-ray of ^{57}Co doped in Rh . The spectrum of EuF$_3$ was measured as a standard of Doppler velocity. The surface density of the Mössbauer absorber was about $10\sim20$ mg/cm^2. Mössbauer spectrum of EuS was also measured, and the isomer shift was compared with the value reported by Berkooz [16]. The isomer shift of EuS in the present measurement was –11.78 mm/s, which is in agreement with Berkooz's result, i.e., –11.75 mm/s. Here, the isomer shift derived by Berkooz is relative to Eu$_2$O$_3$, and it was converted to a value referred to EuF$_3$ by adding 1.037 mm/s [2] to the original value. In addition, the FWHM of the present EuS was measured as about 2.5 mm/s.

1.2.3   Results

Mössbauer spectra of xEuO$\cdot$($100-x$)(0.1Na$_2$O$\cdot0.9$B$_2$O$_3$) ($x = 0.99$, 5.0, 10.0, 15.0, 20.0) and xEuO$\cdot$($100-x$)(0.3Na$_2$O$\cdot0.7$B$_2$O$_3$) ($x = 0.99$, 2.91, 4.76, 10.0, 15.0, 20.0) glasses are shown in Figs. 1.5 and 1.6, respectively. All of the spectra in Fig. 1.5 show only one absorption peak with isomer shift around –13.0 mm/s, corresponding to an oxidation state of +2. No absorption peak due to Eu^{3+} is found around $0.0\sim1.0$ mm/s. On the other hand, Fig. 1.6 exhibits a resonance peak of Eu^{3+} as well as Eu^{2+}. Figures 1.5 and 1.6 indicate that the splitting of the peak due to hyperfine fields is clearly observed in the spectra of glasses with low concentrations of Eu^{2+} ions. Winterer *et al.* performed Mössbauer effect measurements of Eu^{2+} ions in borate glasses from 4.2 to 300 K, and revealed that the hyperfine structure is almost independent of the temperature because $4f$ electrons are shielded rather strongly by the outer orbitals. This indicates that the fluctuation of hyperfine fields is dominated by spin-spin relaxation and not by spin-lattice relaxation. Moreover, they found that the hyperfine structure becomes ambiguous by doping these glasses with paramagnetic Mn^{2+} ions. This means that cross relaxation be-
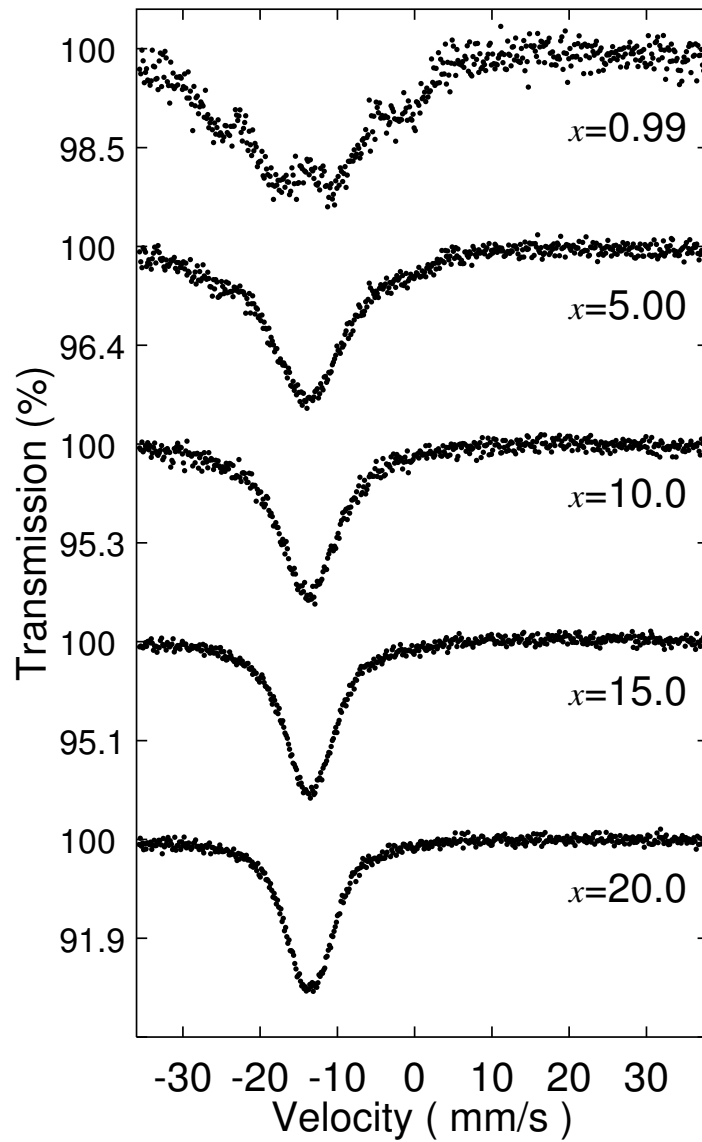
Figure 1.5: Mössbauer spectra of xEuO$\cdot$($100 - x$)(0.1Na$_2$O$\cdot$0.9B$_2$O$_3$) ($x = 0.99, 5.0, 10.0, 15.0, 20.0$) glasses.
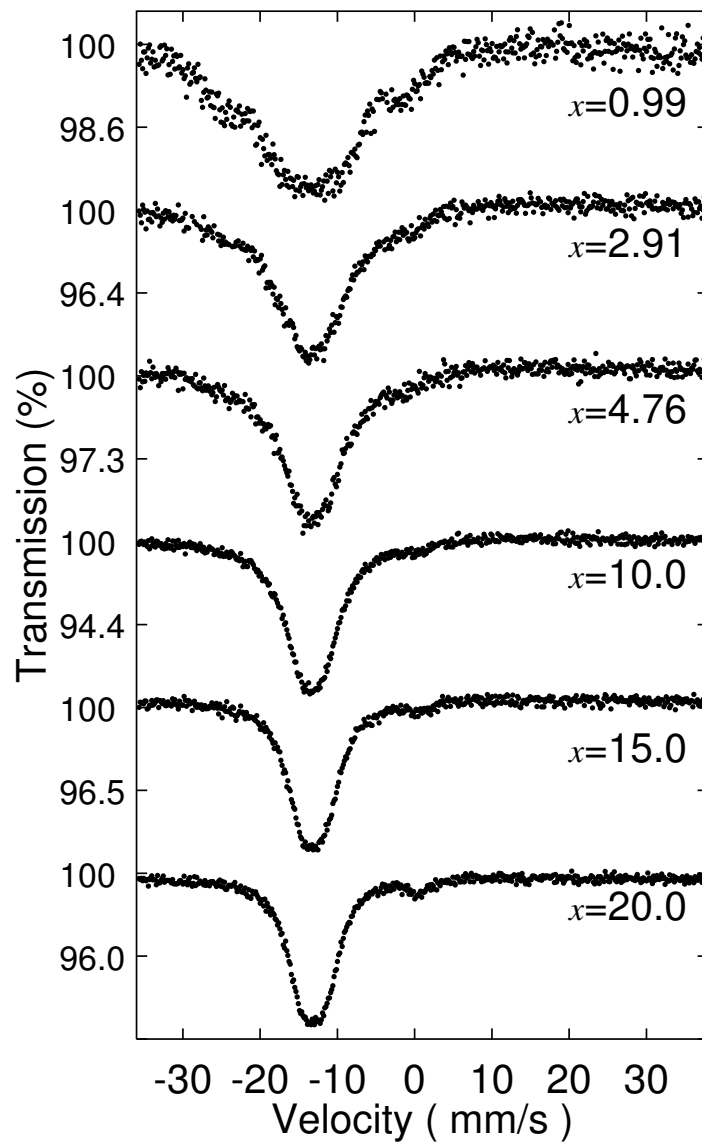
Figure 1.6: Mössbauer spectra of xEuO·$(100 - x)(0.3\text{Na}_2\text{O}\cdot0.7\text{B}_2\text{O}_3)(x = 0.99, 2.91, 4.76, 10.0, 15.0, 20.0)$ glasses.

tween Eu^{2+} and Mn^{2+} ions increases the spin-spin relaxation rate. Thus, in dilute Eu^{2+} -containing glasses, the hyperfine structure is brought about by paramagnetic hyperfine interactions; the spin-spin relaxation time is enough long compared to the reciprocal of the hyperfine interaction energy. The dispersion state of impurity ions doped in glasses depends on the glass composition. For instance, Tanaka *et al.* [17] obtained information on the iron ion clusters in lithium borate glasses utilizing electron spin resonance (ESR) measurements, and revealed that the state of the clusters changes with glass composition. Within the framework of this study, the hyperfine structure indicates that Eu^{2+} ions are distributed rather homogeneously in the glasses with low and high sodium contents when the concentration of Eu^{2+} is low, and therefore the dipolar interactions among the Eu^{2+} ions are very small. A similar concept was also deduced from the site-dependent study using a fluorescence line narrowing technique for Sm^{2+} -doped borate glasses with low sodium contents [18]. On the other hand, as the concentration of Eu^{2+} is increased, the average distance between Eu^{2+} ions becomes short, and the hyperfine structure disappears, owing to the short spin-spin relaxation time. As shown in Figs. 1.5 and 1.6, when the concentrations of Eu^{2+} ions are more than 15 mol%, the FWHM of absorption line is almost unchanged. Hence, the effect of the paramagnetic hyperfine interaction can be ignored in the glasses having these compositions. Here, it is reasonably assumed that the magnetic interaction among Eu^{2+} ions in these glasses is very small, because the magnetic transition temperature is much lower than the room temperature as was revealed by Shoenes *et al.* [19] for oxide glasses containing a large amount of Eu^{2+} ions.

Mössbauer spectra of xEuO·(100 − x)(0.22Na$_2$O·0.78SiO$_2$) (x = 10, 20, 30) glasses are shown in Fig. 1.7. All the spectra exhibit two absorption peaks at about –13 mm/s and 0 mm/s. These absorption bands are assigned to Eu^{2+} and Eu^{3+} ions, respectively. The absorption peak due to Eu^{2+} manifets
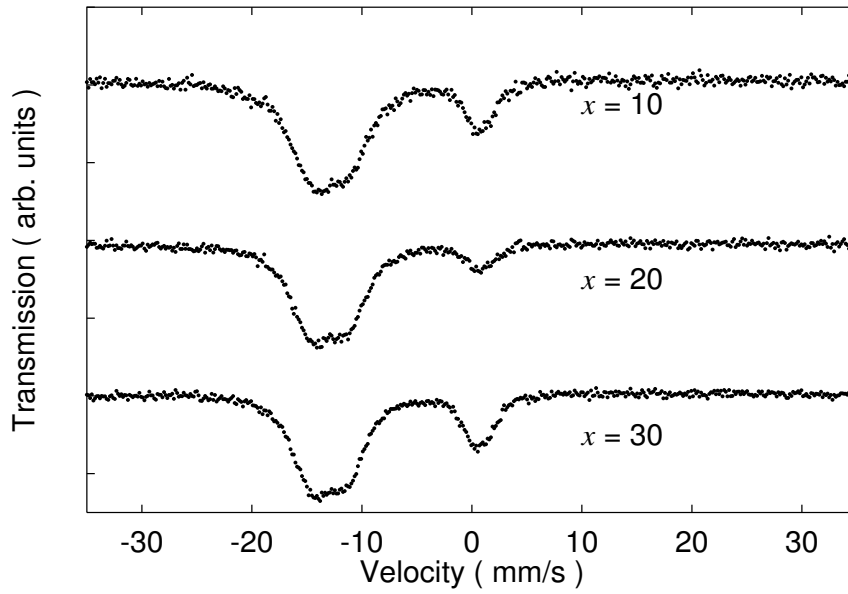
Figure 1.7: Mössbauer spectra of xEuO$\cdot$ ($100 - x$) (0.22Na$_2$O$\cdot 0.78$SiO$_2$)($x = 10, 20, 30$) glasses.

an asymmetric spectral shape. As mentioned above, the magnetic hyperfine interaction among Eu^{2+} ions can be neglected because the glasses contain a large amount of Eu^{2+} ions and the magnetic interaction among Eu^{2+} ions is very small. Thus, the asymmetric absorption band results from the partially resolved quadrupole splitting of of Eu^{2+}, which reflects a large electric field gradient caused by ligands as will be discussed in Section 1.2.4.2.

Figure 1.8(a) shows the experimental data for 30EuO$\cdot$70B$_2$O$_3$ glass and the curve calculated tentatively with a single Lorentzian. The difference between the experimental and theoretical curves is also shown in Fig. 1.8(a). The presence of structure in the difference spectrum indicates the deviation of the peak shape from a single Lorentzian. Furthermore, the FWHM, 6.41 mm/s, found in glasses is significantly broader than the FWHM, 2.5 mm/s, obtained
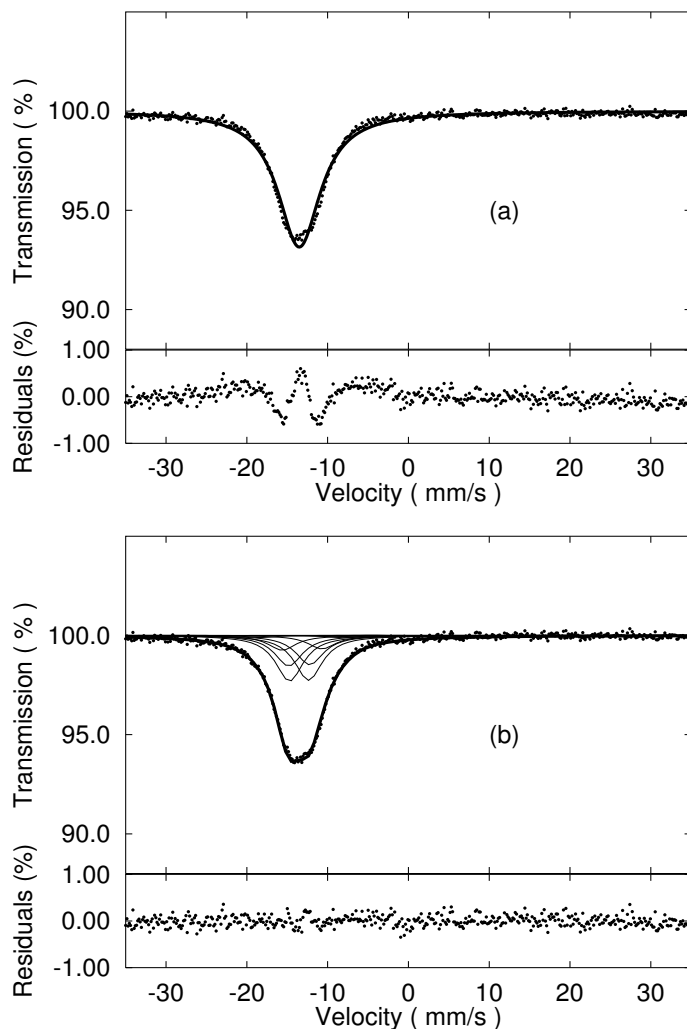
Figure 1.8: (a) Mössbauer spectrum of $30EuO{\cdot}70B_2O_3$ glass. The experimental data (dots) and the theoretical curve drawn using a single Lorentzian (solid line) are shown. The lower spectra represents difference between the experimental and theoretical spectra. (b) Mössbauer spectrum of $30EuO{\cdot}70$ B_2O_3 glass. The experimental data (dots) and the theoretical curve drawn by assuming a nonzero quadrupole interaction (solid line) are shown. The lower spectrum represents difference between the experimental and theoretical spectra.

Γ= 7.09 mm/s

eQ_gV_{zz}= - -

δ= -13.43 mm/s

for EuS with a cubic symmetry for an Eu^{2+} ion. This result also implies that an electric field gradient exists at the Eu^{2+} ion sites in the glass. Moreover, a fit with a single Lorentzian shape for Mössbauer spectrum including unresolved quadrupole interaction gives rise to an error in the value of isomer shift [20]. Thus the absorption band due to Eu^{2+} was fitted using a method for the analysis of pure quadrupole spectra proposed by Shenoy and Dunlap [6].

According to their method, the gamma-ray resonance energy between (I^*, I_z^*) and (I, I_z) is given by

$$R(I_z^*, I_z) = eV_{zz}[Q_e P(I^*, I_z^*) - Q_g P(I, I_z)] + \delta, \tag{1.9}$$

where e is the elementary electronic charge, Q is the quadrupole moment of the nucleus, V_{zz} is the electric field gradient in the direction z, Q_e and Q_g are the nuclear quadrupole moments at excited and ground states, respectively, I^* and I are the nuclear spins at excited and ground states, respectively, and I_z^* and I_z are the z projections of the nuclear spins at excited and ground states, respectively, and δ is the isomer shift. $P(I^*, I_z^*)$ and $P(I, I_z)$ are written as

$$P(I, I_z) = \sum_{N=0}^{4} a_N(I, I_z)\eta^N, \tag{1.10}$$

where η is the asymmetry parameter of electric field gradient and $a_N(I, I_z)$ is the eigenvalue coefficient calculated by Shenoy and Dunlap [6]. The intensity of the transition is also expressed using a polynomial of η as follow:

$$A(I^*, I_z^*; I, I_z) = \sum_{N=0}^{4} b_N(I^*, I_z^*, I, I_z)\eta^N, \tag{1.11}$$

where $b_N(I^*, I_z^*, I, I_z)$ is the intensity coefficient reported in Ref. [6]. In the case of ^{151}Eu, $I^* = 7/2$, $I = 5/2$ and $Q_e/Q_g = 1.34$ [5]. Therefore, there are allowed 12 transitions. The transition energies depend on δ, $eQ_g V_{zz}$ and η, whereas their intensities are a function of η. By using Eq. (1.9) to (1.11), δ, $eQ_g V_{zz}$ and η can be determined by the least squares method under an assumption

that each transitions are expressed as a Lorentzian shape, FWHM, γ of which reflects the site-to-site variation of Eu^{2+}.

Figure 1.8(b) shows the experimental data and the curve calculated by considering a full quadrupole interaction with a asymmetric parameter, as mentioned above. The residual in Fig. 1.8(b) demonstrates that the agreement between experimental and theoretical spectra is fairly good. The physical parameters thus obtained, i.e., δ, eQ_gV_{zz}, γ and η are –13.49 mm/s, –14.74 mm/s, 4.16 mm/s and 0.86, respectively. The γ value, 4.16 mm/s, which is larger than the FWHM, 2.5 mm/s, for an Eu^{2+} ion in a cubic site, is due to the site-to-site
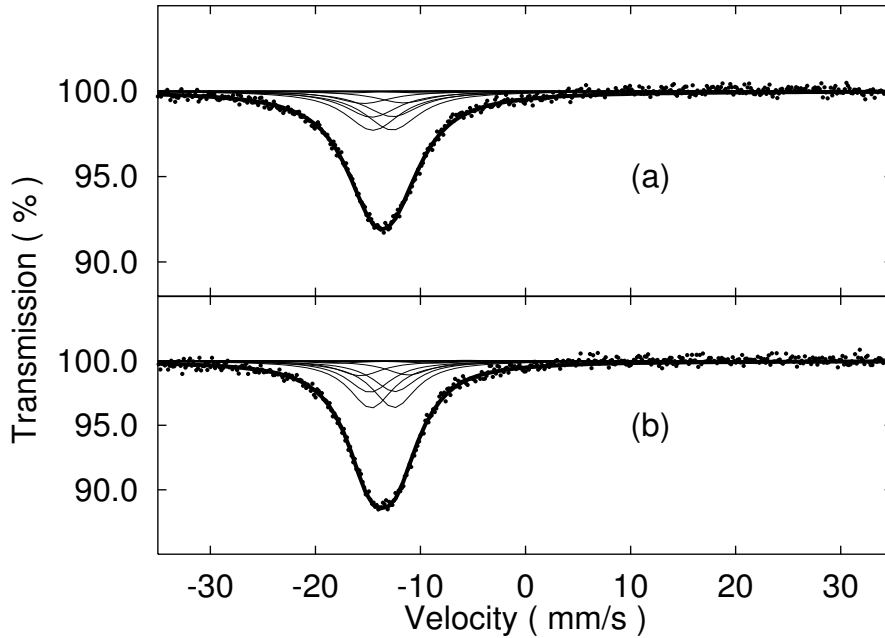

Figure 1.9: Mössbauer spectra of (a) 15EuO·85(0.10Na$_2$O·0.90B$_2$O$_3$) and (b) 20EuO·80(0.10Na$_2$O·0.90B$_2$O$_3$) glasses. The experimental data (dots) and the theoretical curve drawn by assuming a nonzero quadrupole interaction (solid line) are shown.

variation or the disorder structure in the glass. Thus the contribution of the quadrupole interaction, eQ_gV_{zz}, and the contribution of disorder structure, γ, can be separated from each other in the line broadening of the absorption peak. The experimental and theoretical spectra for some of borate and silicate glasses are shown in Figs. 1.9 and 1.10. The theoretical spectra reproduce the experimental data well. The Mössbauer parameters obtained from the analysis of glasses containing more than 15 mol% EuO are listed in Table 1.3, along with the fraction of the absorption peak area of Eu^{2+} to the total absorption area of spectrum. Here, the absorption line of Eu^{3+} around 0 mm/s was analyzed by a single Lorentzian curve because of the poor spectral resolution.
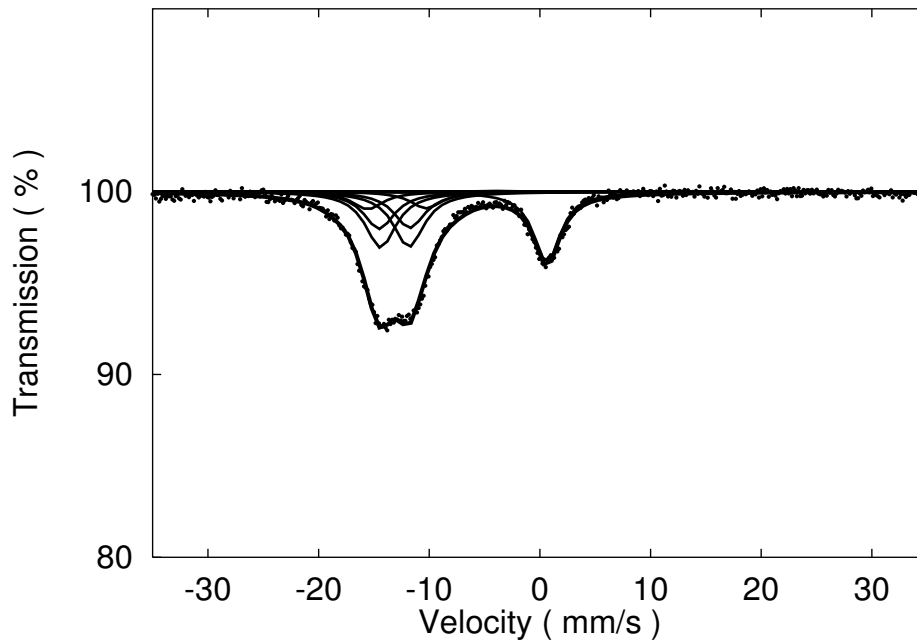

Figure 1.10: Mössbauer spectrum of 30EuO·70(0.22Na$_2$O·0.78SiO$_2$) glass. The experimental data (dots) and the theoretical curve drawn by assuming a nonzero quadrupole interaction (solid line) are shown.

Table 1.3: Mössbauer parameters obtained from the fitting of theoretical curve to the experimental spectrum. δ is the isomer shift with respect to EuF$_3$, Γ is the FWHM of the absorption line, γ is the FWHM of one component of Lorentzian multiplets, eQ_gV_{zz} is the quadrupole interaction parameter, η is the asymmetry parameter. A is the fraction of absorption peak area of Eu^{2+} with respect to the total absorption peak area.

(a) Borate glasses

Sample	δ (mm/s)	Γ (mm/s)	γ (mm/s)	eQ_gV_{zz} (mm/s)	η	A (%)
90BN15E	-13.55	7.59	5.80	-11.20	0.91	100
85BN15E	-13.47	7.31	5.56	-12.39	0.93	100
80BN15E	-13.43	7.28	5.01	-14.05	0.90	100
75BN15E	-13.31	6.95	4.87	-13.80	0.92	100
70BN15E	-13.15	6.72	4.46	-14.37	0.86	99.1
65BN15E	-13.05	6.27	3.98	-14.02	0.86	99.0
90BN20E	-13.53	7.32	5.01	-13.52	0.92	100
70BN20E	-13.15	6.78	4.10	-14.33	0.91	99.0
75B25E	-13.53	6.51	4.54	-13.80	0.88	100
70B30E	-13.48	6.41	4.16	-14.74	0.86	100

Table 1.3: (*Continued.*)

(b) Silicate glasses

Sample	δ (mm/s)	γ (mm/s)	eQ_gV_{zz} (mm/s)	$A(\%)$
78SN16E	-13.07	4.00	-16.65	82.8
78SN20E	-13.11	3.56	-16.67	85.6
78SN30E	-13.10	3.38	-15.64	79.7
78SL20E	-13.18	4.24	-16.76	81.6
78SK20E	-13.07	3.64	-17.98	71.6
67SAN20E	-13.24	3.60	-14.69	85.7
56SAN20E	-13.33	4.12	-15.08	88.6

Figure 1.11 shows the dependence of isomer shift on x and Na$_2$O+EuO content in 15EuO·85$\{x$Na$_2$O·$(1-x)$B$_2$O$_3\}$ glasses. The isomer shift increases as the concentration of Na$_2$O increases. Figure 1.12 shows the magnitude of quadrupole interaction, $|eQ_gV_{zz}|$, as a function of x and Na$_2$O+EuO content in 15EuO·85$\{x$Na$_2$O·$(1-x)$B$_2$O$_3\}$ glasses. The magnitude of quadrupole interaction, $|eQ_gV_{zz}|$ increases with an increase in Na$_2$O content until $x = 0.2$, beyond which it becomes constant.
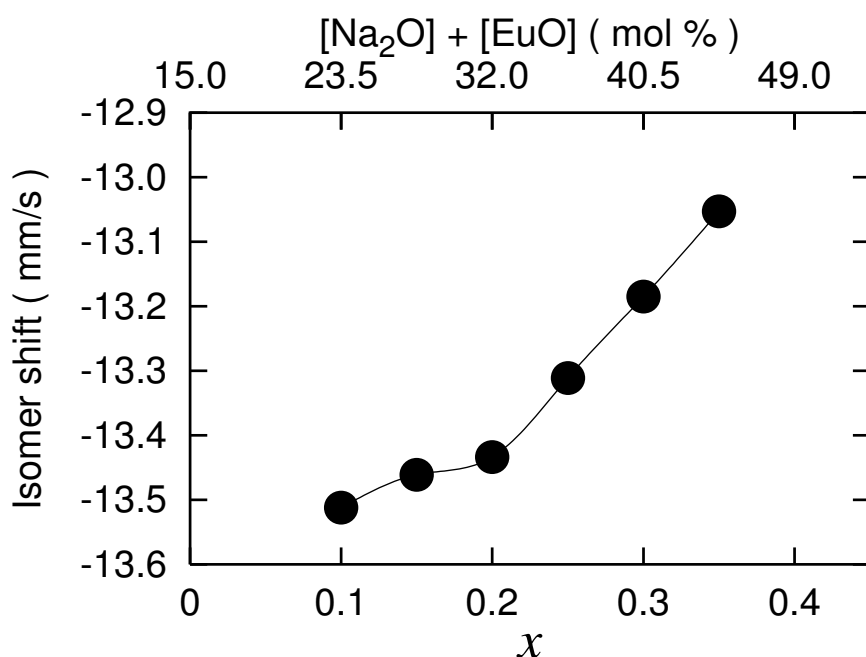

Figure 1.11: Compositional dependence of the isomer shift for ^{151}Eu^{2+} in 15EuO·85$\{x$Na$_2$O·$(1-x)$B$_2$O$_3\}$ glasses.
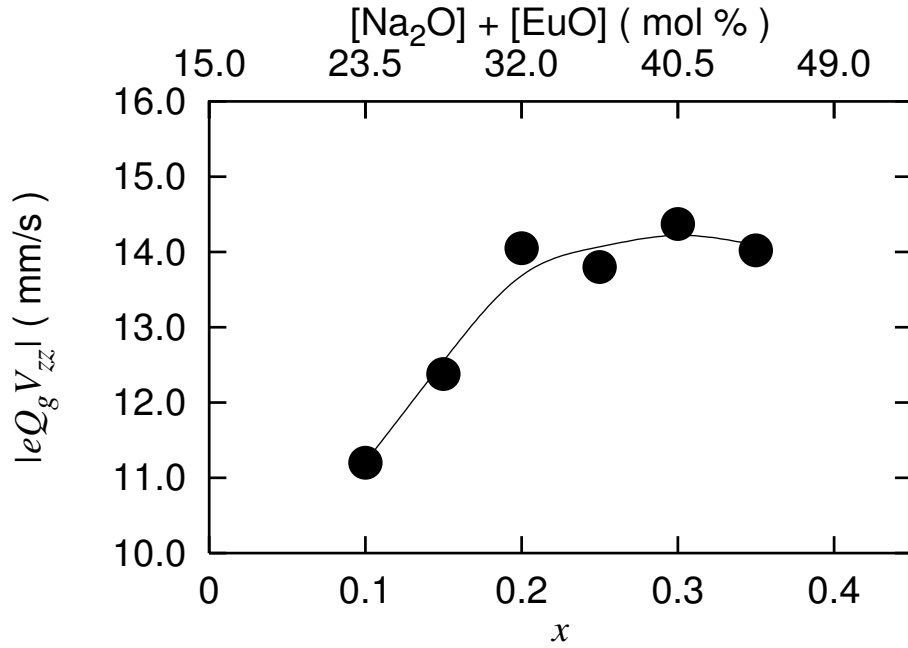
Figure 1.12: Compositional dependence of the magnitude of quadrupole interaction, $|eQ_gV_{zz}|$, for ^{151}Eu^{2+} in 15EuO·85$\{x$Na$_2$O·$(1-x)$B$_2$O$_3\}$ glasses.

1.2.4 Discussion

1.2.4.1 Borate glasses

As shown in Figs. 1.5 and 1.8, all of europium ions are present in the divalent oxidation state in the borate glasses with low Na$_2$O contents and without Na$_2$O. On the other hand, Fig. 1.6 indicates that a part of europium ions exist as the trivalent oxidation state in the borate glasses with high Na$_2$O contents. From the absorption area ratio of Eu^{2+} to Eu^{3+} components in Mössbauer spectra, the fraction of Eu^{2+} component is estimated to be 99 %. In the previous study on the Mössbauer effect of fluorozirconate glass containing both Eu^{2+} and Eu^{3+} ions, the effective Debye temperatures for the Eu^{2+} and

Table 1.4: Structural data and isomer shift for some divalent europium oxide compounds.

Compound	Structure	Coordination number	Average Eu^{2+}-O^{2-} distance	Isomer shift
EuO	NaCl	6	2.584	-11.26
Eu$_3$O$_4$	CaFe$_2$O$_4$	8	2.711	-11.6±0.1
Eu$_2$TiO$_4$	K$_2$NiF$_4$	9	- -	-11.76
EuTiO$_3$	Perovskite	12	2.75	-12.5±0.1
EuZrO$_3$	Perovskite	12	2.96	-13.1±0.2

Isomer shifts quoted in the literature relative to Eu$_2$O$_3$ are converted to values referred to EuF$_3$ by adding 1.037 mm/s to original data .

The values of isomer shift are cited from Ref. [5, 16, 21].

The crystal structure, coordination number and average Eu^{2+}−O distance are cited from Ref. [16, 22, 23].

Eu^{3+} ions deduced from the temperature dependence of recoil-free fraction were 145 and 261 K, respectively [15]. The result indicates that the chemical bond strength of Eu^{2+}−F is weaker than that of Eu^{3+}−F, and the recoil-free fraction of Eu^{2+} is smaller than that of Eu^{3+}. This is ascribable to the lower valence state and larger ionic radius of the Eu^{2+} ion. Hence, it is reasonable to consider that the Debye temperature, and hence, the recoil-free fraction, is smaller for Eu^{2+} than for Eu^{3+} in oxide glasses as well. As a result, it is definitely concluded that more than 99 % of the europium ions are present as a divalent oxidation state in the borate glasses with higher Na$_2$O contents.

Table 1.4 shows the values of isomer shift and the structural data for various oxide crystals of Eu^{2+} [5, 16, 21–23]. The isomer shift (IS) in oxide crystals

increases with a decrease in the coordination number and the average Eu$-$O bond distance. This indicates that IS is sensitive to the variation of the electric charge at the nucleus within the same oxidation state. Since the variation of electronic state of the outer 6s orbital mainly contributes to $|\Psi_A(0)|^2$ in Eq. (1.3) via the chemical bond with the ligand, the value of IS in ionic europium compounds with the divalent state is affected by the 6s electron density. This behavior was also reported in halide compounds (EuX$_2$, X= F, Cl, Br and I), where the value of IS decreases with an increase in the electronegativity of X, i.e., with a decrease in the covalency of Eu$^{2+}-$X bond [24]. Thus the value of IS of Eu^{2+} can be a measure of the covalency and coordination number in oxide solids. The change in IS of ^{151}Eu with covalency is opposite to the variation in IS of ^{57}Fe, because $\Delta < r^2 >$ in Eq. (1.3) is negative in the case of ^{57}Fe. In the Fe^{3+} -containing glasses, therefore, more covalent Fe$-$O bond shows the smaller value of IS, while more ionic Fe$-$O bond exhibits the larger value of IS [25, 26]. This tendency is explained on the basis of the contribution of 4s electron density to $|\Psi_A(0)|^2$ in Eq. (1.3), indicating that the value of IS of ^{57}Fe can be a measure of the covalency of Fe$-$O bond [27]. Thus, the value of IS of ^{57}Fe was used to determine whether Fe^{3+} ions occupy tetrahedral or octahedral sites in oxide glasses [28].

As shown in Tables 1.3 and 1.4, the isomer shifts of Eu^{2+} ions in borate glasses are comparable to or lower than those of EuTiO$_3$ and EuZrO$_3$, where the coordination number for Eu^{2+} is 12. Therefore the average coordination number for Eu^{2+} is considered to be 12 in the borate glasses studied here, and Eu^{2+} ions play a role of a network-modifying cation. In fact, it is well known that Eu^{2+} ions have chemical properties similar to the network-modifying cations such as Ca^{2+}, Sr^{2+} and Ba^{2+} [8,13]. The more negative value of IS in borate glasses than in the oxide crystals is probably brought about by the fact that the second nearest neighbor of Eu^{2+}, which forms chemical bonds

with O^{2-} ions surrounding Eu^{2+}, is a cation with an acid nature, i.e., B^{3+}. On the other hand, the value of IS is more positive in the present Eu^{2+} -containing borate glasses than in Eu^{2+} -containing fluorozirconate glass reported by Coey *et al.* [15], in which the value of IS is –14.18 mm/s, reflecting that the chemical bond between Eu^{2+} and oxygen is more covalent than that between Eu^{2+} and fluorine. This fact is ascribed to the difference of electronegativity between oxygen and fluorine.

The quadrupole interaction (QI) is expressed as eQ_gV_{zz}. V_{zz} is given by

$$V_{zz} = V_{zz}^{latt} + V_{zz}^{val}, \tag{1.12}$$

where V_{zz}^{latt} is the contribution of lattice and V_{zz}^{val} is the contribution of valence. In the case of Eu^{2+} with $^8S_{7/2}$ ground state, the resultant zero orbital angular momentum leads to no valence contribution. In other words, only lattice term appreciably contributes to V_{zz}. Thus, nonzero quadrupole parameter indicates that there is a deviation of the Eu^{2+} ion site from a cubic symmetry; the quadrupole parameter can be a measure of the pure lattice distortion around an Eu^{2+} ion.

A close look at Fig. 1.11 reveals that an increase in IS becomes sharp at $x = 0.2$ where the total concentration of Na_2O and EuO is nearly 30 mol%, and further the value of IS tends to increase as the concentration of Na_2O increases, indicating that a rapid increase in electron density at the nucleus takes place around this composition. This result is related with the role of Eu^{2+} in the borate glass structure. In sodium borate glasses, with increasing Na_2O content, the number of three-coordinated boron decreases and that of four-coordinated boron increases up to about 33 mol% Na_2O content, beyond which the four-coordinated boron begins to decrease, as demonstrated from [11]B nuclear magnetic resonance (NMR) measurements [29]. In the region of more than 29 mol% Na_2O content, it is considered that the nonbridging oxygen

begins to appear in sodium borate glass. On the other hand, the glass-forming region of the system containing EuO is similar in shape and size to that of the glass system containing CaO [8], and compositional dependence of the number of four-coordinated boron in the CaO-B$_2$O$_3$ system takes the same trend as that in the alkali borate glasses [30]. Therefore, it is reasonable that the number of nonbridging oxygens which coordinate an Eu^{2+} ion begins to increase when the total concentration of Na$_2$O and EuO is above 30 mol%. As a result, the electron density at the ^{151}Eu nucleus drastically increases in this compositional region, since the nonbridging oxygen has more electron donation-ability than the bridging oxygen and increases the 6s electron density effectively. This situation is reflected in the compositional dependence of QI as well, because the magnitude of QI can be a measure of the asymmetry in coordinating state of ligands around an Eu^{2+} ion as mentioned above. The introduction of Na$_2$O and EuO into the borate glass structure gives rise to oxide ions with different localized electron densities. This leads to an increase in the electric field gradient around an Eu^{2+} ion. Hence, the quadrupole interaction parameter increases until the total concentration of Na$_2$O and EuO reaches nearly 30 mol% as shown in Fig. 1.12. When the total concentration of Na$_2$O and EuO exceeds 30 mol%, the highly distorted local structure which is characterized by the nonbridging and bridging oxygens is formed around an Eu^{2+} ion. This speculation is coincident with the compositional dependence of γ value, which is due to the site-to-site variation of Eu^{2+}. As seen from Table 1.3, there is a tendency that the γ value is smaller in the glasses with high contents of Na$_2$O+EuO than in the glasses with low contents of Na$_2$O+EuO. The glass network structure is rigid in the region of less than 30 mol% Na$_2$O+EuO content because of the lack of nonbridging oxygens, so that Eu^{2+} ions must occupy a variety of sites, while the glass network structure is flexible in the region of more than 30 mol% Na$_2$O+EuO content due to the appearance of the nonbridging oxy-

gens, so that the nonbridging oxygens coordinate an Eu^{2+} ion more readily and the site-to-site variation becomes small in this region. From this viewpoint, it is considered that when Na$_2$O content is low, EuO converts three-coordinated boron atoms to four-coordinated ones, while when Na$_2$O content is high, the oxygens introduced by EuO work as nonbridging oxygens.

In order to evaluate the covalency of Eu^{2+}–O bond for all the compositions, an attempt is made to introduce the theoretical optical basicity (Λ) concept proposed by Duffy and Ingram [31, 32], allowing for the difference of the electronegativity between Na$^+$ and Eu^{2+} ions. The optical basicity concept is qualitatively supported by CNDO molecular orbital calculations [33]. It is defined as follows:

$$\Lambda = \sum_i \frac{z_i r_i}{2\gamma_i}, \tag{1.13}$$

where z_i is the oxidation number of the i-th cation, r_i is the ratio of the number of i-th cations with respect to the total number of oxide ions and γ_i is the moderating parameter, which is defined as

$$\gamma_i = 1.36(\chi_i - 0.26), \tag{1.14}$$

where χ_i is the electronegativity of Pauling as well as the electronegativity of Allred and Rochow [34]. Thus, γ_B, γ_{Na} and γ_{Eu} are 2.36, 0.87 and 1.02 respectively. Figure 1.13 shows the relationship between the value of IS and the calculated optical basicity. An increase in the optical basicity brings about an increase in the electron density of oxide ions which coordinate an Eu^{2+} ion. In other words, the optical basicity is a measure of electron-donating ability to probe ions, i.e., Eu^{2+} ions. The linear correlation suggests that the increase in electron density at the nucleus is mainly explained in terms of the increase in $6s$ electron, i.e., the increase in the covalency of the chemical bond between Eu^{2+} and oxygen, irrespective of glass compositions.
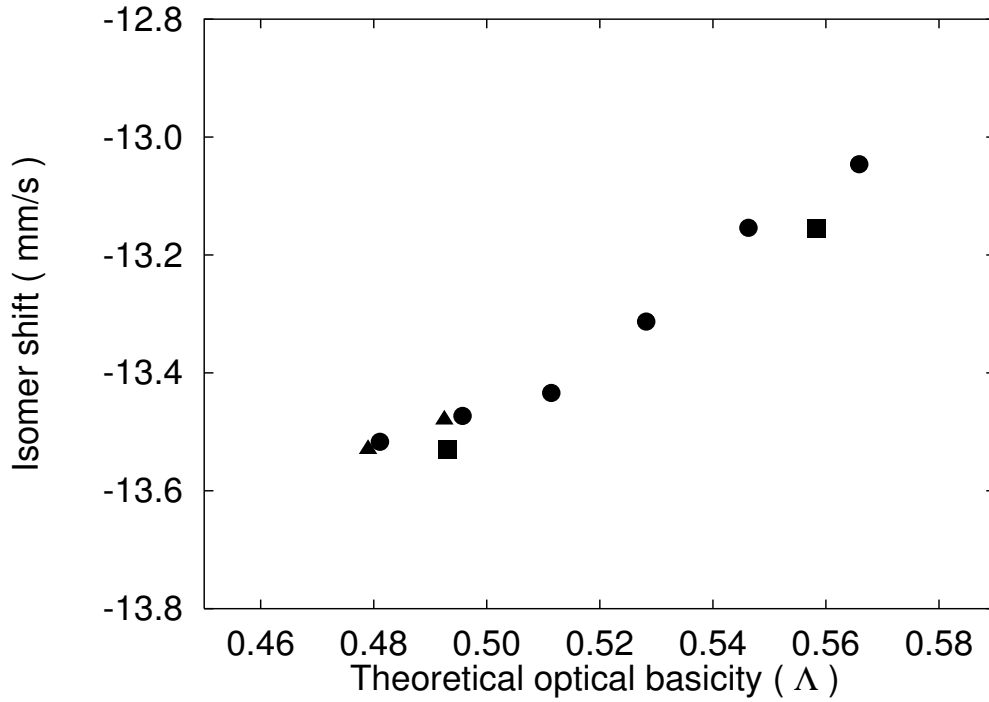
Figure 1.13: Relationship between isomer shift and calculated optical basicity for Eu^{2+} -containing borate glasses. $\bullet$: $15\text{EuO-}85\{x\text{Na}_2\text{O}\cdot(1-x)\text{B}_2\text{O}_3\}$, $\blacktriangle$: $x\text{EuO-}(100-x)\text{B}_2\text{O}_3$, $\blacksquare$: $20\text{EuO-}80\{x\text{Na}_2\text{O}\cdot(1-x)\text{B}_2\text{O}_3\}$

1.2.4.2 Silicate glasses

The isomer shifts of Eu^{2+} ions in alkali silicate glasses lie around –13.3 to –13.1 mm/s as shown in Table 1.3. From a comparison of these values with isomer shifts of Eu^{2+} ions in oxide crystals with different coordination numbers for Eu^{2+} ions as shown in Table 1.4, the average coordination number for Eu^{2+} in the alkali silicate glasses is estimated to be 12. The values of IS for the alkali silicate glasses are larger than those for the sodium borate glasses with low Na$_2$O contents. As found from Eq. (1.3), this result indicates that the 6s electron density at the nucleus is higher in the alkali silicate glasses than in

the sodium borate glasses. Also, the magnitude of QI of alkali silicate glasses is large compared with the sodium borate glasses. As argued in the previous section, the magnitude of QI of Eu^{2+} reflects only the electric field gradient caused by ligands. Thus, the large magnitude of QI in the alkali silicate glasses manifests that the distribution of negative charge supplied by twelve oxide ions around an Eu^{2+} ion are more asymmetrical in the alkali silicate glasses than in the sodium borate glasses. Since the chemical properties of Eu^{2+} are very similar to those of Ca^{2+}, Sr^{2+}, and Ba^{2+}, which are prototypes of network-modifying cations in the random network structure of the oxide glasses, it is thought that Eu^{2+} ions also act as a network-modifying cation. Namely, the Eu^{2+} ions incorporated into the silicate glasses break Si-O-Si bonds and create nonbridging oxygens. The high electron density of nonbridging oxygens brings about the large value of IS. In contrast, Eu^{2+} ions are surrounded by only bridging oxygens in sodium borate glasses with low Na$_2$O content, resulting in the small value of IS. As for the sodium aluminosilicate glasses, the IS decreases with an increase in the concentration of Al$_2$O$_3$. This is because Al^{3+} incorporated in the sodium silicate glass forms AlO$_4^-$ which takes part in the glass network and coordinates an Eu^{2+} ion via bridging oxygens when the ratio of Al$_2$O$_3$ to Na$_2$O is less 1. In other words, the increase in the concentration of Al$_2$O$_3$ decreases the number of nonbridging oxygens in the sodium silicate glasses, leading to the decrease in IS.

The fraction of the absorption area due to Eu^{2+} with respect to the total absorption area of Mössbauer spectrum is about 80 % for all the glasses. The value is less for the alkali silicate glasses than for the sodium borate glass. This is because the basicity of the local environment around an europium ion is higher in the alkali silicate glasses that in the sodium borate glasses. As Winterer *et al.* [13] revealed using the Mössbauer spectroscopy for alkali borate glasses, the ratio of Eu^{3+} to Eu^{2+} increases as the basicity of glass increases.

1.2.5 Conclusion

Sodium borate and alkali silicate glasses containing Eu^{2+} ions were prepared under a strong reducing condition, and the valence state of Eu and the chemical and electronic structure of Eu^{2+} were examined by means of ^{151}Eu Mössbauer spectroscopy.

For the sodium borate glasses, almost all the europium ions are present in the divalent oxidation state, the contribution of quadrupole splitting and the contribution of structure disorder in glass are separated from each other in the absorption line which is significantly broader than that of cubic EuS. The behavior of isomer shift and quadrupole interaction at around 30 mol% Na$_2$O+EuO content is related with the appearance of nonbridging oxygen. Compositional dependence of the isomer shift is correlated well with the optical basicity of the borate glass, indicating that the electron donation from oxide ions mainly affects the 6s orbital. The average coordination number for Eu^{2+} is found to be twelve, and Eu^{2+} ions are rather homogeneously distributed as a network-modifying cation irrespective of the Na$_2$O content.

As for the alkali silicate glasses, about 80 % of europium ions are present in the divalent oxidation state. The value of isomer shift and the magnitude of quadrupole interaction are larger in the alkali silicate glasses than in the sodium borate glasses with low Na$_2$O contents. The facts indicate that the 6s electron density is higher and the distribution of negative charge due to oxide ions around an Eu^{2+} ion is more asymmetrical in the alkali silicate glasses than in the sodium borate glasses. Based on these results, it is considered that Eu^{2+} ions incorporated into the silicate glass break Si-O-Si bonds and produce nonbridging oxygens.

References

[1] R. L. Mössbauer, Z. Phys. **151**, 124 (1958).

[2] E. R. Bauminger, G. M. Kalvius, and I. Nowik, in *Mössbauer Isomer Shifts*, edited by G. K. Shenoy and F. E. Wagner (North-Holland, Amsterdam, 1978), p. 661.

[3] J. G. Stevens, in *CRC Handinbook of Spectroscopy*, edited by J. W. Robinson (CRC press, Boca Raton, Florida, 1981), Vol. III, p. 464.

[4] E. A. Samuel and W. N. Delgass, in *Mössbauer Effect Methodology*, edited by I. J. Gruverman and C. W. Seidel (Plenum Press, New York, 1976), Vol. 10, p. 261.

[5] C. L. Chien, S. DeBenedetti, and F. D. Barros, Phys. Rev. B **10**, 3913 (1974).

[6] G. K. Shenoy and B. D. Dunlap, Nucl. Instrum. Methods **71**, 285 (1969).

[7] K. Hirao, S. Todoroki, D. H. Cho, and N. Soga, Opt. Lett. **18**, 1586 (1993).

[8] M. W. Shafer and J. C. Suits, J. Am. Ceram. Soc. **49**, 261 (1966).

[9] K. Tanaka, T. Ohyagi, K. Hirao, and N. Soga, Bull. Chem. Soc. Jpn. **66**, 1121 (1993).

[10] S. Tanabe, K. Hirao, and N. Soga, J. Non-Cryst. Solids **113**, 178 (1989).

[11] M. F. Taragin and J. C. Eisenstein, Phy. Rev. B **2**, 3490 (1970).

[12] J. A. Hodges, G. Jehanno, and J. M. Friedt, Hyperfine Interact. **27**, 365 (1986).

[13] M. Winterer, E. Morsen, B. D. Mosel, and W. Muller-Warmuth, J. Phys. C **20**, 5389 (1987).

[14] G. Concas, F. Congiu, C. Muntoni, M. Bettinelli, and A. Speghini, Phys. Rev. B **53**, 6197 (1996).

[15] J. M. D. Coey, A. McEvoy, and M. W. Shafer, J. Non-Cryst. Solids **43**, 387 (1981).

[16] O. Berkooz, J. Phys. Chem. Solids **30**, 1763 (1969).

[17] K. Tanaka, K. Kamiya, T. Yoko, S. Tanabe, K. Hirao, and N. Soga, Phys. Chem. Glasses **32**, 16 (1991).

[18] K. Fujita, K. Tanaka, K. Hirao, and N. Soga, J. Appl. Phys. **81**, 924 (1997).

[19] J. Shoenes, E. Kaldis, W. Thöni, and P. Wachter, Phys. Status Solidi A **51**, 173 (1979).

[20] B. A. Goodman, N. N. Greenwood, and G. E. Turner, Chem. Phys. Lett. **5**, 181 (1970).

[21] G. Gerth, P. Kienle, and K. Luchner, Phys. Lett. **27A**, 557 (1968).

[22] R. C. Rau, Acta. Cryst. **20**, 716 (1966).

[23] M. W. Shafer, J. Appl. Phys. **36**, 1145 (1965).

[24] F. Grandjean and G. J. Long, in *Mössbauer Spectroscopy Applied To Inorganic Chemistry*, edited by G. J. Long and F. Grandjean (Plenum Press, New York, 1989), Vol. 3, p. 513.

[25] C. R. Kurkjian and D. N. Buchanan, Phys. Chem. Glasses **5**, 63 (1964).

[26] K.Tanaka and N. Soga, J. Non-Cryst. Solids **95-96**, 255 (1987).

[27] L. R. Walker, G. K. Wertheim, and V. Jaccarino, Phys. Rev. Lett. **6**, 98 (1970).

[28] C. R. Kurkjian and E. A. Sigety, Phys. Chem. Glasses **9**, 73 (1968).

[29] P. J. Bray and J. G. O. Keefe, Phys. Chem. Glasses **44**, 37 (1963).

[30] S. G. Bishop and P. J. Bray, Phys. Chem. Glasses **7**, 73 (1966).

[31] J. A. Duffy and M. D. Ingrum, J. Non-Cryst. Solids **21**, 21 (1976).

[32] J. A. Duffy and M. D. Ingrum, J. Inorg. Nucl. Chem. **37**, 1203 (1975).

[33] J. H. Binks and J. A. Duffy, J. Non-Cryst. Solids **37**, 387 (1980).

[34] J. E. Huheey, E. A. Keiter, and R. L. Keiter, in *Inorganic Chemistry, Principles of Structure and Reactivity*, fourth ed. (Harper Collins College, New York, 1993), pp. 188–189.

Chapter 2

Site-dependent optical properties of rare-earth ions in glasses

2.1 Site-selective spectroscopy of rare-earth ions in glasses by tunable laser

Due to the randomness of the local environment in glasses, there is a distribution of physically different sites. Various spectroscopies, such as magnetic resonance, diffraction, vibrational and Mössbauer spectroscopy, yield information about glass structure. The methods such as isotopic substituted neutron diffraction, X-ray absorption fine structure, and anomalous dispersion offer information about a specific atom in a glass. The measured quantities, however, still involve a weighted summation over an ensemble of individual sites.

A distinguishing feature of laser spectroscopy is that it is site or energy selective. Only impurity ions in sites having electronic transitions resonant with the laser frequency are excited and observed. By using a narrow band tunable laser, an entire distribution of sites can be extracted. This yields the valuable information which is not available with conventional optical spectroscopy. If a broadband light source is used to excite rare-earth ions in glasses, all ions are excited and an inhomogeneously broadened emission with the linewidth of Γ_{ih} is obtained, as illustrated at the lower side in Fig. 2.1. If, instead, a laser is used for excitation, only those ions resonant with the laser frequency are excited, and
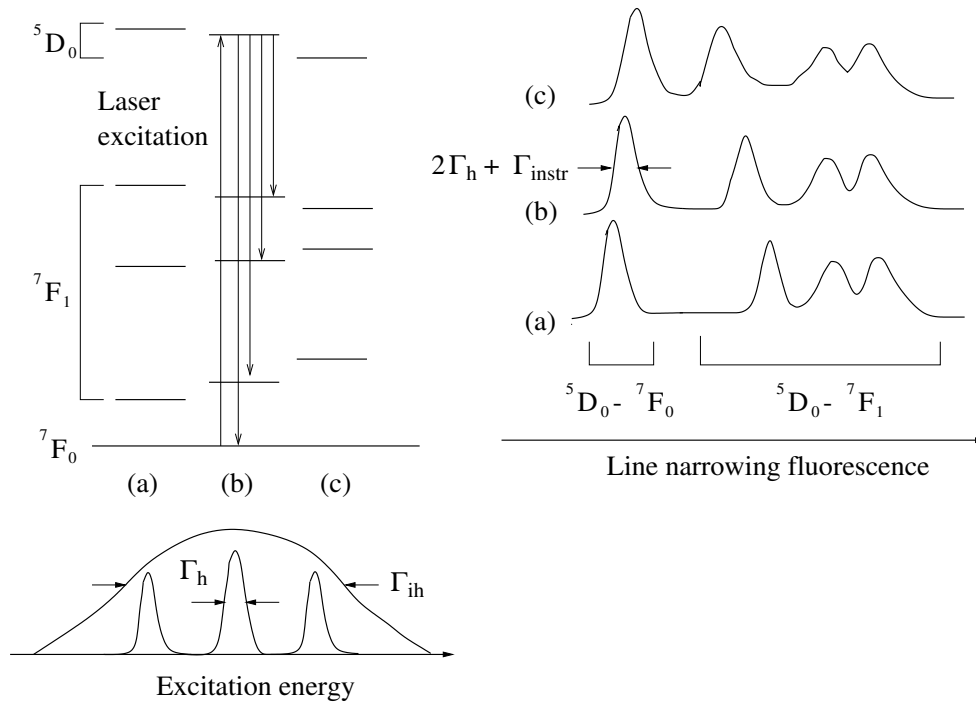
Figure 2.1: Principle of fluorescence line narrowing.

fluorescence from the subset of ions will be narrow, as shown at the right side in Fig. 2.1, where the narrow fluorescence lines are shown following excitation into the $^5D_0$ level of Eu^{3+}. Laser-induced fluorescence line narrowing (FLN) is an effective tool for elucidating the homogeneous linewidth (Γ_h) of optical centers in glasses. When $\Gamma_h < \Gamma_{ih}$, the line-narrowing fluorescence due to the $^5D_0 \rightarrow {}^7F_0$ transition of Eu^{3+} has a width of $2\Gamma_h$ (because both excitation and emission processes are involved) plus any instrumentation width (Γ_{instr}) caused by the laser linewidth or the resolution of detection system [1]. Consequently, the value of Γ_h can be estimated from the careful analysis of FLN spectra. However, it is hard to measure Γ_h by means of the FLN technique below about 10 K, at which instrumental limitations usually dominate. In this respect, spectral hole burning, whose resolution is limited by the spectral

resolution of laser linewidth, has the advantage of FLN (see Chapter 3).

On the other hand, non-resonant fluorescence transitions also exhibit line narrowing. This is illustrated for the $^5D_0 - {}^7F_1$ fluorescence triplet of Eu^{3+} at the right side in Fig. 2.1. A large variation in crystal-field (Stark) splitting of the $^7F_1$ state is observed as the laser wavelength is tuned across the $^7F_0 \to {}^5D_0$ absorption profile. When pulsed excitation is used, the site-to-site variations in the radiative and non-radiative transition probabilities of rare-earth ions in glasses can also be measured from the decay of line narrowing fluorescence [2–4]. Brecher and Riseberg [2,3], in an early pioneering study, analyzed the FLN spectra of $^5D_0 - {}^7F_{1,2}$ transitions of Eu^{3+} in silicate and fluoroberyllate glasses, and proposed two geometric models for the environment around Eu^{3+}. Brawer and Weber [5] carried out the simulation of glass structure by Monte Calro methods and molecular dynamics calculations. They reproduced the observed FLN spectra using crystal field parameters deduced on the basis of a point charge model, and evaluated the energy levels of Eu^{3+} in a fluoroberyllate glass. Several later studies then investigated the structure of glass using the FLN method.

The FLN spectra yield useful information about the local structure around optical centers, the vibrational modes of host matrices, and so on. In $4f - 4f$ transitions of trivalent rare-earth ions, the FLN effect is observed readily, because the homogeneous linewidths of the $4f - 4f$ transitions are often much narrower than the inhomogeneous linewidths, especially at low temperatures. This is because of the weakness of the coupling between the $4f$ electrons and the host material, which results from the shielding of the $4f$ electrons from the surroundings by the outer $5s^2 5p^6$ electrons. Furthermore, since the wave functions of the free-ion states of the trivalent rare-earth ions are well known, the symmetry of ion site and the strength of local field acting on the ion can be determined relatively easily from the numbers and magnitudes of the splittings

of J manifolds, respectively. For these reasons, trivalent rare-earth ions have often been employed in the FLN experiments as useful probes of the local environment of these ions. In particular, the FLN spectra of the $^5D_0 - {}^7F_{0,1,2,}$ transitions of Eu^{3+} have been extensively studied because of its simple energy level structure, that is, the fact that it has non-degenerate ground ($^7F_0$) and excited states ($^5D_0$). The electronic structure of Eu^{3+} and Sm^{2+} ions is almost identical with each other because of isoelectronic configuration ($4f^6$). Hence, in principle, the FLN technique can be applied to Sm^{2+}. However, in many cases, the $4f-4f$ transitions are scarcely observed because the parity-allowed intense $4f^6 \rightarrow 4f^55d$ transition overlaps the $4f-4f$ transitions in the visible region [6]. Therefore, few FLN experiments for glasses doped with Sm^{2+} ions have been reported. In Section 2.2, the FLN experiments are performed for not only Sm^{2+}-doped sodium borate glasses, in which the intense $4f^55d$ band does not mask $^5D_0$ state but also Eu^{3+}-doped sodium borate glasses.

2.2 Fluorescence line narrowing spectroscopy of Sm^{2+} and Eu^{3+} in sodium borate glasses

2.2.1 Introduction

Rare-earth -doped glasses have been arresting a great deal of attention because of their potential application to optical devices such as an upconversion laser and a hole burning high-density memory. The homogeneous linewidth of optical transition for rare-earth-doped glasses is affected by the local structure of rare-earth ions. However, the inhomogeneous properties and disorder in glasses complicate information relevant to each of optical centers. Thus, many attempts have been made to excite selectively a subset of rare earth ions within the inhomogeneous line width in glass matrix and to relate the site-dependent optical properties with local structure [2–4, 7–13]. Laser-induced fluorescence line narrowing (FLN) has been effectively used to evaluate a distribution of local environment around rare-earth ions.

Another attempt which extracts only a subset of ions within the inhomogeneous broadening was performed utilizing measurements of spectral hole burning which gives us the high resolution probe. So far, persistent and transient spectral holes have usually been burned only at low temperatures for glasses doped with various rare-earth ions [14–16]. Recently, persistent spectral hole burning (PSHB) has been reported in Sm^{2+} -doped oxide and fluoride glasses at room temperature [17–19]. A large inhomogeneous linewidth which reflects disorder in glass is advantageous for the application of PSHB materials to frequency and time domain optical memories. As for spectral hole burning and FLN in Eu^{3+} -doped glasses, a decrease in homogeneous linewidth with increasing excitation frequency within the inhomogeneously broadened $^7F_0 \rightarrow {}^5D_0$ absorption line of Eu^{3+} was reported for several kinds of glasses at

room and liquid helium temperatures [17, 20]. Also, the fluorescence lifetime of $^5D_0$ state was reported to change with the variation of crystal field strength within the inhomogeneous linewidth, which corresponds to the site-to-site variation [2]. Thus, it is important to study the site-dependent optical properties of rare-earth ions from the technological and basic research standpoint.

The aim of this study is to examine the site-dependent optical properties relevant to the inhomogeneously broadened $^5D_0 \leftarrow {}^7F_0$ line for sodium borate glasses doped with Sm^{2+} ions. Moreover, the site-dependent optical properties for sodium borate glasses doped with Sm^{2+} ions are compared with those for sodium borate glasses doped with Eu^{3+} ions. The results are discussed in connection with effect of these ions on the glass-forming ability.

2.2.2   Experimental procedure

2.2.2.1   Preparation of glass

The compositions of glass samples examined in this work are summarized in Table 2.1. Glasses were prepared from reagent-grade Eu_2O_3, Sm_2O_3, Na_2CO_3 and B_2O_3 as starting materials. These raw materials were thoroughly mixed, and melted in a platinum crucible at 1100 °C for 30 min in air so as to eliminate carbon dioxide from the melt. The melt was poured onto a stainless steel plate to obtain glass. As for the Sm^{3+} -containing system, the resultant glass was remelted in a graphite crucible in a strongly reducing atmosphere at 1350∼1400 °C for 30 min in order to convert Sm^{3+} to Sm^{2+} ions. For the Eu^{3+} -containing system, the glass was remelted in a platinum crucible at 1350∼1400 °C for 30 min in air.

The reduction condition was attained using $Ar(94)/H_2(6)$ (vol%) gas in an electric furnace composed from a graphite heater, an insulator and a water jacket. The glass thus obtained was cut and polished into a rectangular shape

Table 2.1: Glass compositions (in mol%) and the melting condition.

Composition	x	atmosphere during melting
$(100-x)\mathrm{B_2O_3}\cdot x\mathrm{Na_2O}\cdot$ $(1.0\mathrm{Eu_2O_3}$ or $0.1\mathrm{Eu_2O_3})$	10,15,20	in air
$(100-x)\mathrm{B_2O_3}\cdot x\mathrm{Na_2O}\cdot$ $(2.0\mathrm{SmO}$ or $0.2\mathrm{SmO})$	10,15,20	in $\mathrm{Ar}(94)/\mathrm{H_2}(6)$ atmosphere

of $5 \times 5 \times 3$ mm³ for measurements of optical properties.

2.2.2.2 Optical Measurements

Fluorescence and excitation spectra were obtained using a fluorescence spectrometer with a Xe lamp as a light source (Hitachi-850). For the glasses containing samarium, the excitation wavelength was fixed at 400nm, where $\mathrm{Sm^{2+}}$ and $\mathrm{Sm^{3+}}$ ions exhibit absorption bands ascribed to $4f^6 \to 4f^5 5d$ and spin-allowed $^6H_{9/2} \to^6 P_J$ transitions, respectively [21]. For the glasses containing europium, the excitation wavelength was 394 nm. The excitation spectra were measured by monitoring the peak positions of the $^5D_0 \to {}^7F_2$ transitions for $\mathrm{Sm^{2+}}$ and $\mathrm{Eu^{3+}}$ ions, respectively.

FLN measurements were carried out as follows. The glass sample was maintained at 10 to 300 K in a closed cycle helium refrigerator (Iwatani CRT, 006-2000). Excitation was accomplished by a tunable pulsed dye laser (Spectra Physics, PDL-3, a mixture of rhodamin 6G and rhodamin B dyes for $\mathrm{Eu^{3+}}$, and a mixture of LDS698 and DCM dyes for $\mathrm{Sm^{2+}}$), which was pumped by a frequency doubled Nd-YAG laser (Spectra Physics, GCR-11). The output pulse had a duration of 6 ns and a typical linewidth of 0.07 cm⁻¹

at a repetition rate of 10 Hz. Excitation wavelength was tuned within the range corresponding to the $^7F_0 \rightarrow {}^5D_0$ absorption line in the excitation spectrum. Emission from the sample the direction of which was perpendicular to the exciting laser beam was passed through a monochromator (Ritu, MC-25NP, 25 cm, resolution ~ 2 cm^{-1}). Signals were detected with a photomultiplier (PM) (Hamamatu Photonics, R955). The same experimental setup was used for the measurements of time-resolved fluorescence spectra and fluorescence lifetime as shown in Fig. 2.2. In the former case, PM signals were accumulated with a boxcar integrator (Stanford Research systems, SR250) and, in the latter case, the signals were stored using a digital storage oscilloscope (Tektoronics TDS310, 300 MHz bandwidth).
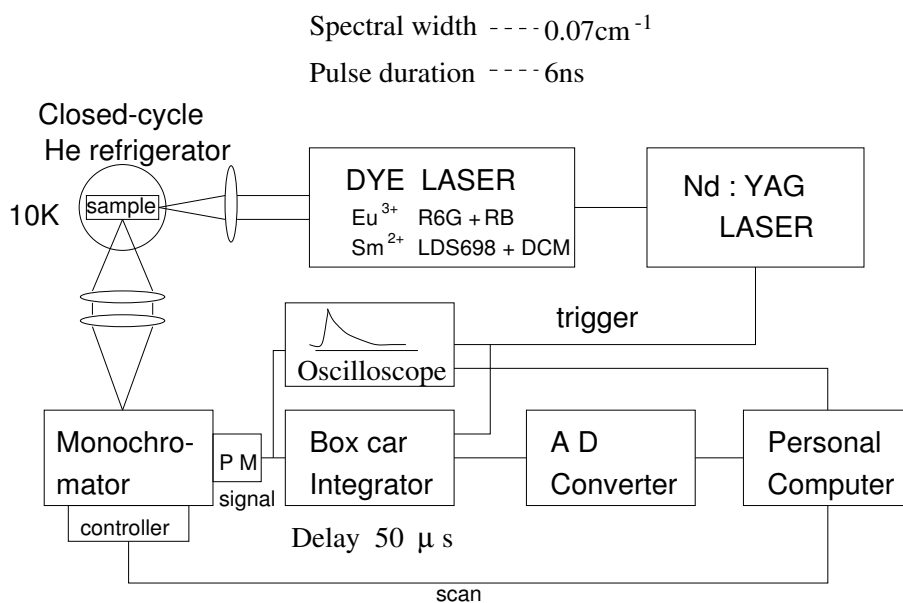
Figure 2.2: Schematic illustration of the equipment for time-resolved FLN measurements.

2.2.3 Results

Figures 2.3(a) and (b) show the fluorescence spectra for $85B_2O_3 \cdot 15Na_2O \cdot 2.0SmO$ and $85B_2O_3 \cdot 15Na_2O \cdot 1.0Eu_2O_3$ glasses at room temperature. Emission lines assigned to the $^4G_{5/2} \rightarrow {}^6H_J$ (J=5/2, 7/2, 9/2) transitions of Sm^{3+} that would appear in the range between 15000 and 18000 cm^{-1} are not observed in contrast with the case of Sm^{2+} -doped fluorohafnate glass reported previously [21]. This fact clearly indicates that almost all the samarium ions are present as Sm^{2+} ions in the present glass. This is attained because of the higher melting temperature and larger fraction of hydrogen in melting atmosphere compared to the case of fluorohafnate glass. The excitation spectra of $85B_2O_3 \cdot 15Na_2O \cdot 2.0SmO$ and $85B_2O_3 \cdot 15Na_2O \cdot 1.0Eu_2O_3$ glasses at 10 K are shown in Figs. 2.4(a) and (b), respectively. For Sm^{2+}, the $^7F_0 \rightarrow {}^5D_0$ transi-
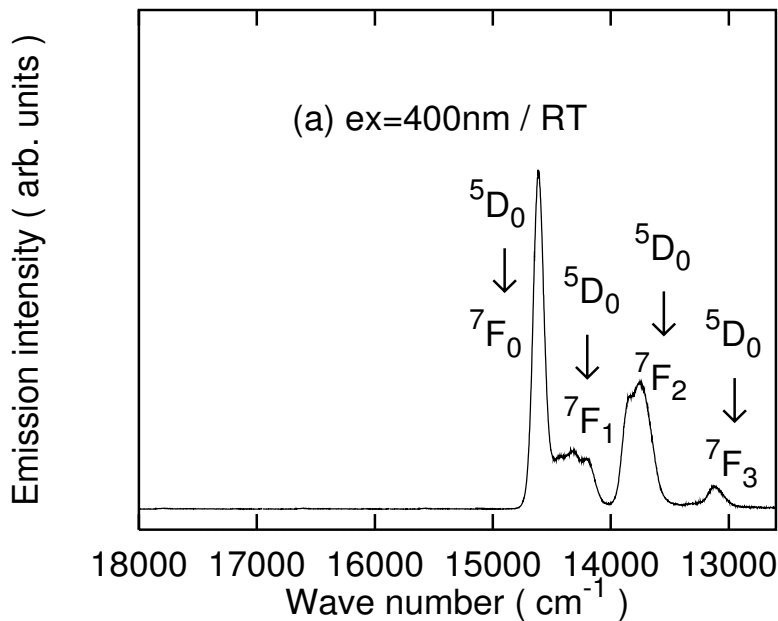
Figure 2.3: Fluorescence spectra for (a) $85B_2O_3 \cdot 15Na_2O \cdot 2.0SmO$ and (b) $85B_2O_3 \cdot 15Na_2O \cdot 1.0Eu_2O_3$ glasses at room temperature.
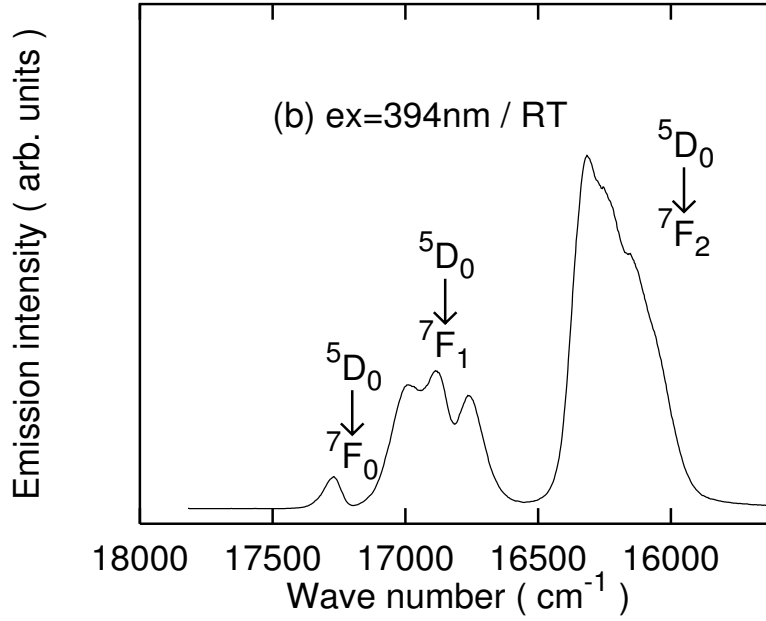
Figure 2.3: (*Continued.*)

tion is clearly observed without a hindrance by the $4f^6 \rightarrow 4f^5 5d$ transition. The inhomogeneous linewidth for both spectra is estimated to be of the same order of magnitude to each other.

Figures 2.5 and 2.6 show FLN spectra of the $^5D_0 \rightarrow {}^7F_1$ transition for $85B_2O_3 \cdot 15Na_2O \cdot 1.0Eu_2O_3$ and $85B_2O_3 \cdot 15Na_2O \cdot 2.0SmO$ glasses at 10 K, respectively. In Figs. 2.5 and 2.6, three lines, noticeablely markedly separated from each other, are denoted as ϵ_+, ϵ_- and ϵ_0 in the order of energy. Some energy transfers were reported to take place within a few milliseconds after excitation of Eu^{3+} -doped oxide and fluoride glasses [22]. On the basis of this result, in order to suppress the energy transfer as efficiently as possible, the present measurements were carried out with a gate width of 3 μs at a delay of 50 μs. Both spectra manifest gradual and systematic changes when the excitation energy is increased. In general, the spectral line of the $^7F_1$ term
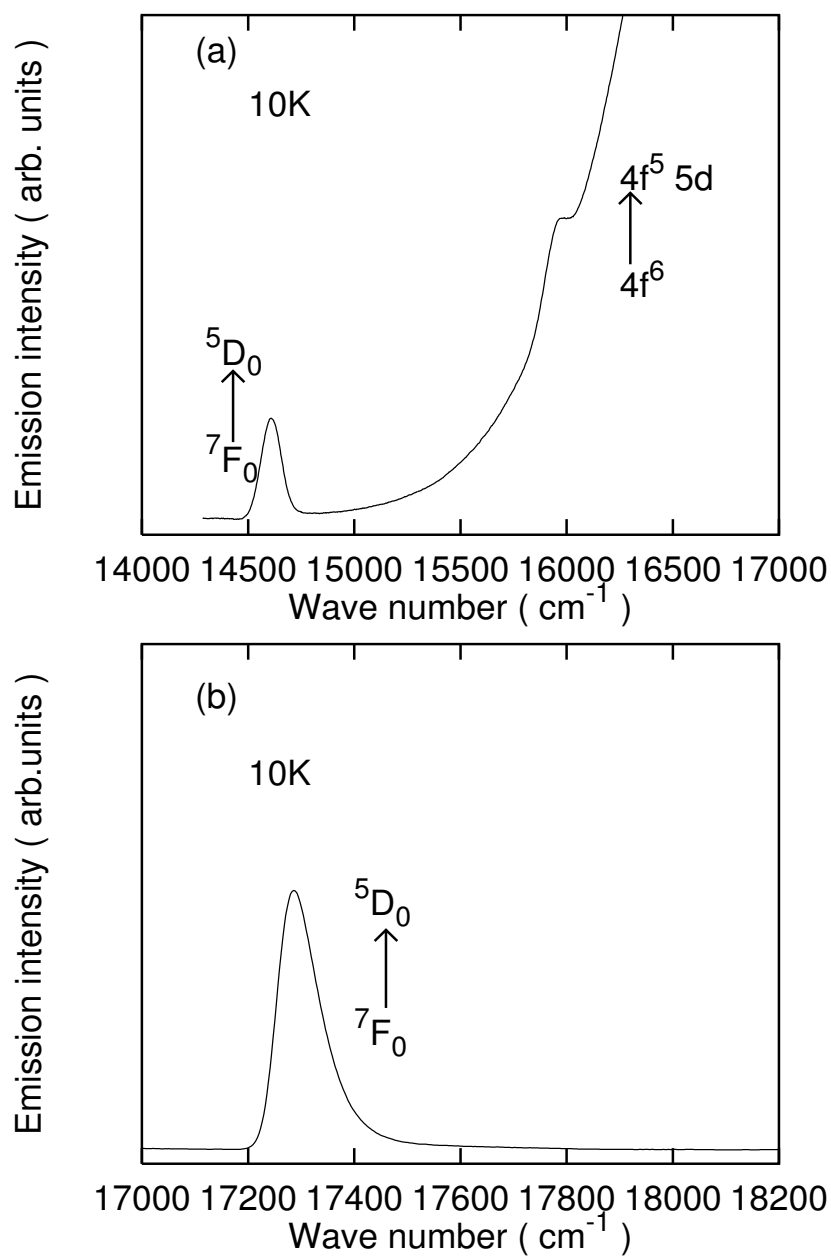
Figure 2.4: Excitation spectra of the $^5D_0 \rightarrow {}^7F_2$ transition for (a) $85B_2O_3 \cdot 15Na_2O \cdot 2.0SmO$ and (b) $85B_2O_3 \cdot 15Na_2O \cdot 1.0Eu_2O_3$ glasses at 10 K.
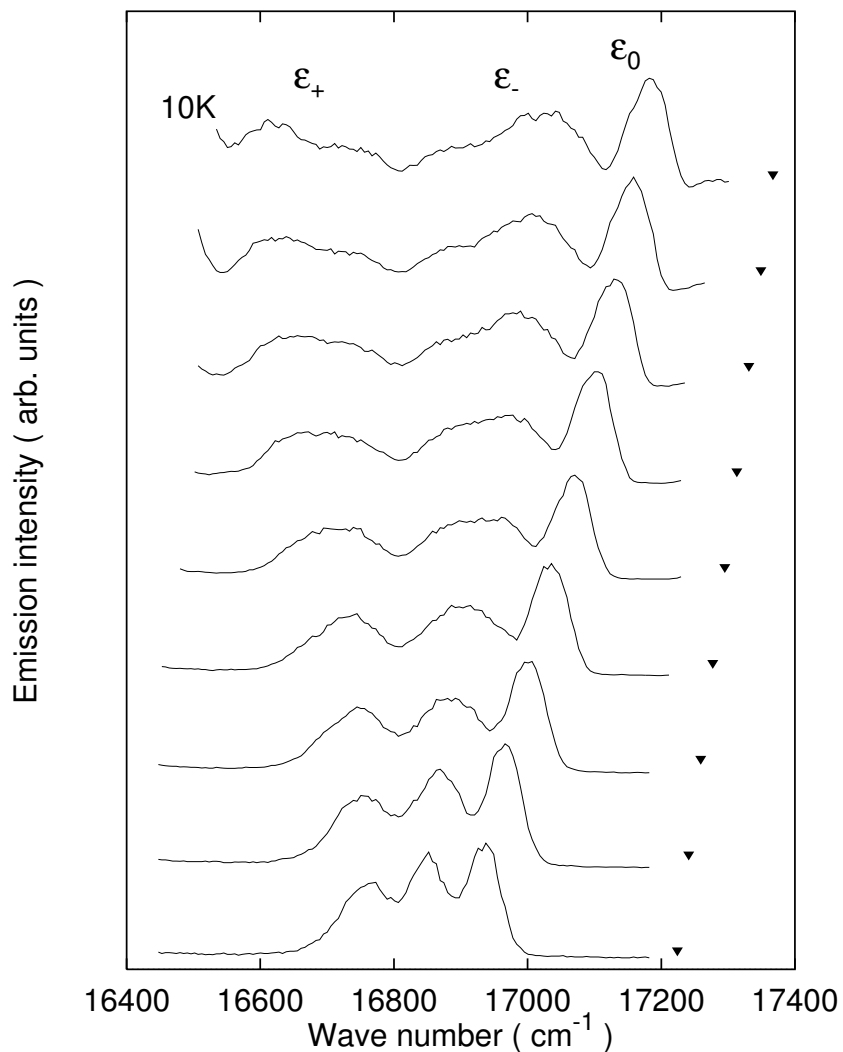
Figure 2.5: FLN emission spectra of the $^5D_0 \rightarrow {}^7F_1$ transition of Eu^{3+} in $85B_2O_3 \cdot 15Na_2O \cdot 1.0Eu_2O_3$ glass. The fluorescence spectra were measured with a time delay 50 μs after a pulsed laser excitation at 10 K. Excitation energies are denoted by triangles.

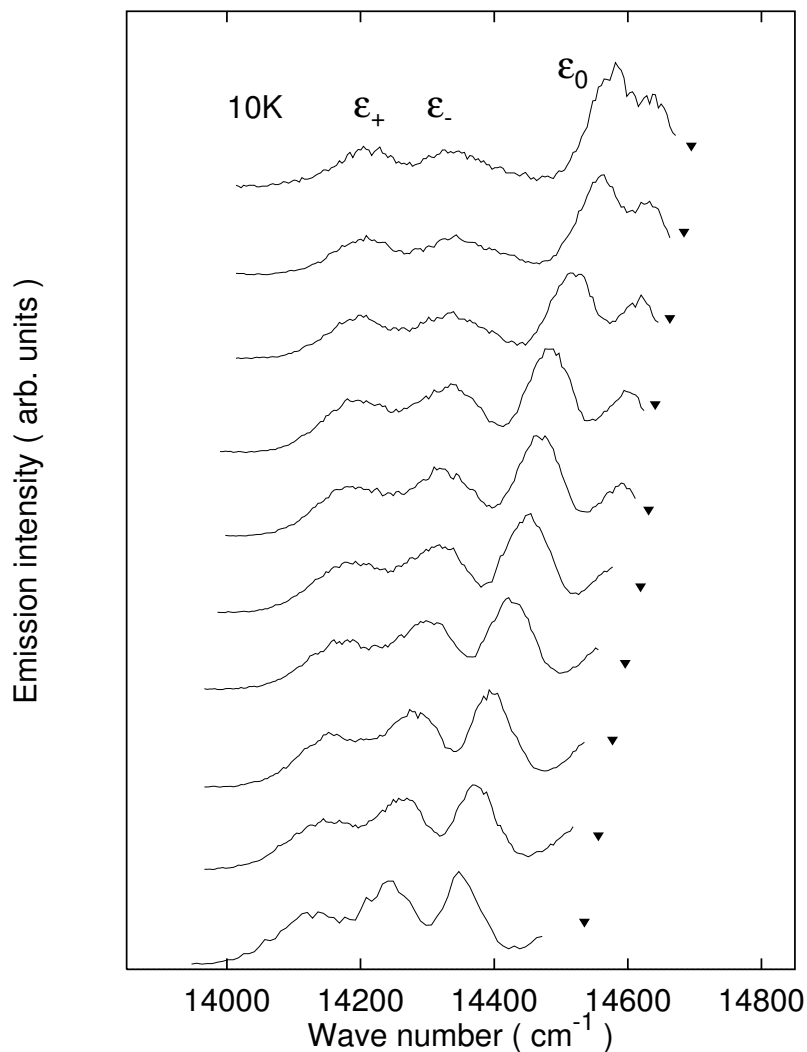Figure 2.6: FLN emission spectra of the $^5D_0 \to {}^7F_1$ transition of Sm^{2+} in $85B_2O_3 \cdot 15Na_2O \cdot 2.0SmO$ glass. The fluorescence spectra were measured with a time delay of 50 μs after a pulsed laser excitation at 10 K. Excitation energies are denoted by triangles.

consists of three components because the $^{2s+1}L_J$ level is at most split into $2J$ + 1 states when the symmetry of local crystal fields is less than C_{2v} [23]. For Eu^{3+}, however, more than three peaks are observed when the excitation energy is high. A similar phenomenon was reported by Weber *et al.* [7] for lithium borate glasses doped with Eu^{3+} ions. On the contrary, for Sm^{2+}, an additional peak appears only at around 14600 cm^{-1} when the excitation energy is high.

FLN experiments were carried out for 0.2 mol% rare-earth ions -containing glasses as well. In order to analyze the FLN emission spectra in detail, a multidimensional nonlinear least squares fit was attempted. Here, so as to take into account the energy transfer which can not be removed perfectly and/or simultaneous excitation of different types of sites, the fittings for these spectra were carried out assuming six or seven Gaussian distribution functions. Figures 2.7 and 2.8 show the experimental and calculated FLN emission spectra for $85B_2O_3 \cdot 15Na_2O \cdot xEu_2O_3$ glasses with $x = 0.1$ and 1.0 at 17331 cm^{-1} excitation energy and $85B_2O_3 \cdot 15Na_2O \cdot xSmO$ glasses with $x = 0.2$ and 2.0 at 14684 cm^{-1} excitation energy, respectively. For 2.0 mol% Eu^{3+}, the spectral lines apparently consist of discrete six components. As for 2.0 mol% Sm^{2+}, on the other hand, the second, fourth and fifth emission peaks in the order of energy are much weaker than the other emission peaks, and therefore the spectral lines are mainly composed of three components, except for the highest energy component due to $^5D_0 - {}^7F_0$ line ascribed to energy transfer, as will be discussed. Furthermore, a close look at Figs. 2.7 and 2.8 indicates for Sm^{2+}, the profile of spectrum seems to ignore of the concentration of Sm^{2+}, while for Eu^{3+}, the first, fourth and sixth emission peaks (this group is designated as α) in the order of energy become more dominant than the second, third and fifth components (group β) as the concentration of Eu^{3+} decreases.

The peak energies of $^7F_1$ manifolds for Sm^{2+} and Eu^{3+} ions in the sodium borate glasses with Na_2O contents of $10-20$mol % are plotted against the exci-
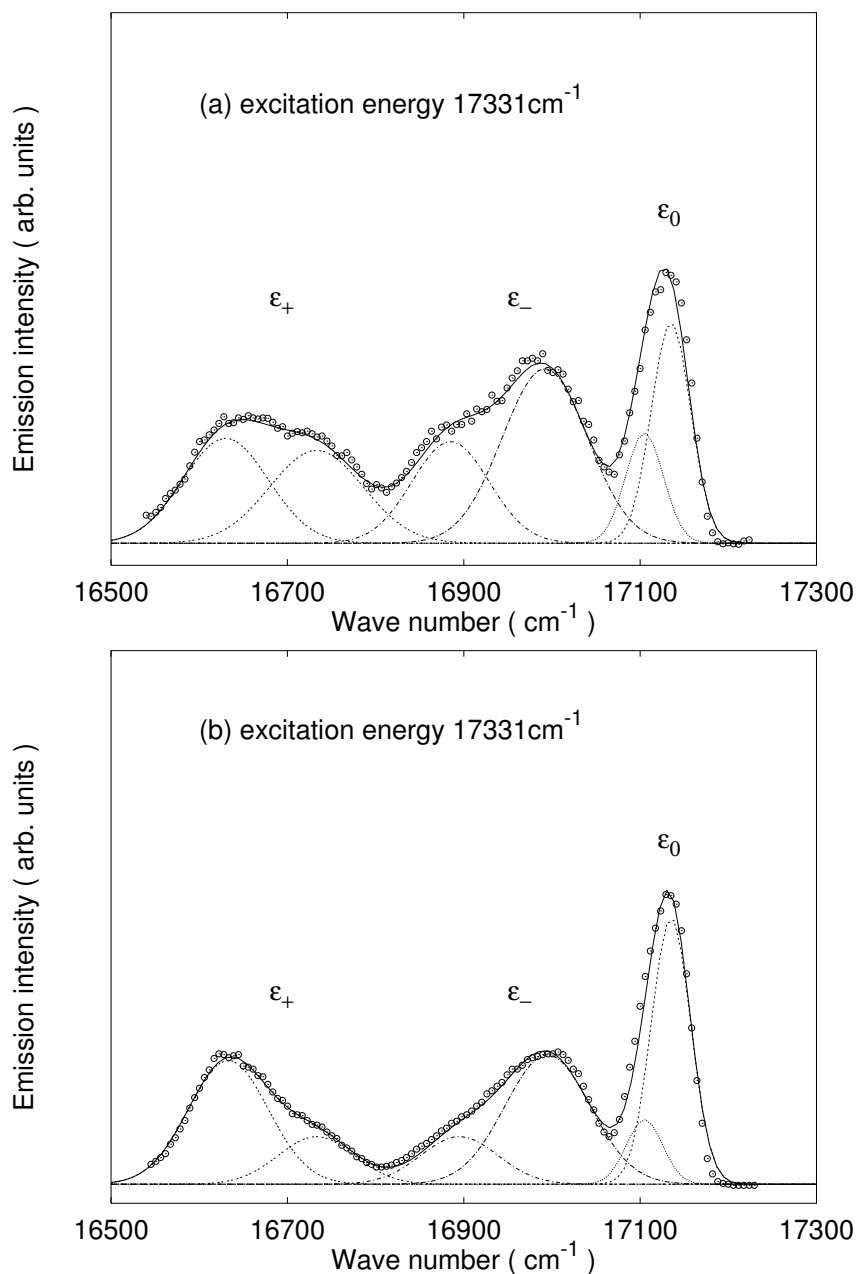
Figure 2.7: Experimental (dotted curve) and caluculated (solid curve) FLN emission spectra for $85B_2O_3 \cdot 15Na_2O \cdot xEu_2O_3$ glasses with (a) $x = 1.0$ and (b) $x = 0.1$. Excitation energy is 17331 cm^{-1}.
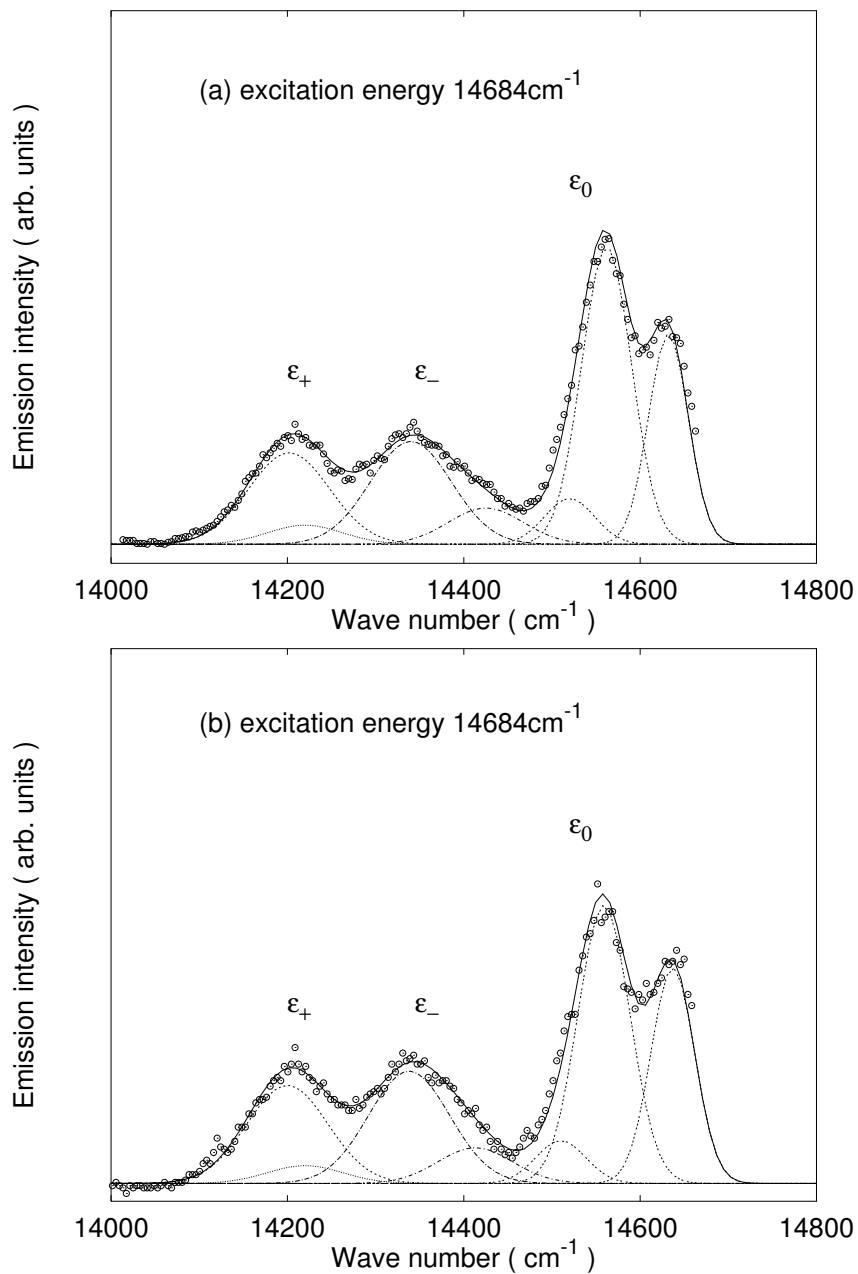
Figure 2.8: Experimental (dotted curve) and caluculated (solid curve) FLN emission spectra $85B_2O_3 \cdot 15Na_2O \cdot xSmO$ glasses with (a) $x = 2.0$ and (b) $x = 0.2$. Excitation energy is 14684 cm^{-1}.
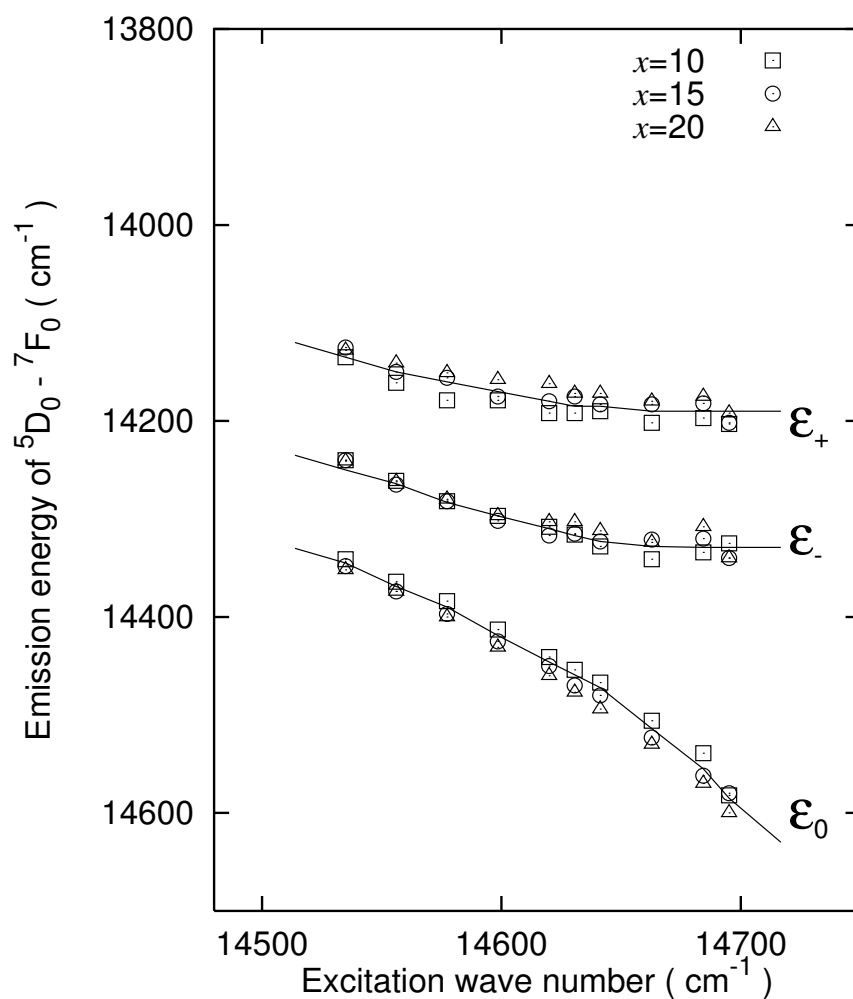
Figure 2.9: Dependence of peak energies of $^7F_1$ Stark components on excitation energy for $(100-x)$B$_2$O$_3$·xNa$_2$O·ySmO glasses with $x = 10$, 15, 20 and $y = 2.0$ and 0.2. Since the experimental results for $y = 2.0$ and 0.2 are nearly identical to each other, the peak energies for $y = 0.2$ are presented.
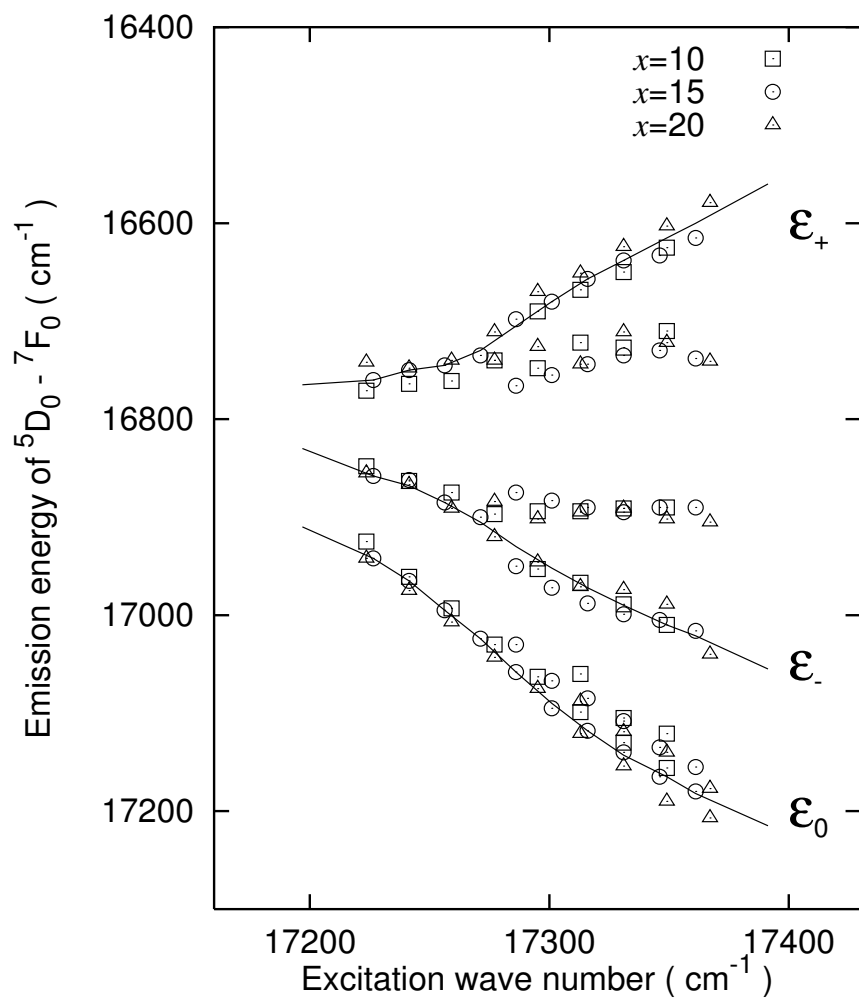
Figure 2.10: Dependence of peak energies of $^7F_1$ Stark components on excitation energy for $(100-x)B_2O_3 \cdot xNa_2O \cdot yEu_2O_3$ glasses with $x = 10$, 15, 20 and $y = 1.0$ and 0.1. The lines are shown for the glasses with $y = 0.1$.

tation energy in Figs. 2.9 and 2.10, respectively. The peak energies were evaluated from the predominant three lines in the $^7F_1$ emission spectra and were connected by three lines for each of the components. In particular, for Eu^{3+}, the energies were determined from the dominant three components (group α) which were observed for the low concentration of Eu^{3+}.

Fluorescence lifetimes of the $^5D_0$ level were measured for each excitation energy monitoring the $^5D_0 \rightarrow {}^7F_1$ emission positions obtained by deconvolution. The fluorescence decay curves for 85B$_2$O$_3$·15Na$_2$O·2.0SmO glass excited with 14641 cm^{-1} and 85B$_2$O$_3$·15Na$_2$O·1.0Eu$_2$O$_3$ glass excited with 17295 cm^{-1} are shown in Figs. 3.9(a) and (b), respectively. The lifetimes were calculated by the least squares method for each of decay curves. All the decay curves
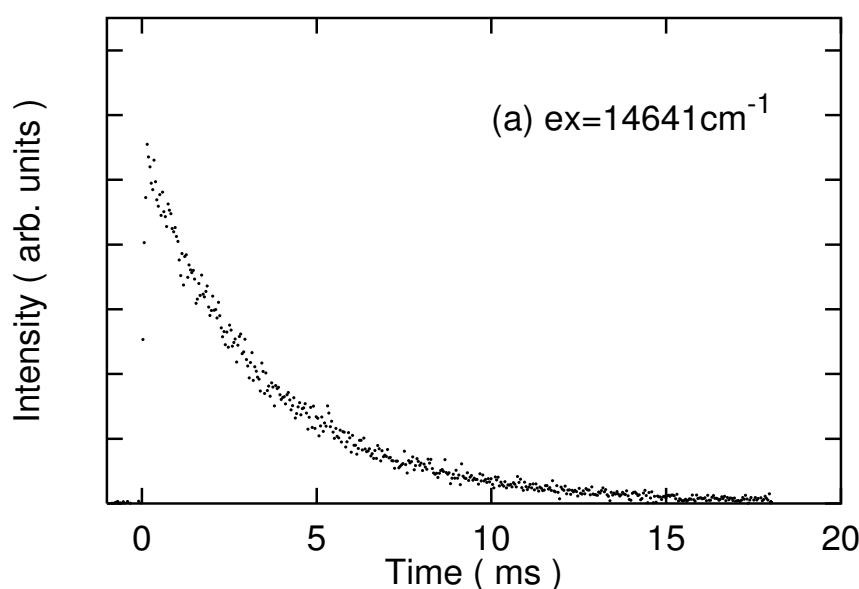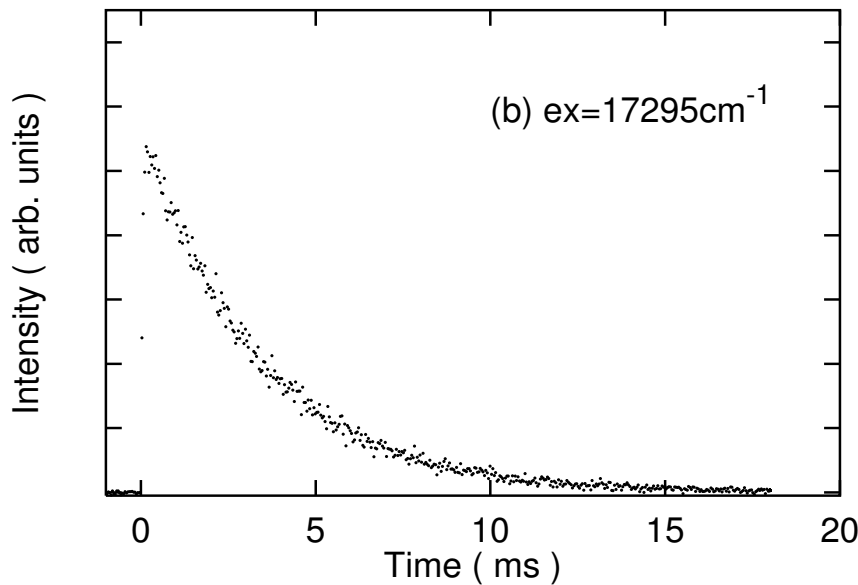

Figure 2.11: Time dependence spectra for (a) 85B$_2$O$_3$·15Na$_2$O·2.0SmO glass in 14641 cm^{-1} excitation energy and (b) 85B$_2$O$_3$·15Na$_2$O·1.0Eu$_2$O$_3$ glass in 17295 cm^{-1} excitation energy.

Figure 2.11: (*Continued.*)

were approximately represented by a single exponential over a 0~15 ms range. The excitation energy dependences of lifetime, as well as the distributions of lifetimes, are shown for $85B_2O_3 \cdot 15Na_2O \cdot xEu_2O_3$ glasses with $x = 0.1$ and 1.0 and $85B_2O_3 \cdot 15Na_2O \cdot xSmO$ glasses with $x = 0.2$ and 2.0 in Figs. 2.12 and 2.13, respectively. In these figures, the distribution of lifetime for each excitation energy is shown by a vertical bar.

Figures 2.12 and 2.13 show that, at higher excitation energy, the distribution of lifetime for the 2.0 mol% Sm^{2+} ion is much smaller than that for the 2.0 mol% Eu^{3+} ion. The difference in lifetime between the α and β groups brings about the extended distribution of lifetime for the 2.0 mol% Eu^{3+} ion. The α group is characterized by shorter lifetimes compared with the β group. In addition, it is found that for Eu^{3+}, the distribution range of lifetime becomes remarkably narrow as the concentration of Eu^{3+} varies from 2.0 mol%
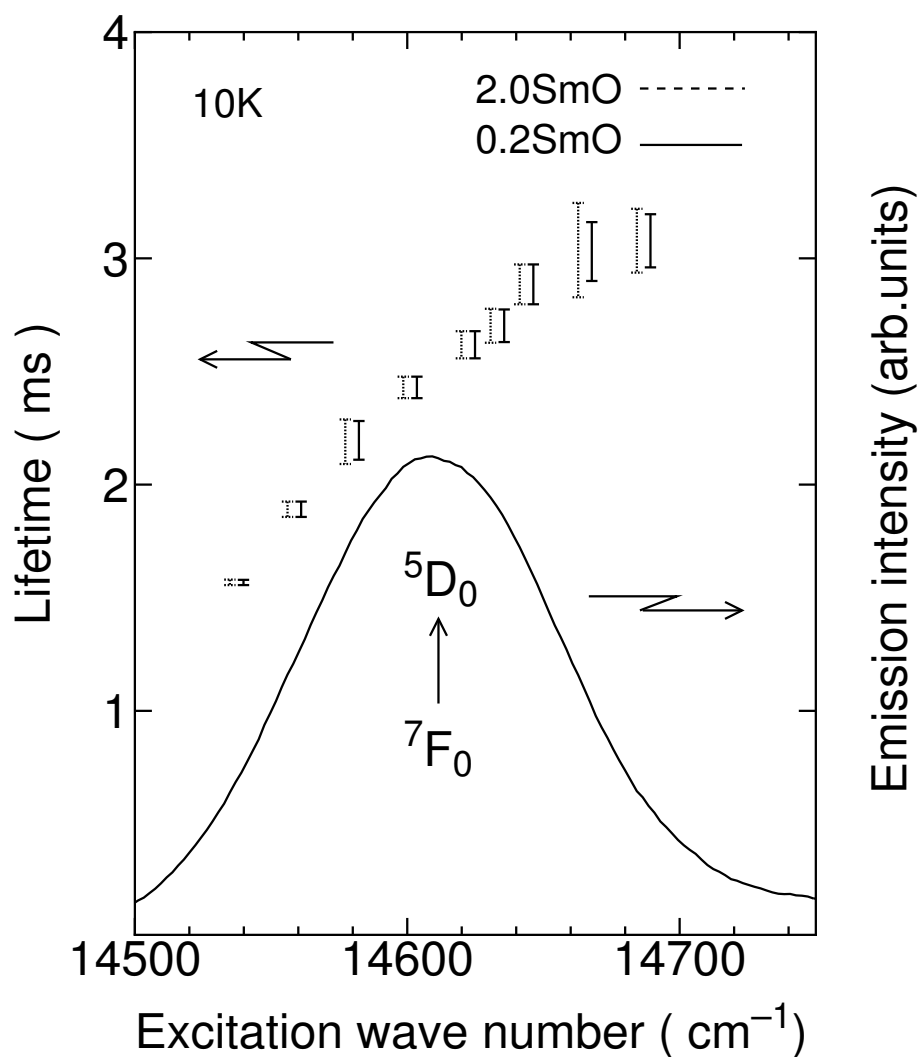
Figure 2.12: Fluorescence decay time of the $^5D_0$ state for $85B_2O_3 \cdot 15$ $Na_2O \cdot xSmO$ glasses with $x = 0.2$ and 2.0. The vertical bars indicate the distribution of lifetime. In the figure, the bars for the glass with $x = 0.2$ are shifted by 5 cm^{-1} to the high energy side for a clearer view.

Figure 2.13:   Fuorescence decay time of the $^5D_0$ state for $85B_2O_3 \cdot 15$ $Na_2O \cdot xEu_2O_3$ glasses with $x = 0.1$ and 1.0. The vertical bars indicate the distribution of lifetime. In the figure, the bars for the glass with $x = 0.1$ are shifted by 5 cm^{-1} to the high energy side for a clearer view.
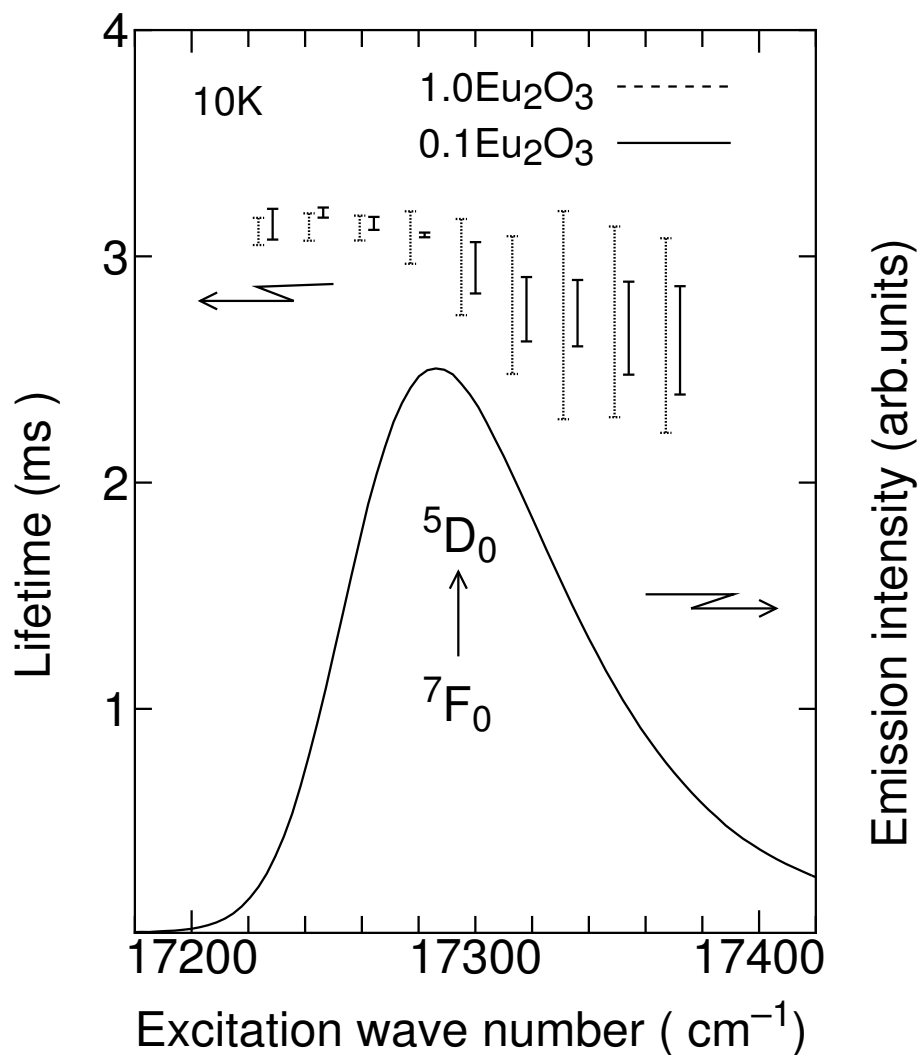
to 0.2 mol%. This behavior is clearly observed when the excitation energy is high. In contrast, for Sm^{2+}, the distribution range of lifetime does not change so significantly even though the concentration of Sm^{2+} varies from 2.0 mol% to 0.2 mol%.

2.2.4 Discussion

2.2.4.1 FLN Emission Spectra

The presence of more than three lines in the $^5D_0 - {}^7F_1$ spectra shown in Fig. 2.5 is can be explained in terms of either simultaneous excitation of some different kinds of sites under a single excitation and/or energy transfer between different sites occurring at some time before measurements are carried out. In Fig. 2.6, an additional peak at around 14600cm^{-1} shifts slightly when the excitation energy is varied, but its peak position nearly coincides with the peak energy of the $^7F_0 - {}^5D_0$ absorption line in Fig. 2.4(a). Therefore, it is considered that these peaks are due to the energy transfer in $^5D_0 - {}^7F_0$ transitions from the higher-energy sites to lower-energy sites. However, since the intensity ratio of the $^5D_0 - {}^7F_0$ line to the $^5D_0 - {}^7F_1$ line in FLN spectra is much weaker than that in the normal fluorescence spectrum, the energy transfer is sufficiently reduced. Also, as seen from Fig. 2.8, a large part of the $^5D_0 \to {}^7F_1$ emission line can be divided into only three lines, indicating that the effect of the energy transfer and/or accidental simultaneous excitation of different types of sites is less efficient. Figures 2.5 and 2.6 thus confirm that the inhomogeneous broadening due to the simultaneous excitation of some different kinds of sites and/or energy transfer is observed in site-selective spectra for both Sm^{2+} and Eu^{3+} ions, and these effects on $^7F_1$ spectra at the high-excitation energy are greater for Eu^{3+} ions than for Sm^{2+} ions. For Eu^{3+}, an additional peak due to the energy transfer which corresponds to the $^5D_0 - {}^7F_0$ transition may appear

in higher emission energy range than ϵ_0 component, but such a peak is hardly detected because of the wide energy gap between the $^7F_0$ and $^7F_1$ level and the weak intensity ratio of the $^5D_0 - {}^7F_0$ line to the $^5D_0 - {}^7F_1$ lines when compared with the case of Sm^{2+}, as shown in Figs. 2.3(a) and (b).

Figure 2.7 indicates that the decrease in the concentration of Eu^{3+} tends to suppress the energy transfer and/or give rise to the excitation of one type of sites. As a result, more detailed information concerning the Eu^{3+} ion site is obtained in high-excitation-energy range, although the cause of the presence of more than three components in the site-selective spectra still remains unclear. On the other hand, from the concentration dependence of FLN emission spectra shown in Fig. 2.8, it is inferred that since the energy transfer and/or the simultaneous excitation of some different kinds of sites do not take place efficiently on FLN measurements for the 2.0 mol% Sm^{2+} ion, a drastic change of the spectral line is not observed even when the concentration of Sm^{2+} decreases. The concentration dependence of rare-earth ions in FLN spectra is discussed in detail together with the results obtained by lifetime measurements in Section 2.2.4.2.

For Sm^{2+}, ϵ_0 is sensitive to excitation energy, whereas ϵ_+ and ϵ_- are almost independent of the excitation energy, as shown in Fig. 2.9. For Eu^{3+}, on the other hand, ϵ_0 and ϵ_- shift to lower energy side, while ϵ_+ shifts toward the opposite direction, when the excitation energy is increased as seen from Fig. 2.10. Similar behaviors of $^7F_1$ splitting were reported by Brecher and Riseberg for Eu^{3+} -doped silicate and fluoroberyllate glasses [2,3]. The excitation energy dependence of the $^7F_1$ state for Sm^{2+} in borate glasses resembles that for Eu^{3+} in a silicate glass, whereas Eu^{3+} in borate glasses manifest a tendency similar to that for Eu^{3+} in a fluoroberyllate glass. These results thus suggest that the local environment around Sm^{2+} is different than that around Eu^{3+} in borate glasses with sodium contents of $10 - 20$ mol%. Brecher and Riseberg [2, 3]

performed crystal-field analysis for the different types of excitation energy dependence of the $^7F_1$ state using a point-charge model and assuming C_{2v} site symmetry, and proposed two structural models. In their structural models, the difference in excitation energy-dependent shifts of $^7F_1$ components can be ascribed to the difference in symmetry of the wave function which expresses each of the components.

The difference in excitation energy dependence of peak positions of the $^7F_1$ components can be related to the difference in glass-formating ability between Sm^{2+} - and Eu^{3+} -containing borate glasses. It is impossible to incorporate even a small amount of Eu^{3+} ions into B$_2$O$_3$ glass free from Na$_2$O because of the phase separation [24]. On the contrary, from a point of view of glass formation, divalent rare-earth ions are believed to have chemical properties similar to alkaline earth ions such as Ca^{2+} and Sr^{2+} that give rise to extended glass-forming regions with B$_2$O$_3$ [25, 26]. In fact, according to Winterer *et al.* [26], it is possible to introduce 4.0 mol% EuO in pure B$_2$O$_3$ without immscibility in contrast to introducing Eu$_2$O$_3$. In other words, divalent rare-earth and alkaline earth ions can be dispersed in the B$_2$O$_3$ glass network, but trivalent rare-earth ions have a tendency to aggregate when the network modifying cations such as alkali and alkaline earth ions, which assist the glass formation, are not present. Consequently, it is considered that, in borate glasses, the stable local structure around divalent rare-earth ions is significantly different from that around trivalent rare-earth ions.

The electronic levels of rare-earth ions are considered to reflect the characteristics of bonds relevant to the rare-earth ion, the coordinating ions and the ions beyond the first coordination sphere. In sodium borate glasses, with increasing Na$_2$O content, the number of three-coordinated boron decreases and that of four-coordinated boron increases up to about 33 mol% Na$_2$O content, as demonstrated from ^{11}B NMR measurements [27]. Besides, the nonbridging

oxygens are absent in the glass-network when the concentration of Na_2O is below 25 mol%. In other words, the flexibility of glass-network structure does not change so significantly even though the glass composition is varied for the present glass compositions. As found from Figs. 2.9 and 2.10, the peak positions of $^7F_1$ manifolds vary little with glass composition, indicating that the local structure around Sm^{2+} and Eu^{3+} ions does not change even if the glass composition varies.

2.2.4.2   Lifetime Measurement

It is well known that for Eu^{3+} in most solids, the radiative quantum efficiency of $^5D_0$ state is almost unity because of the wide energy gap between $^5D_0$ and the next-lower $^7F_6$ state as well as the weak interaction between $4f$ electrons and surrounding ions. For Sm^{2+}, the lifetime was almost independent of temperature from 10 to 80 K, indicating that the radiative relaxation is dominant. Furthermore, for both ions, the excitation wave number dependence of the emission intensity in the FLN measurements manifests a profile similar to the inhomogeneously broadened excitation spectrum when the laser power is constant. Thus the excitation energy dependence of lifetime, as well as the lifetime distribution indicated by a vertical bar in Figs. 2.12 and 2.13, presumably reflects the site variation of the radiative transition probability, which is strongly affected by the local structure around the rare-earth ion. Another possibility for the large distribution of lifetime could be the energy transfer which is closely associated with ion-ion interactions such as dipole-dipole, dipole-quadrupole, quadrupole-quadrupole interaction, and so forth. Therefore, a more extended distribution of lifetime at higher excitation energy for the 2.0 mol% Eu^{3+} ion is consistent with the simultaneous excitation of different kinds of sites and/or the energy transfer mentioned above. On the other hand, the results for the lifetime distributions as well as the FLN spectra

for the Sm^{2+} ion reflect the fact that Sm^{2+} ions are distributed rather homogeneously as network-modifying cations in the glass-network; in such a situation, the effects of ion-ion interaction and occupation of different kinds of sites become less efficient. As for Eu^{2+} ions in borate glasses, such a concept has been already deduced from the experiments of the ^{151}Eu Mössbauer effect or fluorescence properties [26, 28]. Thus it is speculated that the difference in valence and ionic radius of rare-earth ions determines whether the rare-earth ion is distributed homogeneously or inhomogeneously in sodium borate glasses. The supposition is consistent with the glass-forming ability of the borate system containing rare-earth ions as was discussed in the last section.

2.2.5   Conclusion

For Sm^{2+}- and Eu^{3+} -doped borate glasses with Na$_2$O contents from 10 to 20 mol%, site-dependent information about these rare-earth ions was obtained using FLN method. The result indicates that the optical properties of Sm^{2+} entirely differ from those of Eu^{3+}. When the excitation energy is high, the influence of the different types of sites and/or the interaction among rare-earth ions on the optical properties is more remarkable for the Eu^{3+} ion than for the Sm^{2+} ion. For Eu^{3+}, the distribution of lifetime changes clearly when the concentration of Eu^{3+} varies from 2.0 to 0.2 mol% although for Sm^{2+}, it remains nearly constant. The peak energies of $^{7}F_1$ components as a function of the difference in energy between $^{5}D_0$ and $^{7}F_0$ levels propose that the stable environments around divalent and trivalent rare-earth ions are significantly different from each other in the present sodium borate glasses. It is concluded that the valence and ionic radius of rare-earth ions have a considerable effect on ion's distribution state and local structure in sodium borate glasses with low sodium contents.

References

[1] J. Hegarty, R. Brundage, and W. M. Yen, Appl. Opt. **19**, 1889 (1980).

[2] C. Brecher and L. A. Riseberg, Phys. Rev. B **13**, 81 (1976).

[3] C. Brecher and L. A. Riseberg, Phys. Rev. B **21**, 2607 (1980).

[4] C. Brecher, L. A. Riseberg, and M. J. Weber, Phys. Rev. B **18**, 5799 (1978).

[5] S. A. Brawer and M. J. Weber, Phys. Rev. Lett. **45**, 460 (1980).

[6] S. Hüfner, in *Optical spectra of Transparent Rare Earth Compound* (New York, Academic, 1978), p. 14.

[7] M. J. Weber, J. Hegarty, and D. H. Blackburn, in *Borate Glasses: Structua Properties and Applications* (Plenum Press, New York, 1978), p. 215.

[8] G. Boulon, M. Bouderbala, and J. Seriot, J. Less-Common Met. **112**, 41 (1985).

[9] T. F. Belliveau and D. J. Simkin, J. Non-Cryst. Solids **110**, 127 (1989).

[10] G. Nishimura and T. Kushida, J. Phys. Soc. Jpn. **60**, 683 (1991).

[11] J. L. Adam, V. Poncon, J. Lucas, and G. Boulon, J. Non-Cryst. Solids **91**, 191 (1987).

[12] K. Soga, M. Uo, H. Inoue, and A. M. nad S. Inoue, J. Am. Ceram. Soc. **78**, 129 (1995).

[13] M. Tanaka and T. Kushida, Phys. Rev. B **49**, 5192 (1994).

[14] R. M. Macfarlane and R. M. Shelby, Opt. Commun. **45**, 46 (1983).

[15] Th. Schmidt, R. M. Macfarlane, and S. Völker, Phys. Rev. B **50**, 15707 (1994).

[16] T. Suemoto, M. Namiki, and K. Koyama, Opt. Commun. **115**, 475 (1995).

[17] D. M. Boey, R. M. Macfarlane, Y. Sun, and R. S. Meltzer, Phys. Rev. B **54**, 6263 (1996).

[18] K. Hirao, S. Todoroki, D. H. Cho, and N. Soga, Opt. Lett. **18**, 1586 (1993).

[19] D. H. Cho, K. Hirao, K. Fujita, and N. Soga, J. Am. Ceram. Soc. **79**, 327 (1996).

[20] J. R. Morgan, E. P. Chock, W. D. Hopewell, M. A. El-sayed, and R. Orbach, J. Phys. Chem. **85**, 747 (1981).

[21] K. Hirao, S. Todoroki, and N. Soga, J. Lumin. **55**, 217 (1993).

[22] X. Gang and R. C. Powell, J. Appl. Phys. **57**, 1299 (1985).

[23] A. Lempicki, H. Samelson, and C. Brecher, J. Mol. Spectrosc. **27**, 375 (1968).

[24] E. M. Levin, Phys. Chem. Glasses **7**, 90 (1966).

[25] M. W. Shafer and J. C. Suits, J. Am. Ceram. Soc. **49**, 261 (1966).

[26] M. Winterer, E. Morsen, B. D. Mosel, and W. Muller-Warmuth, J. Phys. C **20**, 5389 (1987).

[27] P. J. Bray and J. G. O. Keefe, Phys. Chem. Glasses **44**, 37 (1963).

[28] K. Tanaka, T. Ohyagi, K. Hirao, and N. Soga, Bull. Chem. Soc. Jpn. **66**, 1121 (1993).

Chapter 3

Low-temperature optical dephasing of rare-earth ions in glasses
— A study by persistent spectral hole burning

3.1   Optical dephasing and homogeneous linewidth

Electronic transitions between $4f^n$ states of rare-earth ions in solids arise predominantly from pure electronic transitions, i.e., zero phonon lines, which correspond to the electronic transition without creating any phonon. At $T = 0$ K, the zero-phonon linewidth, i.e., the homogeneous linewidth, $\Gamma_h(0)$, is given by

$$\Gamma_h(0) = \frac{1}{2\pi c T_1(0)} \quad (\text{in cm}^{-1}), \tag{3.1}$$

where $T_1(0)$ is the lifetime of the excited electronic state.

At $T > 0$ K, the homogeneous linewidth, Γ_h, broadens due to optical dephasing processes caused by phonons excited by the lattice vibrations. The optical dephasing takes place as a result of the quasi-elastic scattering of a phonon at impurity, i.e., the electron-phonon interaction, and the phonon scattering leads to an abrupt change in phase of wave function in the excited electronic state. In other words, the electron is left in the excited electronic level, l, but the time-dependent part of its wave function, $\exp(iE_l t/\hbar)$, is changed to $\exp[i(E_l t/\hbar) + i\delta]$, δ being a random phase shift. For an ensemble of impurities, this dephasing means that the coherence time of excited impurities is shortened, and thus, the corresponding linewidth, Γ_h, becomes larger compared with

the value determined by the lifetime of the excited state. Zero-point vibration causes no optical dephasing. The density of thermal phonons increases with temperature, thereby giving rise to the temperature broadening of Γ_h. Thus, it is reasonable to introduce two characteristic periods, the energy relaxation time, T_1, and the pure dephasing time, T_2^*. Relaxation in energy results in phase memory loss as well, and the overall coherence time, T_2, of the excited electronic state, which governs the Γ_h, can be written as follows:

$$\Gamma_h(T) = \frac{1}{\pi c T_2} = \frac{1}{\pi c}\left(\frac{1}{2T_1} + \frac{1}{T_2^*}\right) \quad (\text{in cm}^{-1}). \tag{3.2}$$

When nonradiative decay processes are present, $1/T_1 = 1/T_{\text{rad}} + 1/T_{\text{non}}$, where T_{rad} and T_{non} are the radiative and nonradiative decays, respectively. Usually the temperature dependence of T_{rad} is neglected, while T_{non} and T_2^* depend strongly on temperature. When the contribution of T_{non} to Γ_h is negligibly small, T_2^* remains as the main source of the temperature dependence of Γ_h. Then the optical dephasing processes are reflected in the temperature dependence of Γ_h

Let's express the interaction of the rare-earth ion with the host lattice in terms of a power series of the dynamical strain, ϵ, due to the lattice vibration as follows:

$$V = V^{(0)} + V^{(1)}\epsilon + V^{(2)}\epsilon^2 + \cdots, \tag{3.3}$$

where $V^{(n)}$ is the nth-order expansion coefficient of V with respect to ϵ. $V^{(0)}$ represents the static crystal-field potential, and it does not contribute to the phonon-induced optical dephasing directly. The one-phonon absorption and emission (direct process) arise from first-order perturbation due to the second term, while the Raman process occurs by the $V^{(1)}\epsilon$ term in second order as

well as by the $V^{(2)}\epsilon^2$ term in first order. The homogeneous linewidth, $\Gamma_{\rm h}$, originating from the Raman process is given by

$$\Gamma_{\rm h} = C \int_0^\infty | <H> |^4 \frac{\rho^2(\omega) e^{\hbar\omega/kT}}{(e^{\hbar\omega/kT} - 1)^2} d\omega, \tag{3.4}$$

where C is a constant, H is the electron-phonon interaction Hamiltonian, $\rho(\omega)$ is the vibrational density of states, and k is the Boltzmann constant. In pure crystals, it is reasonable to use the Debye approximation, $\rho(\omega) \propto \omega^2$, for the density of states and the long wavelength approximation, $<H>^2 \propto \omega$, for the interaction over the entire acoustic phonon spectrum. In this case, one finds

$$\Gamma_{\rm h} \propto T^7 \int_0^{T_D/T} \frac{x^6 e^x}{(e^x - 1)^2} dx, \tag{3.5}$$

where T_D is the Debye temperature. According to Eq. (3.5), the value of $\Gamma_{\rm h}$ varies as T^2 for $T > 0.5T_D$, while the temperature dependence obeys T^7 -law at low temperatures ($\sim$10K). This theory is fairly consistent with the temperature dependence of $\Gamma_{\rm h}$ for crystals such as $Y_2O_3 : Eu^{3+}$ [1]. However, in glasses, the vibrational distribution is more complicated than the one described by Debye's theory, and involves an additional low-frequency vibration. Besides, if the participation of the nonacoustic low-frequency phonons is dominant, the long-wavelength approximation assumed in the above discussion is not appropriate. It will be reasonable that the interaction of the rare-earth ion with such phonons is expressed in terms of a power series of the amplitude of the lattice vibration instead of the dynamical strain in Eq. (3.3). Then $<H>^2 \propto \omega^{-1}$ is more appropriate [2,3].

On the other hand, some current theories of optical dephasing [4–7] predict that the temperature dependence of $\Gamma_{\rm h}$ is determined by the energy dependence of the density of states of two-level system (TLS) in glasses. This is because the coupling between the optical transition and the TLS is modulated by absorption and emission of phonons, and leads to a dependence of T^α with $\alpha = 1 - 2$.
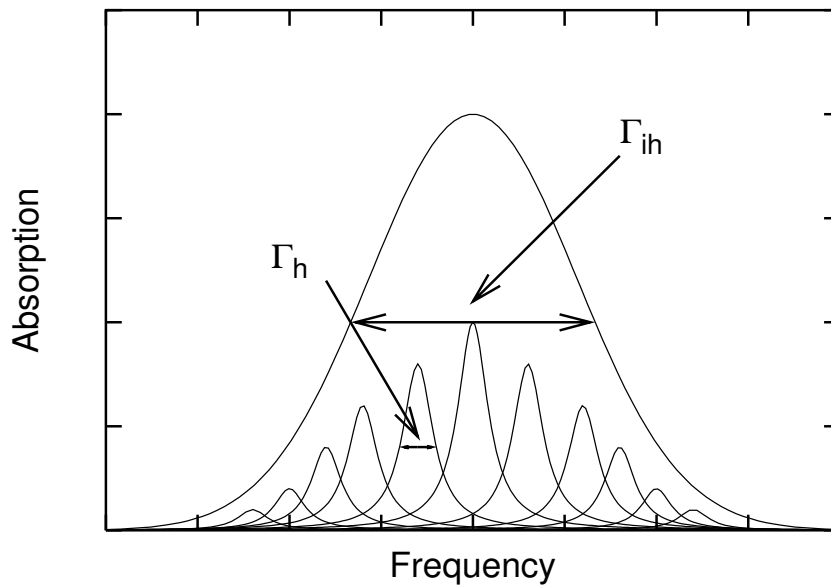
Figure 3.1: Priciple of homogeneous and inhomogeneous broadening in glasses.

In order to fully understand the temperature dependence of Γ_h in glasses, it is nessesary to measure Γ_h in a wide temperature range. However, the optical transitions of rare-earth ions in glasses exhibit the large inhomogeneous linewidth, Γ_{ih}, because of their site-to-site variations as described in Chapter 2. An example of a continuous distribution of Γ_h which overlaps to form Γ_{ih} is shown in Fig. 3.1. Spectroscopic techniques such as fluorescence line narrowing, spectral hole burning and photon echos have been used to eliminate the influence of Γ_{ih} and to get information on Γ_h. In this chapter, the temperature dependence of Γ_h for rare-earth -doped glasses is measured by means of spectral hole burning. Hence, the mechanisms of spectral hole burning in rare-earth -doped glasses studied so far are described in the following section.

3.2 Spectral hole burning of rare-earth ions in inorganic glasses

Spectral hole burning occurs when the transition energy of guest ion embedded in a solid changes after absorption of monochromatic light. By irradiating the inhomogeneously broadened spectral band with a narrow band laser of frequency, ω_L, those ions which are resonant with the laser may undergo a phototransformation such that the product absorbs at a different frequency. This creates a hole or dip in the original absorption band at ω_L as shown in Fig. 3.2. The photoproduct can either be stable at low temperatures and a permanent hole is formed, or it can be a metastable state that acts as a population storage level, by which a transient hole is created. The hole is subsequently
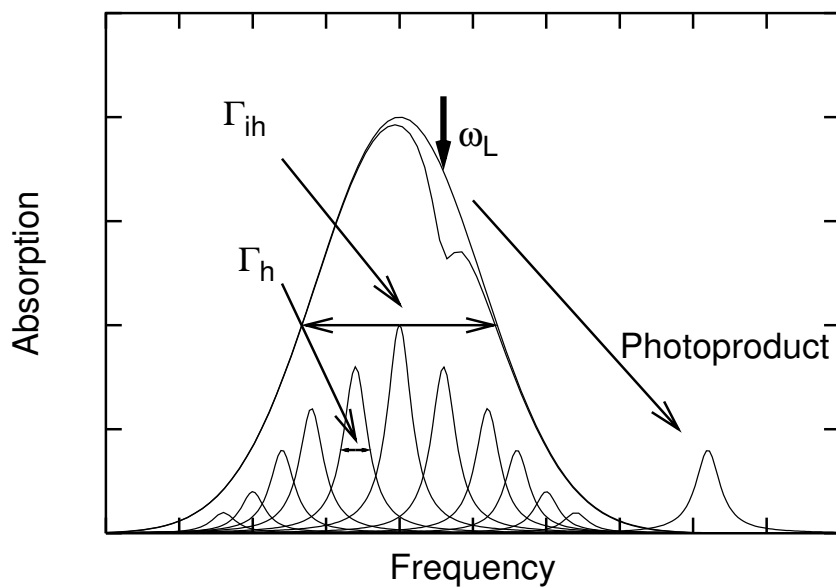

Figure 3.2: Laser-induced hole burnd at frequency, ω_L. Here, the photopruduct is assumed to be redistributed outside the inhomogeneous band.

probed in a second step by means of a tunable laser, which scanned over the frequency region of the hole. The intensity of the latter should be low enough to avoid further burning of the absorption band. The hole represents, after minor correction, a negative replica of the homogeneous transition, and the hole linewidth at a small burning intensity yields the homogeneous linewidth, Γ_{h}. Thus, with spectral hole burning, optical resolutions can be obtained which are much higher than those reached with conventional techniques. In this way, for example, it is possible to study the influence of host dynamics on impurity ions in solids at extremely low temperatures.

Because the optical transition energy depends on the environment in a complicated way, the laser is not selecting ions in a specific environment, but a set of ions in different environment, all absorbing at the same frequency, ω_L. Furthermore, since the correlation between transition energy and environmental parameters is, in general, different for the photoproduct and the original ion, it is expected that the photoproduct band or "anti-hole" will be broader than the hole.

3.2.1 Mechanisms of spectral hole burning

Three mechanisms are known to be responsible for spectral hole burning of rare-earth ions in inorganic glasses; non-photochemical hole burning (NPHB), transient hole burning (THB) and photoionization hole burning (PHB).

3.2.1.1 Non-photochemical hole burning (NPHB)

This mechanism is characteristic of amorphous systems. The first examples of inorganic impurity ions to show NPHB are Pr^{3+} and Nd^{3+} ions in silicate glasses as shown in Table 3.1 [8,9]. A detailed hole-burning mechanism is not understood, but the reversibility and burning characteristics suggest that the hole burning occurs by a slight rearrangement of the local structure of the glass in the vicinity of the optical center. Glasses are thermodynamically metastable solids, and have non-equilibrium states. In such disordered solids, it is thought that rare-earth ions are coupled to a two-level system (TLS) of the glass at very low temperatures, and after excitation with a narrow band laser, tunneling takes place in the electronically excited state which is followed by relaxation to a different ground state configuration as shown in Fig. 3.3. As a result, the optical transition is shifted, and the non-photochemical hole is burned in the absorption band. The hole is permanent at temperatures that are much lower

Table 3.1: Non-photochemical hole burning observed in rare-earth -doped inorganic glasses [8,9].

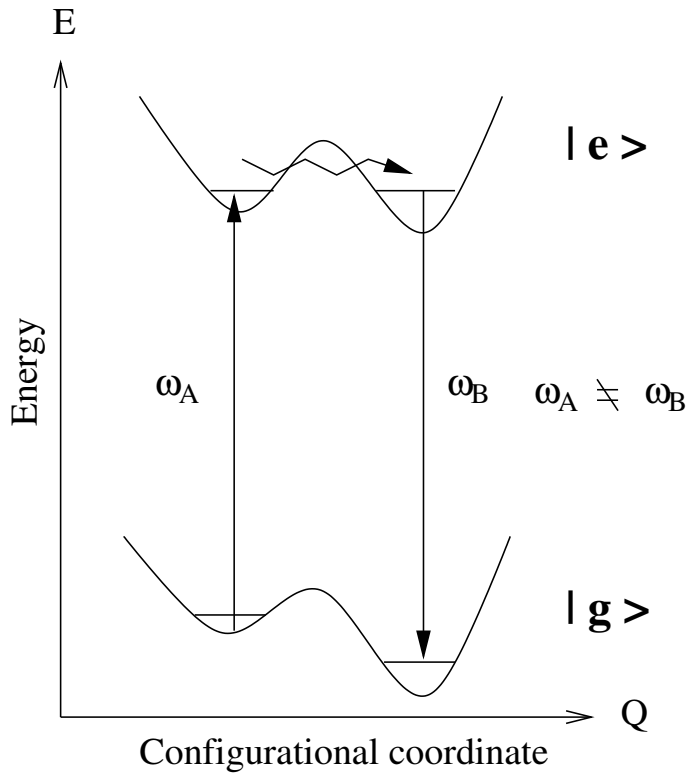| Material	burning wavelength (Å)	transition
Silicate glass: Pr^{3+}	6060	$^3H_4 \rightarrow ^1D_2$
Silicate glass: Nd^{3+}	5950	$^4I_{9/2} \rightarrow ^4G_{5/2}$

Figure 3.3: Schematic diagram of non-photochemical hole burning mechanism. |e> and |g> represent potential energy curves of a two-level system (TLS) of a glass interacting with the ground and electronically excited states of a guest ion.

than that corresponding to the ground state barrier. TLS was first proposed to explain anomalous thermal properties in glasses at low temperatures and is presumed to involve two nearly equi-energetic configurations of groups of atoms in the glass between which transition takes place by phonon-assisted tunneling [10, 11].

3.2.1.2 Transient hole burning (THB)

THB is a mechanism by which population is transfered from the ground state to a metastable state such as hyperfine levels. This mechanism is observed for Eu^{3+} -doped silicate glass [12], in which the large quadrupole splitting of $^7F_0$ ground state allows optical pumping among these levels as shown in Fig. 3.4. The hole can be burned much more efficiently, but it persisted for only a few seconds in the dark at very low temperatures. Also, anti-holes are
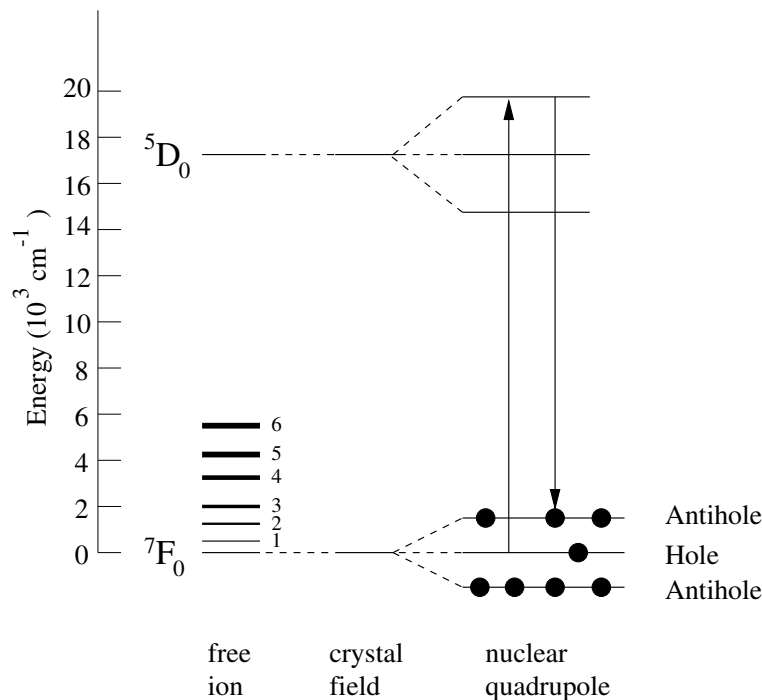

Figure 3.4: Schematic diagram of the optical pumping mechanism of the quadrupole split levels of $I = 5/2$ europium nucleus. The energy level diagram shows the redistribution of population in the nuclear quadrupole levels of Eu^{3+} by an optical pumping, leading to a hole at laser frequency and anti-holes at frequencies consistent with quadrupole splittings [12].

observed at frequencies consistent with Eu quadrupole splittings.

3.2.1.3   Photoionization hole burning (PHB)

PHB is observed for Sm^{2+} -doped oxide and fluoride glasses [13–15]. It is believed that photoionization of $Sm^{2+} \rightarrow Sm^{3+} + e^-$ takes place by irradiation of a narrow band laser, and the released electron is trapped at an unknown site. The PHB in these glasses is not caused by a two-photon process observed by Winnacker *et al.* [16] for $BaClF : Sm^{2+}$ crystals, but by an one-photon process [15]. This is illustrated in Fig. 3.5. A remarkable and unique feature is that the hole is stable at room temperature.
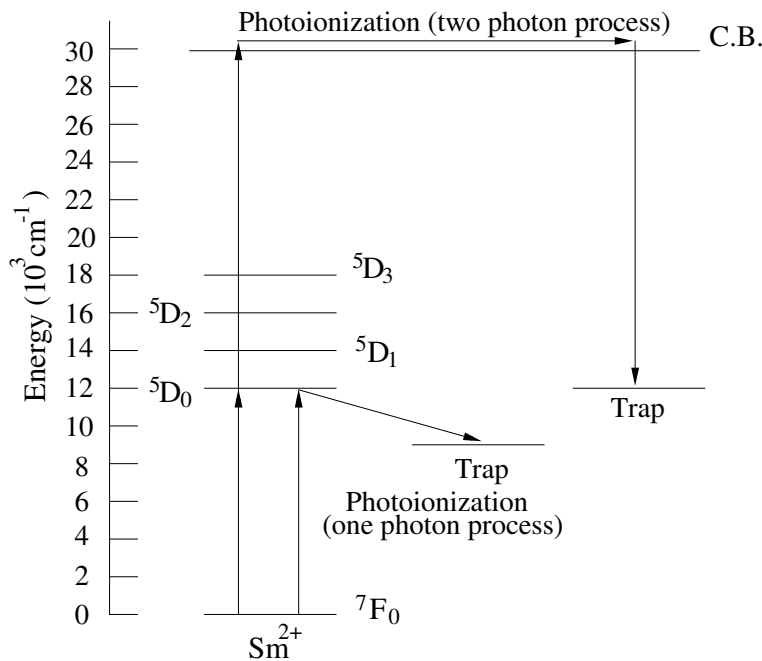

Figure 3.5: Energy-level diagram of Sm^{2+} showing the mechanism for photoionization hole burning.

3.3 Persistent spectral hole burning of Eu^{3+} ions in silicate glasses

3.3.1 Introduction

As described in Chapter 2, trivalent rare-earth ions in glasses exhibit a homogeneous linewidth much narrower than inhomogeneous linewidth because of their weak coupling to the surrounding lattice, especially at low temperatures. Consequently, a site-selective excitation provides the information relevant to each of optical centers in glasses which is hindered by inhomogeneous broadening. Spectral hole burning and fluorescence line narrowing (FLN) have been utilized for such a purpose. The FLN technique has been extensively employed to measure the homogeneous linewidth (Γ_{h}) of optical transitions [17–20] and to evaluate a distribution of rare-earth ion sites as a function of excitation energy [21, 22]. For the measurement of Γ_{h}, however, the measurement temperatures in FLN reported were usually limited above about 10 K because Γ_{h} becomes less than the spectral resolution of a spectrometer at lower temperatures. On the other hand, spectral hole burning, whose resolution is restricted by the spectral resolution of laser linewidth, is a powerful tool as a high resolution spectroscopy and is useful for the measurements of Γ_{h} in inorganic solids. In particular, the value of Γ_{h} is readily obtained for solids which show persistent spectral hole burning (PSHB). The PSHB has been extensively examined for various inorganic materials doped with rare-earth ions, ranging from nearly perfect crystals to disordered materials, from a viewpoint of the application to frequency and time domain optical memories [23] as well as the basic research of the optical dephasing process [8, 9].

It is known that Γ_{h} of rare-earth ions in glasses exhibits an anomalous behavior in both their magnitude and temperature dependence when compared

with crystalline counterparts. This anomaly is inevitably observed in Eu^{3+} - doped glasses. It has been found that Γ_h of the $^5D_0 - {}^7F_0$ transition of Eu^{3+} in various glasses has a nearly quadratic temperature dependence at a wide temperature range above about 10 K [17–19, 24], while most crystals doped with Eu^{3+} show T^7 -dependence of Γ_h. On the other hand, a T-linear dependence of Γ_h has been observed for the same transition of Eu^{3+} in silicate glass at 0.4 to 4.2 K by means of transient hole burning spectroscopy [25, 26] and at 1.6 to 7 K by means of accumulated photon echoes [24]. These phenomena were commonly connected with the vibrational properties characteristic of glass, such as two-level system (TLS). For instance, Γ_h for Eu^{3+} -doped silicate glass was reported to follow the same T -linear dependence as the contribution of the TLS to specific heat measured on the same sample at 0.4 to 4.2 K [25, 26]. The result coincides with theoretical models of optical dephasing in which the same T -dependence is predicted for both Γ_h and the contribution of the TLS to the specific heat in a given sample. However, up to now, few data are accumulated with respect to the temperature dependence of Γ_h in Eu^{3+} -doped glasses between 4.2 and 10 K, and therefore the optical dephasing mechanisms are not fully understood over a wide temperature range. One reason for this fact is that PSHB is usually not observed in the Eu^{3+} -doped glasses except Al_2O_3-SiO_2 system reported by Mao *et al.* recently [27].

In spite of a long history of research in this field, some unresolved problems exist concerning the condition for the formation of persistent holes in glasses. PSHB has been observed in Sm^{2+} -doped oxide and fluoride glasses at room temperature [13–15], while in Pr^{3+} -doped silicate glasses it takes place at 1.6 to 20 K [12]. For Eu^{3+}, two types of spectral hole have been reported at different temperature ranges. Schmidt *et al.* [25] carried out time-resolved spectral hole burning in Eu^{3+} -doped silicate glass at 0.4 to 4.2 K, and revealed that transient holes arose from an optical pumping among ground-

state nuclear quadrupole levels, and therefore hole spectra were accompanied with symmetrically placed antihole pairs. In addition, persistent holes were not burned even at a high laser fluency. In contrast, as mentioned above, Mao *et al.* [27] reported that PSHB was observed at the liquid nitrogen temperature in 74.8SiO$_2$·22.0Al$_2$O$_3$·3.2Eu$_2$O$_3$ glass prepared under an inert He atmosphere. These results for the Eu^{3+} -doped glasses suggest that the formation of persistent holes is feasible by the change of glass composition or melting condition. Also, it is expected that the inhomogeneous linewidth of the $^5D_0 - {}^7F_0$ transition of Eu^{3+} in glasses depends on glass composition because it reflects the site-to-site variation of Eu^{3+}. The inhomogeneous linewidth is particularly important for the application of PSHB materials to a frequency domain optical memory. In the present investigation, an attempt was made to control not only the character of holes but also the inhomogeneous linewidth of $^5D_0 - {}^7F_0$ transition in Eu^{3+} -doped silicate glasses containing Al$_2$O$_3$. In particular, attention is paid to the role of Al^{3+} in persistent hole burning. Also, the temperature dependence of Γ_h for the $^5D_0 - {}^7F_0$ transition of Eu^{3+} in the aluminosilicate glass is discussed.

3.3.2 Experimental procedure

Glasses with compositions of $(75 - x)$SiO$_2 \cdot x$AlO$_{3/2}$·25NaO$_{1/2}$·1.0EuO$_{3/2}$($x = 0, 10, 15, 20, 25, 35$) in cation ratio were prepared from reagent-grade Eu$_2$O$_3$, Na$_2$CO$_3$, Al$_2$O$_3$ and SiO$_2$ as starting materials. The raw materials were mixed thoroughly in a porcelain mortar and melted in a platinum crucible at 1600 °C for 2 h. Then the melt was cooled to room temperature. In order to obtain more homogeneous glass, the glass thus obtained was pulverized and remelted at 1600 °C for 2 h. The melt was cooled slowly to room temperature. The resultant glass was cut and polished into a rectangular parallelepiped shape of 10×5×5 mm^3.

Fluorescence and excitation spectra were obtained at room temperature or 12 K using a fluorescence spectrophotometer with a Xe lamp as a light source (Hitachi 850). Optical absorption spectra were measured at room temperature using a spectrophotometer with a Xe lamp as a light source (Hitachi 330). Luminescence decay curve was measured at 12 K using a dye laser composed of a mixture of rhodamin6G and rhodaminB (Spectra Physics, PDL-3), which was pumped by a frequency doubled Nd:YAG laser (Spectra Physics, GCR-11). The output pulse had a duration of 6 ns and a typical linewidth of 0.07 cm^{-1} at a repetition rate of 10 Hz. The excitation was performed at the wavelength of 580 nm. The output of $^5D_0 - {}^7F_2$ emission at 612 nm was recorded using a monochromator (Spex 270M, resolution $\sim$0.1 nm), a storage oscilloscope (Hewlett Packard 54522A, 500 MHz bandwidth) and a photomultiplier (Hamamatsu Photonics R955). The luminescence lifetime was determined by a least-square fitting with an exponential function. For the measurements at 12 K, the glass sample was cooled using a closed cycle helium gas refrigerator (Iwatani Plantech, Model CRT-006-2000).

Persistent spectral hole burning was measured using a setup illustrated in Fig. 3.6. A single frequency ring dye laser (Coherent CR899-21, a frequency jitter width of $\sim$1 MHz) was used to burn and subsequently probe the hole. The dye laser was operated with rhodamine 6G for the excitation of Eu^{3+}. A typical laser intensity on the sample under burning was $\sim$100 W/cm^2. The hole burned was detected by measuring a fluorescence excitation spectrum with a beam the power of which was attenuated by a factor of 100. Luminescence ray from the sample in the direction perpendicular to the excitation beam was collected by a lens to a photomultiplier (Hamamatsu Photonics R928). A color filter was used to intercept the scattered laser radiation but transmit the luminescence of wavelengths longer than 600 nm. A digital oscilloscope (Tektronics 11403A) was used for the storage and averaging of signal. Hole spectrum was
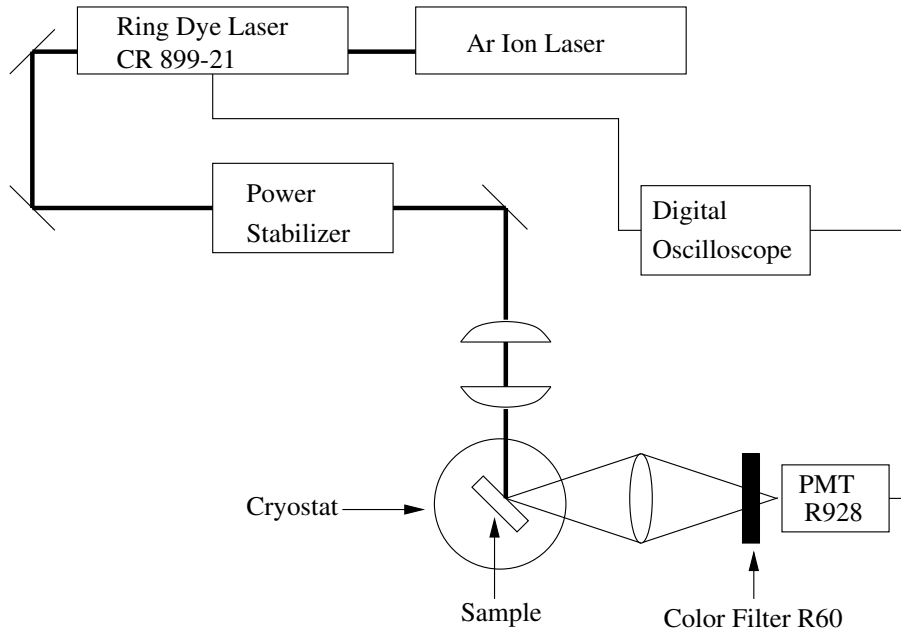
Figure 3.6: Schematic illustration of the equipment for hole-burning measurements.

fitted to a single Lorentzian function by a least-squares method. The sample was placed in a He flow cryostat (Oxford Instruments CF-1204), and the temperature was kept constant by a temperature-controller (Oxford Instruments CF-1240).

3.3.3 Results

Figure 3.7(a) shows normal fluorescence spectra of Eu^{3+} in $75SiO_2 \cdot 25NaO_{1/2} \cdot 1.0EuO_{3/2}$ and $50SiO_2 \cdot 25AlO_{3/2} \cdot 25NaO_{1/2} \cdot 1.0EuO_{3/2}$ glasses at 12 K. The excitation is carried out at 394 nm which corresponds to the $^5L_6 \leftarrow ^7F_0$ transition of Eu^{3+}. These fluorescence spectra manifest some bands which originate from transitions between the $^5D_0$ level and various ^7F_n levels (see energy level diagram of Fig. 3.4). Figure 3.7(b) shows excitation spectra of Eu^{3+} in
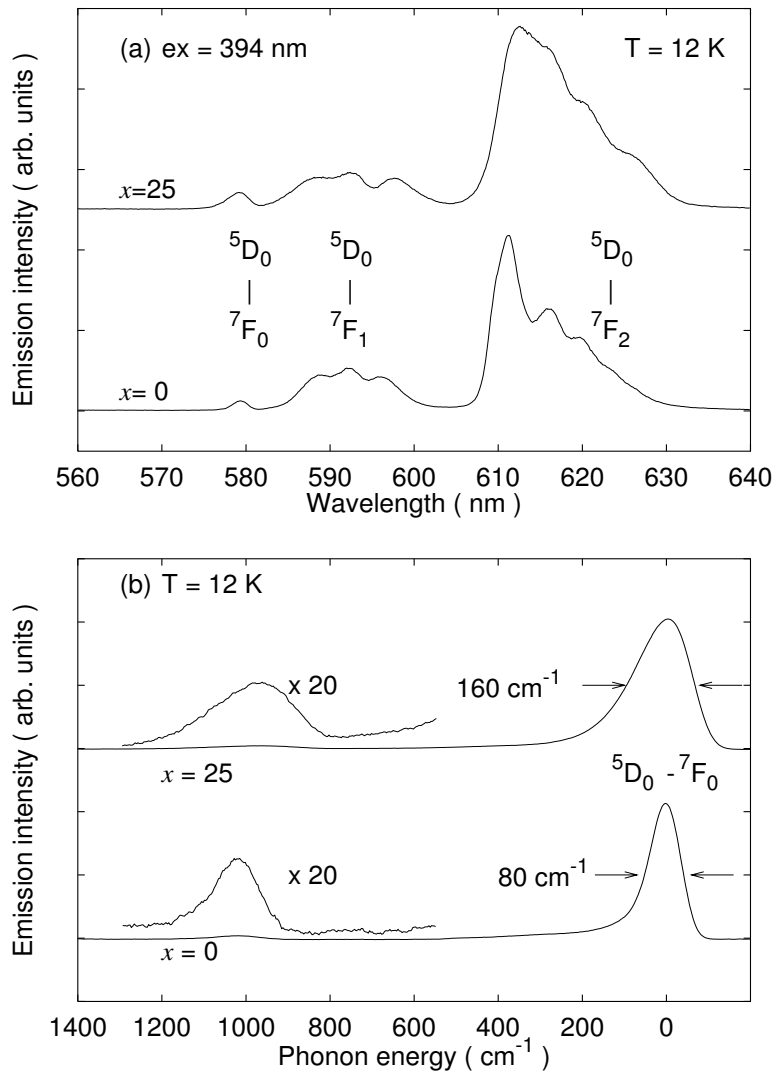
Figure 3.7: (a) Fluorescence spectra at 12 K for $(75 - x)SiO_2 \cdot xAlO_{3/2} \cdot 25$ $NaO_{1/2} \cdot 1.0EuO_{3/2}$ ($x = 0, 25$) glasses. The excitation wavelength is 394 nm. (b) Excitation and phonon sideband (PSB) spectra at 12 K for $(75 - x)$ $SiO_2 \cdot xAlO_{3/2} \cdot 25NaO_{1/2} \cdot 1.0EuO_{3/2}$ ($x = 0, 25$) glasses obtained by monitoring the $^5D_0 - {}^7F_2$ transition. In both spectra, the horizontal axis denotes the energy of phonon absorbed in the $^5D_0 - {}^7F_0$ transition. The PSB spectra are magnified by a factor of 20.

75SiO_2·25$NaO_{1/2}$·1.0$EuO_{3/2}$ and 50SiO_2·25$AlO_{3/2}$·25$NaO_{1/2}$·1.0$EuO_{3/2}$ glasses at 12 K. The excitation spectra were obtained by monitoring the $^5D_0 - {}^7F_2$ transition at 612 nm. In the figure, the excitation wavelength was represented as a relative energy in wavenumber with respect to the center of gravity of a pure electronic transition between $^5D_0$ and $^7F_0$ states. The $^5D_0 - {}^7F_0$ transition consists of a single band due to the nondegenerate ground ($^7F_0$) and excited states ($^5D_0$), and a full width at half maximum of the band, which reflects a site-to-site variation in the local environment of Eu^{3+}, is about 80 and 160 cm^{-1} for 50SiO_2·25$AlO_{3/2}$·25$NaO_{1/2}$·1.0$EuO_{3/2}$ and 75SiO_2·25$NaO_{1/2}$·1.0$EuO_{3/2}$ glasses, respectively. In Fig. 3.7(b), distinct phonon sideband spectra, the intensity of which is multiplied by a factor of 20, can be seen in the range of 900~1100 cm^{-1}. The PSB spectra are observed around 1050 cm^{-1} in silicate glass, and around 950 cm^{-1} in aluminosilicate glass.

Optical absorption spectra of $(75 - x)SiO_2$·$xAlO_{3/2}$·25$NaO_{1/2}$·1.0$EuO_{3/2}$ ($x = 0, 25$) glasses at room temperature are shown in Fig. 3.8(a). It is found that the intense absorption is observed at around 400 nm for aluminosilicate glass, while the absorption at about 400 nm is not recognized for silicate glass. In Fig. 3.8(b) is shown room temperature fluorescence spectrum of Eu^{3+} in 50SiO_2·25$AlO_{3/2}$·25$NaO_{1/2}$·1.0$EuO_{3/2}$ glasses in the wavelength range of 400 to 700 nm. The excitation is performed at the ultraviolet light with wavelength of 394 nm. In addition to the emission peaks around 600 nm due to Eu^{3+} as seen from Fig. 3.7(a), the emission band at around 460 nm, the intensity of which is enlarged by a factor of 30, obviously appears as a broad spectrum. The broad emission band is ascribed to the transition from the $4f^65d$ to $4f^7$ levels of Eu^{2+} [28]. This implies that the intense absorption and broad emission in the ultraviolet to blue region are induced by the presence of some Eu^{2+} ions in the aluminosilicate glass.

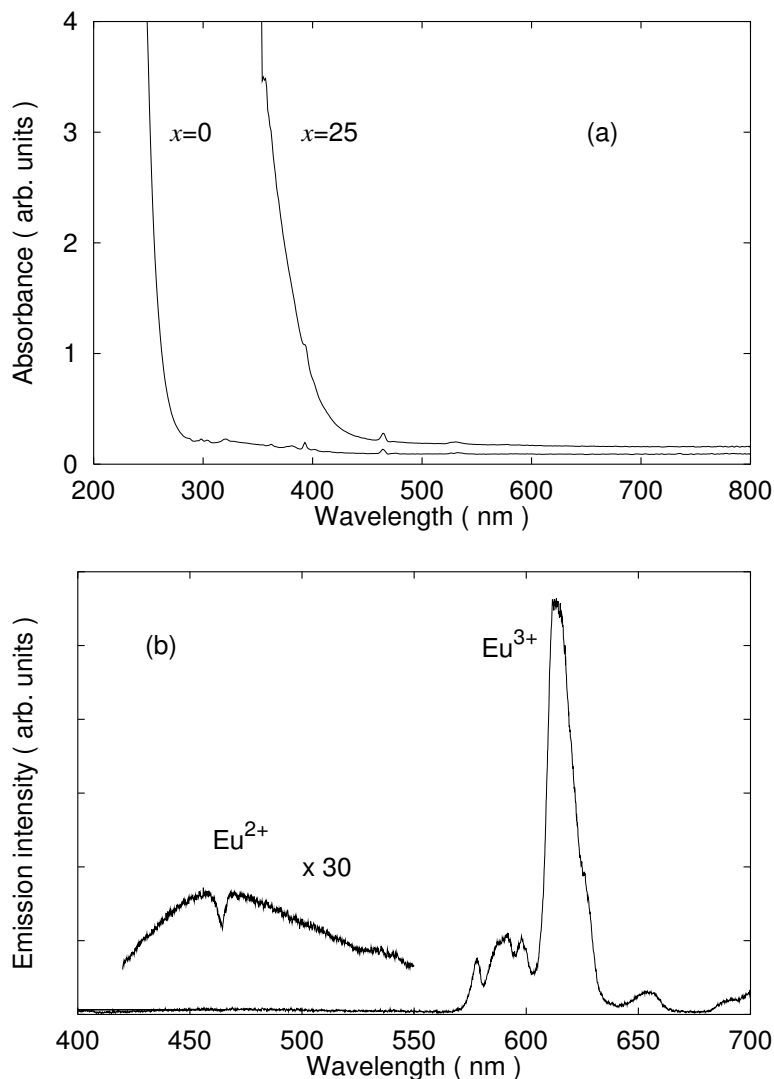In Fig. 3.9 the fluorescence decay curve is shown for the $^5D_0$ state of

Figure 3.8: (a) Optical absorption spectra at room temperature of $(75 - x)\mathrm{SiO_2} \cdot x\mathrm{AlO_{3/2}} \cdot 25\mathrm{NaO_{1/2}} \cdot 1.0\ \mathrm{EuO_{3/2}}$ ($x = 0,\ 25$) glasses. (b) Fluorescence spectrum at room temperature for $50\mathrm{SiO_2} \cdot 25\mathrm{AlO_{3/2}} \cdot 25\mathrm{NaO_{1/2}} \cdot 1.0\mathrm{EuO_{3/2}}$ glass. The excitation wavelength is 394 nm. The broad emission at around 460 nm is magnified by a factor of 30. A small dip of emission intensity takes place at 460 nm, since the light with wavelength of about 460 nm causes the excitation of $\mathrm{Eu^{3+}}$.

Eu^{3+} in $50SiO_2 \cdot 25AlO_{3/2} \cdot 25NaO_{1/2} \cdot 1.0EuO_{3/2}$ glasses under the excitation of wavelength of 580 nm at 12 K. The decay curve is approximately exponential, and the lifetime is estimated as 1.67 ± 0.02 ms. Figure 3.10 shows typical hole spectra of Eu^{3+} in $50SiO_2 \cdot 25AlO_{3/2} \cdot 25NaO_{1/2} \cdot 1.0EuO_{3/2}$ glass at 4.2, 6.4, 7.7, 10.4 and 16.5 K obtained by the irradiation of 580.0 nm laser light. In all the spectra, the burning wavelength is 580.0 nm, and the burning time is 300 s. The full width of the holes is estimated as 1.35 ± 0.05, 2.99 ± 0.10, 3.53 ± 0.02, 4.08 ± 0.08 and 6.44 ± 0.10 GHz, respectively; the hole width becomes wider and the depth grows shallower with increasing temperature. At higher temperatures, a long irradiation time of laser light is needed to obtain a hole which has
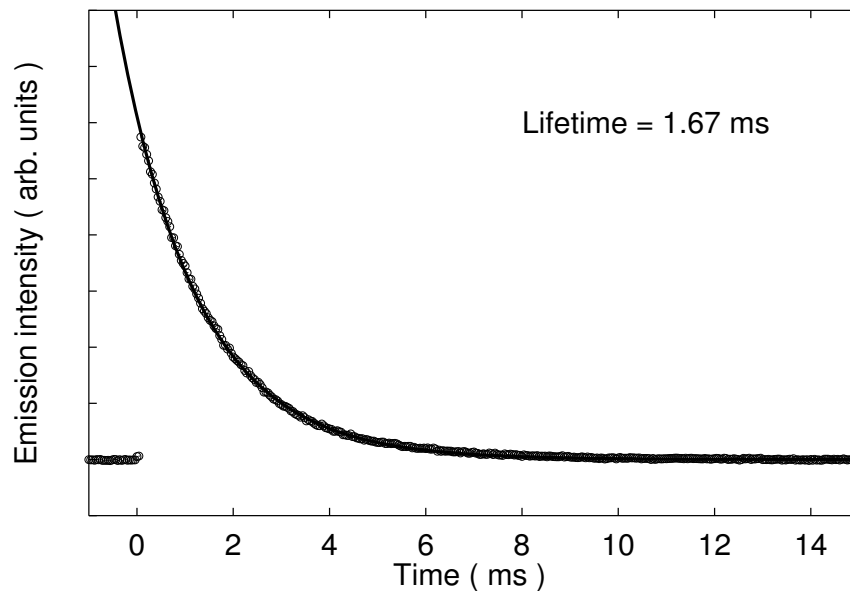

Figure 3.9: Fluorescence decay curve at 12 K for the $^5D_0$ state of Eu^{3+} in $50SiO_2 \cdot 25AlO_{3/2} \cdot 25NaO_{1/2} \cdot 1.0EuO_{3/2}$ glass. The excitation wavelength is 580.0 nm. In the figure, the solid curve represents an exponential function fitted to data points (open circles).
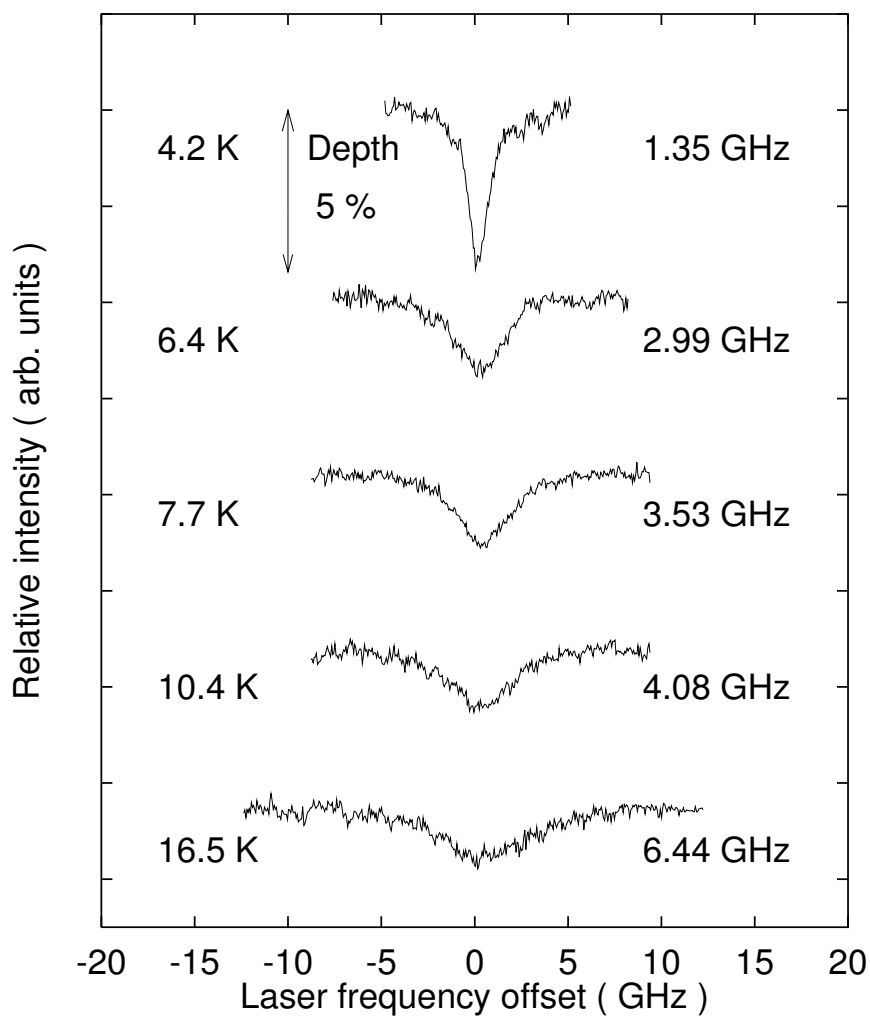
Figure 3.10:   Holes burned in the $^5D_0$ – $^7F_0$ transition of Eu^{3+} in $50SiO_2 \cdot 25AlO_{3/2} \cdot 25NaO_{1/2} \cdot 1.0EuO_{3/2}$ glass at various temperatures. In all the spectra, the burning wavelength is 580.0 nm, and the burning time is 300 s. The measurement temperature and the full width at half maximum of the burned hole are shown at the left and right sides, respectively.

the same depth as the hole burned at 4.2 K. A hole was hardly detected above
25 K. Moreover, the hole burned at 4.2 K disappeared in a temperature cycle
of $T >$50 K. On the other hand, an attempt was made to burn holes under the
same conditions for $75SiO_2 \cdot 25NaO_{1/2} 1.0EuO_{3/2}$ glass, but the persistent holes
were not observed.

3.3.4 Discussion

Macfarlane and Shelby [12] reported two types of mechanisms to cause a spec-
tral hole in glass. One is an optical pumping mechanism which is ascribed
to the redistribution of population among the quadrupole sublevels. This
mechanism is observed for $^5D_0 - {}^7F_0$ transition of Eu^{3+} in a silicate glass,
and is dominant at low temperatures ($T < 4.0$ K) where the homogeneous
linewidth is less than the ground-state quadrupole splitting. The other is a
non-photochemical process which involves an optically induced rearrangement
of local structure, being observed in the $^3H_4 - {}^1D_2$ transition of Pr^{3+} in silicate
glass. In the former case, antiholes at both sides of the hole are observed in
the hole spectra, and the hole are not formed at higher temperatures, where
the hole linewidth exceeds the quadrupole splitting, and the relaxation rate
among quadrupole sublevels is fast enough. In the present aluminosilicate
glasses, the hole is stable for more than 1 h and can be burned at relatively
high temperatures. In addition, there exist no antiholes in the hole spectra,
which would appear in the frequency range within ~ 100 MHz and ~ 300 MHz
from the resonant hole [25]. Therefore, the latter mechanism is likely applied
to the aluminosilicate glasses doped with Eu^{3+} ions. On the other hand, an
attempt was made to burn a hole and measure a hole spectrum in silicate glass
under the same conditions, but it was impossible to observe persistent holes
above 4.2 K at least. This result is consistent with that reported by Schmidt,
Macfarlane and Völker [25], where persistent spectral holes are not observed
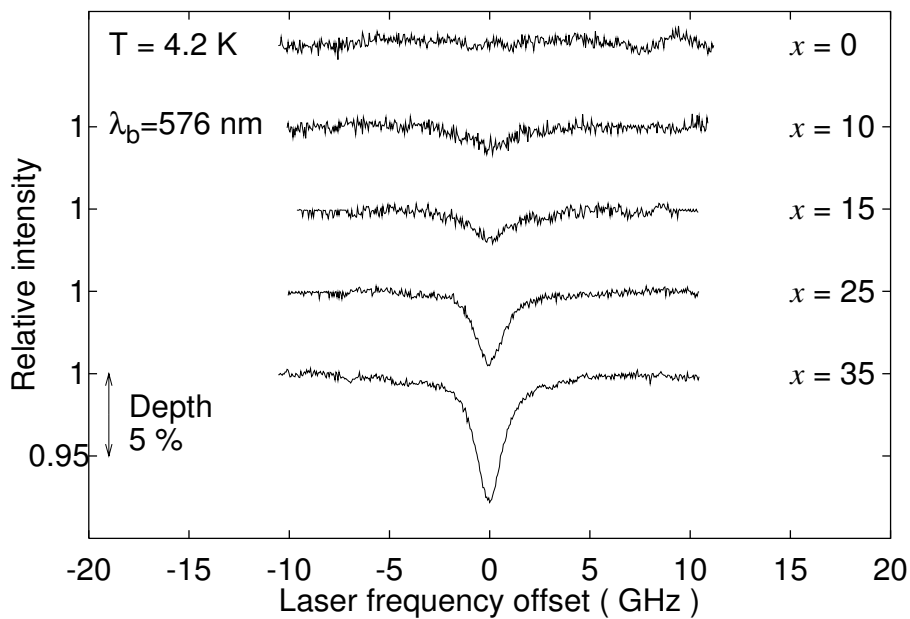
Figure 3.11: Hole spectra for the $^5D_0$ – $^7F_0$ transition of Eu^{3+} in $(75 - x)SiO_2 \cdot xAlO_{3/2} \cdot 25NaO_{1/2} \cdot 1.0\ EuO_{3/2}$ ($x=0$, 10, 15, 25, 35) glasses at 4.2 K. In all the spectra, the burning wavelength is 576.0 nm, and the burning time is 300 s.

for the Eu^{3+} in silicate glass. Additionally, the transient holes due to the optical pumping mechanism are also undetected in the present silicate glass above 4.2 K because of the short hole lifetime. Figure 3.11 shows holes burned in the $^5D_0$ – $^7F_0$ transition of Eu^{3+} in $(75 - x)SiO_2 \cdot xAlO_{3/2} \cdot 25NaO_{1/2} \cdot 1.0EuO_{3/2}$ ($x =0$, 10, 15, 25, 35) glasses at 4.2 K. The burning wavelength is 576.0 nm, and the burning time is 300 s. As the concentration of Al_2O_3 increases, the hole linewidth decreases and the hole depth increases. Thus, it is evident that the addition of Al_2O_3 to silicate glass causes a drastic change in the hole character and linewidth, and subsequently, long-lived holes are burned even above 4.2 K.

It was found that the introduction of Al^{3+} in silicate glass has the effects on the valence state of europium ion and the inhomogeneous linewidth of $^5D_0 - {}^7F_0$ transition as well. These phenomena are related to the local structure around europium ion. Todoroki *et al.* [29] performed ^{151}Eu Mössbauer spectroscopy for sodium aluminosilicate glasses with compositions similar to the present glasses, and investigated the compositional dependence of isomer shift of ^{151}Eu^{3+} in these glasses. They revealed that the covalency of $Eu^{3+}-O$ bond decreases with increasing Al_2O_3 content. This is because the local basicity around Eu^{3+} decreases with a decrease in nonbridging oxygens, which is caused by the incorporation of AlO_4 group in the glass, as shown Fig. 3.12. This is also supported by the measurements of phonon sideband (PSB) spectra as shown in Fig. 3.7(b). In silicate glass, the PSB appears at around 1050 cm^{-1}, while in aluminosilicate glass, the peak position of PSB shifts to a lower energy side near 950 cm^{-1}. The lowering of phonon energy of ligands coupled with an Eu^{3+} ion is attributed to the formation of Si-O-Al bond with lower phonon energy than that of Si-O-Si bond. Besides, the glass network structure is rigid in the aluminosilicate glass because of a lack of nonbridging oxygens, so that the Eu^{3+} ions must occupy various sites, while the glass network structure is flexible in the silicate glass due to the presence of nonbridging oxygens introduced by Na$^+$ ions, so that the positive charge of the Eu^{3+} ion is compensated by the nonbridging oxygens more readily. As a result, the site-to-site variation in the $^5D_0 - {}^7F_0$ transition of Eu^{3+} becomes much larger in aluminosilicate glass than in silicate glass. Furthermore, not only the low local basicity and but also the high melting temperature (1600 °C) for aluminosilicate glass brings about a reduction of some amounts of trivalent europium ions, i.e., a production of divalent europium ions. The evidence is provided by the observation of the $4f^65d - 4f^7$ transition due to Eu^{2+} as shown in Figs. 3.8(a) and (b). In contrast, the divalent europium ions were not detectable in silicate glass.

$$Al_2O_3$$

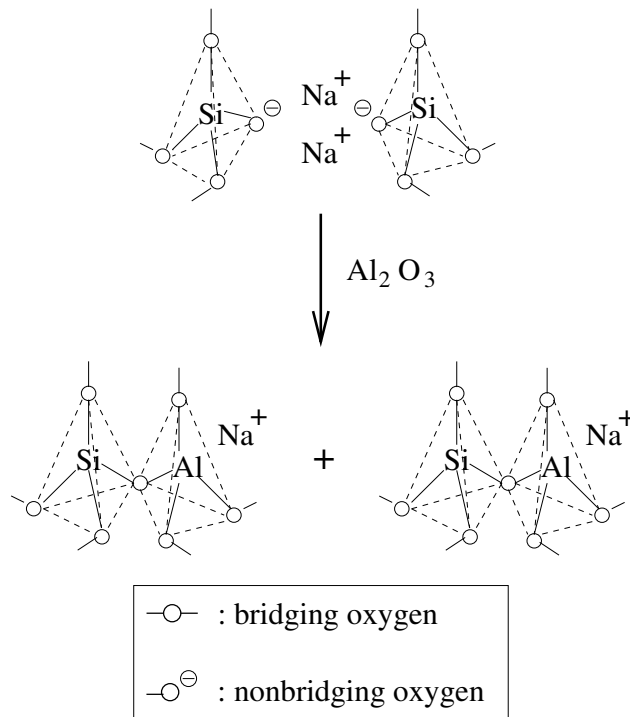-O- : bridging oxygen

-O⊖ : nonbridging oxygen

Figure 3.12: A structural change induced by an incorporation of Al_2O_3 into silicate glass.

Also, an attempt was made to burn several persistent holes with different frequencies at the same laser beam position in $50SiO_2 \cdot 25AlO_{3/2} \cdot 25NaO_{1/2} \cdot 1.0EuO_{3/2}$ glass. The results are shown in Fig. 3.13. The burning time is 300 s in all the spectra. The top spectral profile corresponds to a hole burned in the $^5D_0 - {}^7F_0$ transition of Eu^{3+} at 6.0 K obtained by the irradiation of 580.0 nm laser light. In the two lower profiles, each of new holes represented by arrows affect the depth of the previously burned holes. This indicates that the potential barrier between electronic states of Eu^{3+} ions before and after burning is not so high. In addition, as mentioned above, the persistent holes do not survive temperature cycling above 50 K. The relatively low activation
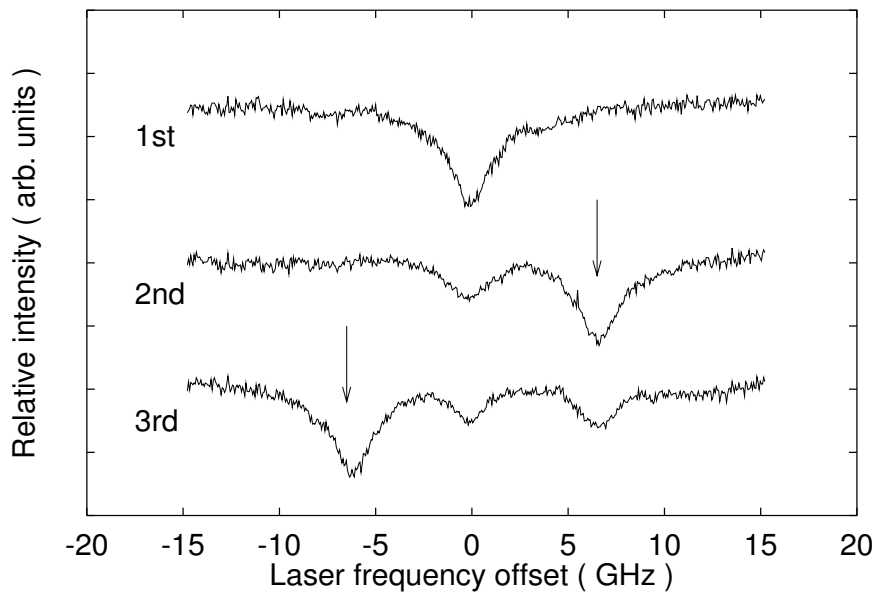
Figure 3.13: Multiple hole spectra for the $^5D_0 - {}^7F_0$ transition of Eu^{3+} in $50SiO_2 \cdot 25AlO_{3/2} \cdot 25NaO_{1/2} \cdot 1.0EuO_{3/2}$ glass at 6.0 K. The arrows represent the positions of holes burned newly with different laser frequencies. All the spectra are drawn in the same scale.

energy for the hole filling and the erasure of hole supports a photophysical rearrangement of the local environment around Eu^{3+}.

Figure 3.14 (a) shows holes burned in the $^5D_0 - {}^7F_0$ transition of Eu^{3+} in $50SiO_2 \cdot 25AlO_{3/2} \cdot 25NaO_{1/2} \cdot 1.0EuO_{3/2}$ glass at 6.0 K for different burning times. In Fig. 3.14(b), the hole width is plotted as a function of burning time. It is found that both the hole linewidth and the depth grow larger as the burning time, t_b, is increased. From the theoretical consideration based on the assumption that the homogeneous spectrum is a Lorentzian shape and that the burning time, t_b, is short, the hole linewidth, H, is given by [30]

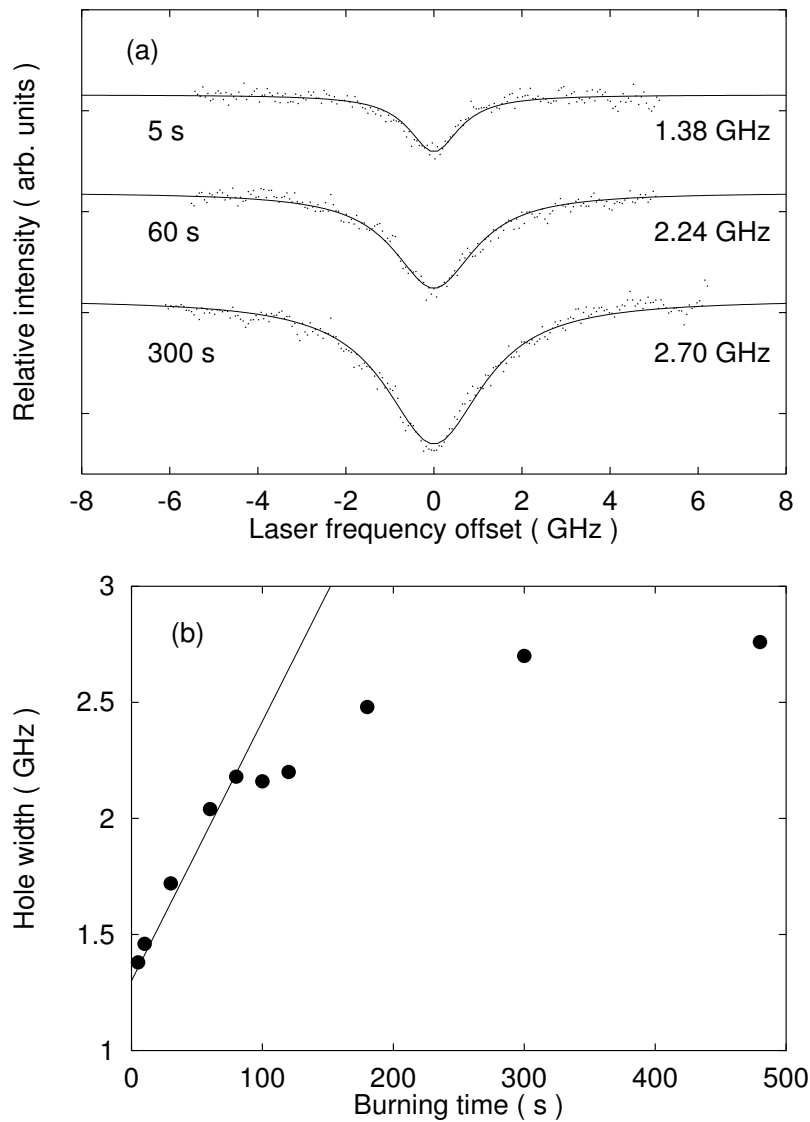$$H(t_b) \approx 2\Gamma_h + \alpha t_b, \tag{3.6}$$

Figure 3.14:   (a) Burning time dependence of hole spectrum for $50SiO_2 \cdot 25AlO_{3/2} \cdot 25NaO_{1/2} \cdot 1.0EuO_{3/2}$ glass at 6.0 K. The solid curves represent Lorentzian functions fitted to the data points (dots). The measurement temperature and the burning time are shown at the left and right sides, respectively.   (b) Hole linewidth at 6.0 K as a function of burning time for $50SiO_2 \cdot 25AlO_{3/2} \cdot 25NaO_{1/2} \cdot 1.0EuO_{3/2}$ glass.

where Γ_h is the homogeneous linewidth and α is a constant. From the extrapolation of hole linewidth to $t_b = 0$ (see the solid line in Fig. 3.14(b), zero-burning limit), $H(0)/2$ was calculated, and the value of Γ_h was 0.65 GHz at 6.0 K. This value is about 50 % smaller than that at $t_b = 300$ s which is obtained as $H(t_b)/2$.

In general, the homogeneous linewidth, Γ_h, in Hz is represented in terms of using the energy relaxation time, T_1, and pure dephasing time, T_2^*, as [31]

$$\Gamma_h(T) = \frac{1}{\pi} \left(\frac{1}{2T_1} + \frac{1}{T_2^*} \right). \tag{3.7}$$

As demonstrated from the fluorescence decay curve shown in Fig. 3.9, the value of T_1 is a few ms for the $^5D_0 - {}^7F_0$ transition of Eu^{3+} in the 50SiO$_2$·25AlO$_{3/2}$·25 NaO$_{1/2}$·1.0EuO$_{3/2}$ glass at 580 nm. Judging from this value of T_1, $1/2\pi T_1$ is about 100 Hz, which is approximately $10^6 \sim 10^7$ times smaller than the observed hole linewidth. Therefore, the magnitude of Γ_h is mainly dominated by T_2^* in the $^5D_0 - {}^7F_0$ transition of Eu^{3+} in the aluminosilicate glass at 580 nm.

In Fig. 3.15 is shown the temperature dependence of Γ_h for the $^5D_0 - {}^7F_0$ transition of Eu^{3+} in 50SiO$_2$·25AlO$_{3/2}$·25NaO$_{1/2}$·1.0EuO$_{3/2}$ glass at 580.0 nm. Γ_h is found to show a T^2 -dependence above 8 K, while a nearly linear dependence is observed at the temperature range from 4.2 to 8 K. This temperature dependence agrees with that obtained in Eu^{3+} -doped silicate glass fiber by means of accumulated photon echos [24]. This implies that the temperature dependence of Γ_h is universal in Eu^{3+} -doped glass systems and is fundamentally different from that in a regular crystal such as Y$_2$O$_3$: Eu^{3+}, where Γ_h depends on T^7 at low temperatures according to the two-phonon Raman process [1]. Such a temperature behavior of Γ_h in glasses requires an additional degree of freedom in the vibrational density of state for the rare-earth ion in the glass, such as the interaction between electrons of optical center and an enhanced low frequency phonon mode or the interaction between the electrons
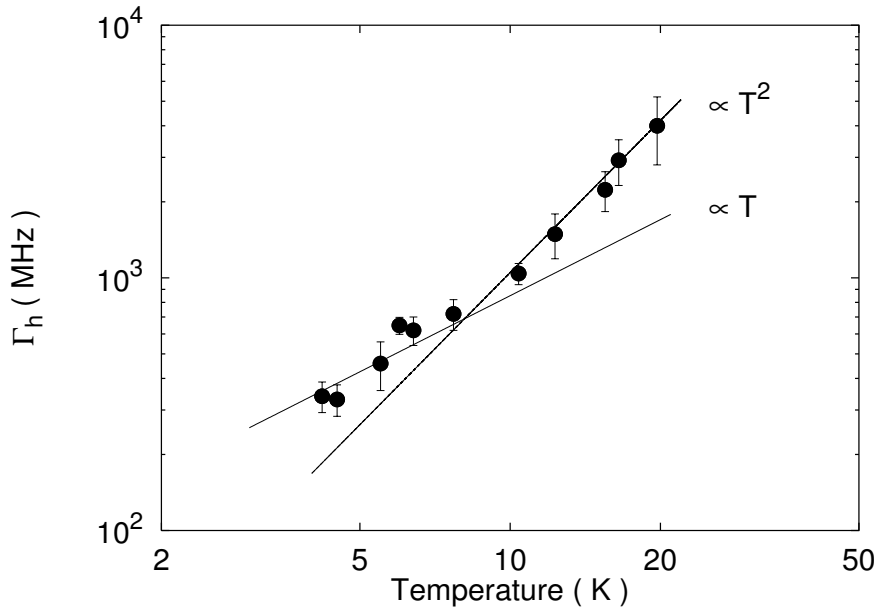
Figure 3.15: Homogeneous linewidth, Γ_h, as a function of temperature for $50\mathrm{SiO}_2 \cdot 25\mathrm{AlO}_{3/2} \cdot 25\mathrm{NaO}_{1/2} \cdot 1.0\mathrm{EuO}_{3/2}$ glass in log-log scale. The burning wavelength is 580.0 nm. The solid lines represent T - and T^2 -dependence, respectively.

and a two-level system (TLS).

In the Raman process with acoustic phonons, the temperature dependence obeys T^2 -law down to about $0.5 T_D$, where T_D is the Debye temperature of the solids. As for the aluminosilicate glass, $T_D = 1200$ K [32], and therefore, the Raman process with acoustic phonons can not usually explain the T^2 - dependence down to 10 K. Some theories [2, 3, 33] showed that the nearly quadratic temperature dependence of Γ_h observed for the $^5D_0 - {}^7F_0$ transition of Eu^{3+} in various glasses in a wide temperature range above about 10 K [17–19, 24] can be explained in terms of the relaxation due to the two-phonon Raman process. For instance, Huber [3] calculated Γ_h for the impurity ion in

silicate glass ($T_D = 500$ K), assuming the two-phonon Raman process in the temperature range between 10 and 300 K with a distribution of nonacoustic low-frequency phonon modes obtained from inelastic neutron-scattering data. He revealed that when the interaction of the optical center with such low-frequency phonons depends on the amplitude in vibration of atoms rather than the strain in solids, the nearly quadratic temperature dependence of Γ_h holds down to relatively low temperatures. On the other hand, Γ_h in Eu^{3+} -doped silicate glass exhibited a linear dependence at temperatures below about 4.2 K [24–26,34]. Several models including a coupling of electrons to TLS were proposed to explain the T -linear dependence of Γ_h at such low temperatures [4–6]. Thus, a cross-over from T - to T^2 -dependence is expected for Eu^{3+} -doped glass systems between 4.2 and 20 K.

3.3.5   Conclusion

Persistent spectral hole burning was successfully observed for Eu^{3+} in sodium aluminosilicate glasses. The holes can be burned up to about 20 K and erased when the temperature is raised up to at least 50 K. The hole is stable for more than 1 h and is accompanied with no antiholes. This suggests that the persistent hole is burned via a photophysically induced rearrangement of the local structure around Eu^{3+}. With an increase in Al_2O_3 content, the hole width becomes narrower and the depth grows shallower. In silicate glass without Al_2O_3, however, the persistent spectral holes are not observed above 4.2 K under the same conditions. Therefore, an introduction of Al^{3+} has the drastic effects on the formation of persistent holes and the hole linewidth. The homogeneous linewidth for the $^5D_0 - {^7}F_0$ transition of Eu^{3+} in aluminosilicate glass is found to vary linearly with temperature below 8 K and to show a quadratic temperature dependence above 8 K. The difference in the local structure between aluminosilicate and silicate glasses is reflected in the inhomogeneous linewidth

as well; the inhomogeneous linewidth for the $^5D_0 - {}^7F_0$ transition of Eu^{3+} in aluminosilicate glass is twice larger than that in silicate glass.

3.4 Persistent spectral hole burning of $\mathbf{Pr^{3+}}$ ions in sodium silicate glasses

3.4.1 Introduction

Low-temperature properties of glasses have been extensively studied by a number of researchers from experimental and theoretical standpoints. In glasses, there are excitation mode of very low energies, which dominate the thermal and acoustic properties at low temperatures. A familiar concept which is responsible for the low-temperature properties is tunneling mode or two-level system [10, 11]. The two-level system (TLS) is modeled as a distribution of double-well potentials where ion or molecule can tunnel from one potential minimum to another, although the origin of low-frequency energy is still unknown. Due to their low-excitation energies, even at very low temperatures a large number of the tunneling mode or TLS can still be thermally excited, thereby giving rise to anomalous properties in the amorphous solids. For instance, the specific heat manifests a T -linear dependence in contrast with the Debye's T^3 -law, and the thermal conductivity exhibits a quadratic dependence on temperature. Each dependence is quite different from that observed in pure crystals. The anomalous temperature dependence is also observed for the homogeneous linewidth (Γ_h) of optical transitions in impurity (ion or molecule) -doped glasses at low temperatures; in nearly pure crystal, Γ_h obeys the T^7 -law, which is well explained based on impurity-phonon interaction such as the Raman process [35], while for a variety of glasses, the temperature dependence of Γ_h is given by T^α with $\alpha =$1∼2 [7].

Spectral hole burning of rare-earth ions in inorganic glasses is one of fundamental ways to obtain Γ_h. The spectral hole burning occurs when a frequency-selected subset of rare-earth ion is altered in its state via a variety of mecha-

nisms; change of valence of rare-earth ion, population storage in the electronic excited state and/or in hyperfine levels of ground state and modification of optical transition frequency through a structural change. The last one is typical of disorder materials such as glasses. It is believed that Pr^{3+} in silicate glasses shows persistent spectral hole burning (PSHB) which is due to a local rearrangement of glass structure surrounding Pr^{3+} [12]. The temperature dependence of Γ_h follows $T^{1.3}$ from 0.4 to 12 K. This phenomenon is explained in terms of TLS, which contributes to low-temperature specific heat of glass [26]. Several models based on the interaction of TLS with the optical transition have been proposed to explain the temperature dependence of T^α with $\alpha = 1 \sim 1.3$ [5,6].

In contrast to a large number of optical dephasing measurements on rare-earth -doped inorganic glasses at high temperatures, very few data below 10 K have been reported. Due to the unknown random structure as well as the limited amount of available data on Γ_h at very low temperatures, there still remains several unresolved problems concerning the detailed mechanism which affects Γ_h and its temperature dependence. In order to fully understand the dynamical optical properties associated with the low-frequency excitation modes in inorganic glasses, it is important to clarify the relation between the glass composition and Γ_h. On the other hand, it appears that the static crystal field around the rare-earth ion also influences the coupling strength of the rare-earth ion with its surrounding host glass, i.e., the magnitude of Γ_h [25,34,36]. However, no attempt has been made to evaluate the dependence of both Γ_h and local structure on glass composition.

For GeO_2-Na_2O glasses doped with Pr^{3+}, it was reported that the hole linewidth and hole burning efficiency depend on Na_2O content [37], although the variation of static crystal field around Pr^{3+} with glass composition was not clarified. In the present section, the effect of Na_2O on PSHB is examined for

Pr^{3+} -doped SiO_2-Na_2O glasses. Especially, emphasis is placed on the compositional dependence of homogeneous linewidth and hole-burning efficiency. Also, fluorescence lifetime measurements are carried out for the $^1D_2$ state of Pr^{3+} to obtain information about the local structure around Pr^{3+}.

3.4.2   Experimental procedure

Glasses with compositions of $(100 - x)SiO_2 \cdot xNa_2O \cdot 0.1Pr_2O_3$ ($x = 10$, 20, 33.3, 45) were prepared from reagent-grade Pr_6O_{11}, Na_2CO_3 and SiO_2 as starting materials. The raw materials were mixed thoroughly in a porcelain motar and melted in a platinum crucible at $1500\sim1600$ °C for $1\sim2$ h. The melt was cooled slowly to room temperature. The resultant glass was cut into a rectangular parallelepiped shape of $10\times5\times5$ mm^3 and the glass surface was polished with CeO_2 slurry.

Emission and excitation spectra were obtained at 10 K using a cw Ar^+-laser-pumped dye laser (Spectra Physics 375B, rhodamin 6G dye, bandwidth$\sim$ 1 cm^{-1}) or a Xe lamp as a light source. The fluorescence was detected using a fluorescence spectrophotometer (Hitachi 850). Fluorescence lifetime measurements were performed at 10 K utilizing the same setup as in Section 3.3. The dye laser was operated with rhodamine 640 for the excitation of Pr^{3+} and the output of $^1D_2 \rightarrow {}^3H_5$ emission at around 700 nm was monitored.

Hole-burning measurements were also carried out using the same setup as in Section 3.3. In order to stabilize laser power, however, the present setup was slightly modified with respect to Section 3.3. The laser light was passed through an acoustic-optics modulator (AOM) and a non-diffracted beam is selected by a pin hole, which is partially reflected and detected by a PIN photodiode. The output laser power was stabilized to make the signal of the PIN photodiode constant changing the diffraction rate of the AOM. The scattered laser radiation was rejected by an appropriate color filter.

3.4.3   Results

Figure 3.16 shows emission and excitation spectra of $55SiO_2 \cdot 45Na_2O \cdot 0.1Pr_2O_3$ glass. The full line in this figure indicates the emission spectrum. The excitation was performed at a wavelength of 580 nm, which corresponds to the $^3H_4 \rightarrow ^1D_2$ transition of Pr^{3+}. In addition to the emission band at 600 to 640 nm originating from the $^1D_2 \rightarrow ^3H_4$ transition, the emission band which is assigned to the $^1D_2 \rightarrow ^3H_5$ transition is observed at around 700 nm. The energy level diagram for Pr^{3+} is depicted in Fig. 3.17. The initial state of the emission band can be ascribed to the lowest crystal-field (CF) component of $^1D_2$ because the multiphonon relaxation process from higher CF component states to lowest one takes place rapidly. The dotted line in Fig. 3.16 indicates excitation spectrum for the $^1D_2 \rightarrow ^3H_5$ emission at around 700 nm. The ab-
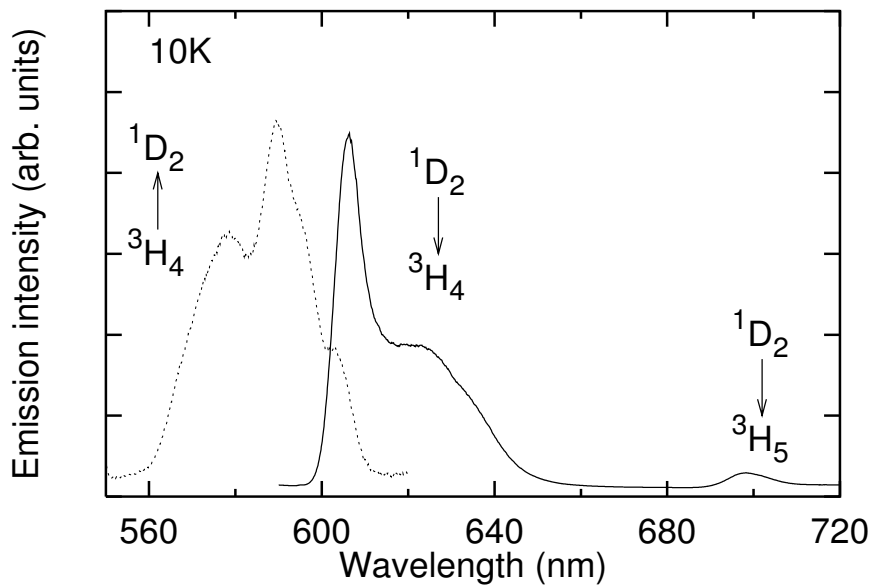

Figure 3.16: Emission (solid line) and excitation (dotted line) spectra at 10 K for $55SiO_2 \cdot 45Na_2O \cdot 0.1Pr_2O_3$ glass.
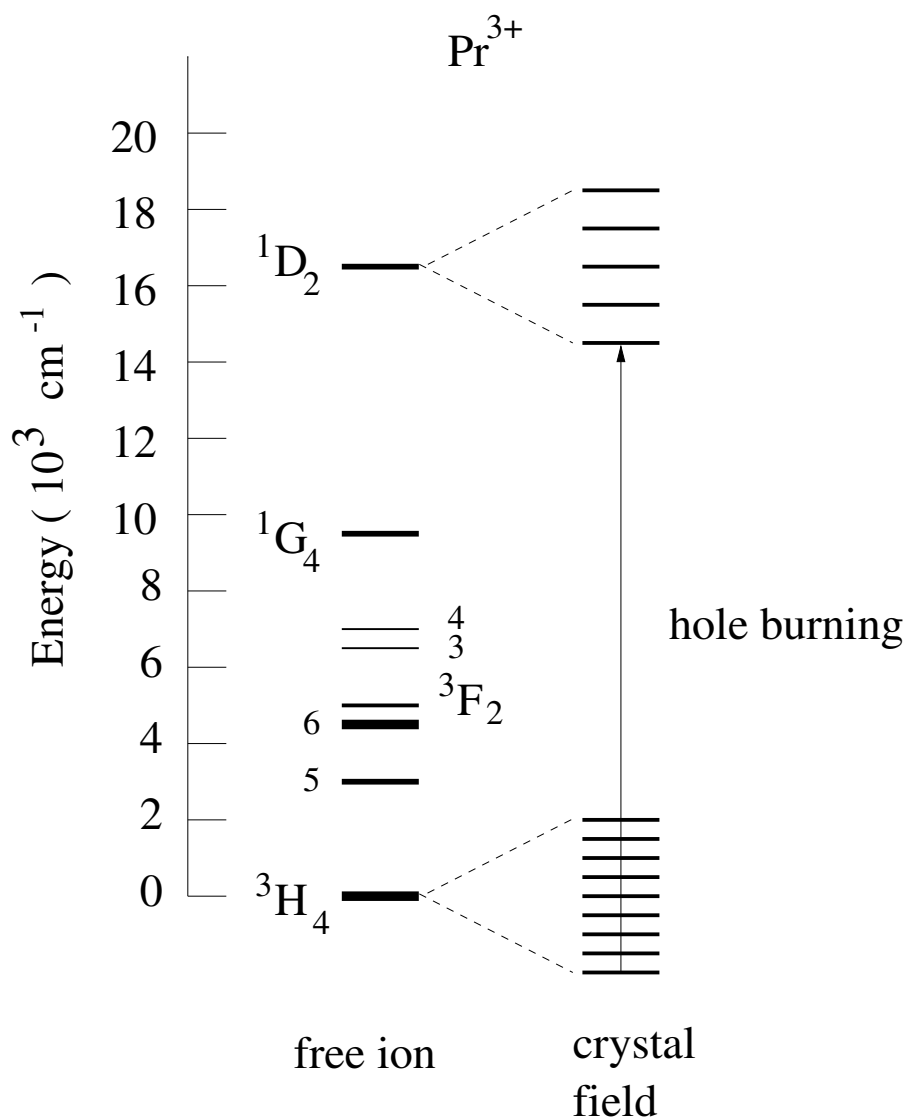
Figure 3.17: Energy level diagram of Pr^{3+}.

sorption band ranging from 560 to 610 nm is due to the CF components of the $^3H_4 \rightarrow {}^1D_2$ transition of Pr^{3+}. The shoulder observed at around 600 nm overlaps with the emission spectrum, suggesting that the overlapping region consists of the lowest CF component of $^1D_2$ state. Long-lived holes are burned only in the lowest CF component of $^1D_2$ state, but not in the higher CF components. This is ascribed to the fast relaxation from the higher CF levels to the lowest one [25].

Figure 3.18 shows fluorescence decay curves for the $^1D_2 \rightarrow {}^3H_5$ emission at around 700 nm in $(100-x)\,SiO_2 \cdot x\,Na_2O \cdot 0.1Pr_2O_3$ $(x{=}10,\ 20,\ 33.3,\ 45)$ glasses. The excitation was performed at a wavelength of 604 nm, which was the same as hole burning experiment as mentioned below. The decay curve is approximately fitted to a single exponential function, and the lifetimes are
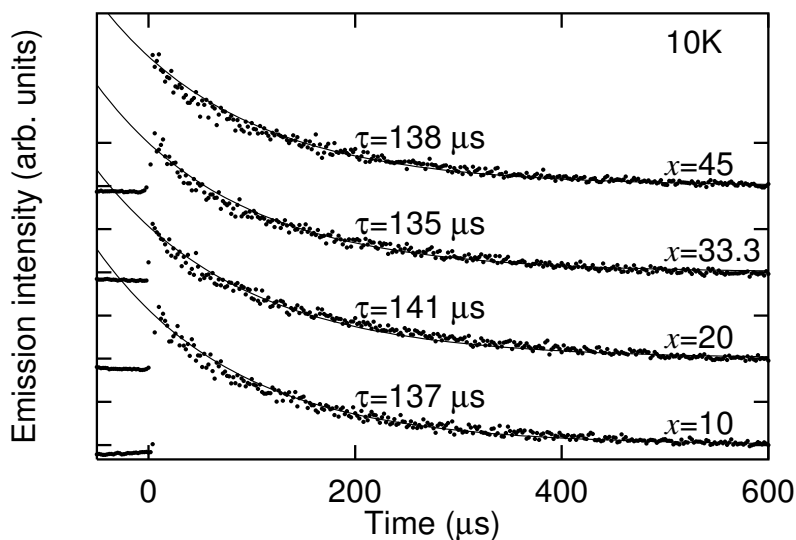

Figure 3.18: Fluorescence decay curve at 10 K for the $^1D_2$ state of Pr^{3+} in $(100-x)\,SiO_2 \cdot x\,Na_2O \cdot 0.1Pr_2O_3$ $(x{=}10,\ 20,\ 33.3,\ 45)$ glasses. The excitation wavelength is 604.0 nm.
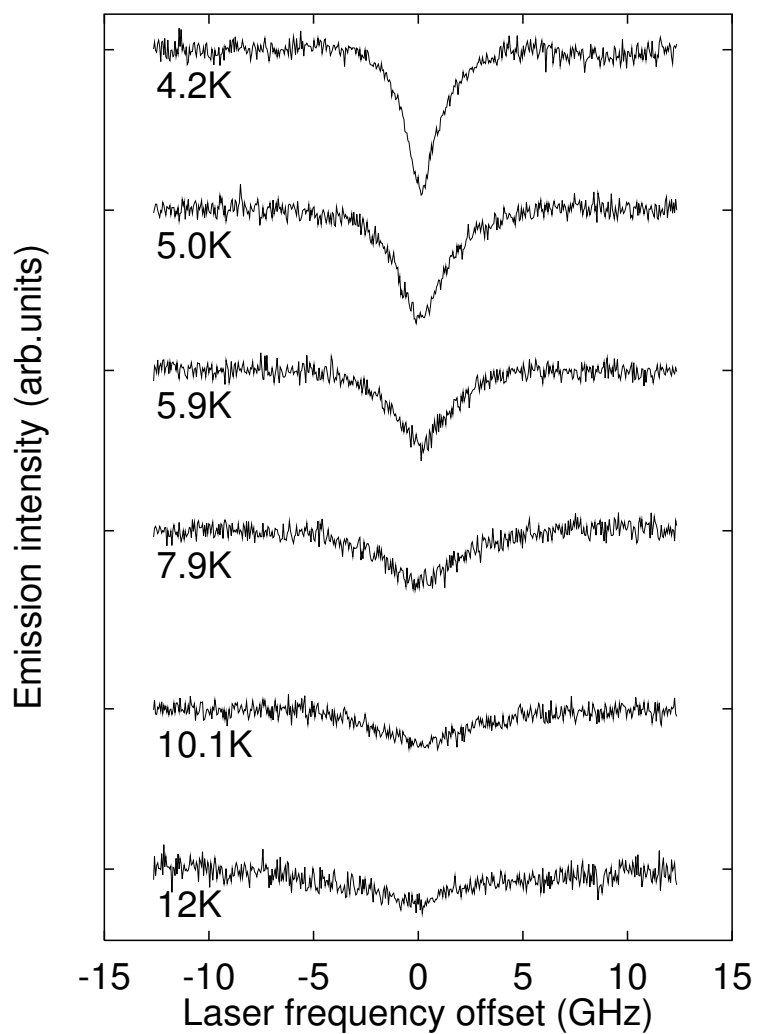
Figure 3.19: Holes burned in the $^1D_2$ – $^3H_4$ transition of Pr^{3+} in $55SiO_2 \cdot 45Na_2O \cdot 0.1Pr_2O_3$ glass at various temperatures. In all the spectra, the burning wavelength is 604.0 nm, and the burning time is 300 s.

estimated to be about 140 μs irrespective of Na_2O content.

Figure 3.19 shows typical hole spectra for $55SiO_2 \cdot 45Na_2O \cdot 0.1Pr_2O_3$ glass at 4.2 to 12 K. The hole was burned by the laser irradiation with a wavelength of 604.0 nm for 300 s in all the spectra. The hole spectrum was best fitted to a single Lorentzian function by a least squares method. As the temperature is increased, the hole linewidth becomes broader and the depth shallower. Under the present hole-burning conditions, the hole was not burned above 12 K for $55SiO_2 \cdot 45Na_2O \cdot 0.1Pr_2O_3$ glass and above 8 K for $90SiO_2 \cdot 10Na_2O \cdot 0.1Pr_2O_3$ glass.

Figure 3.20 shows the time dependence of hole linewidth for $(100-x)SiO_2 \cdot xNa_2O \cdot 0.1Pr_2O_3$ (x=10, 45) glasses at 4.2 K. The hole linewidth increases with an increase in the burning time for a short burning time. According to

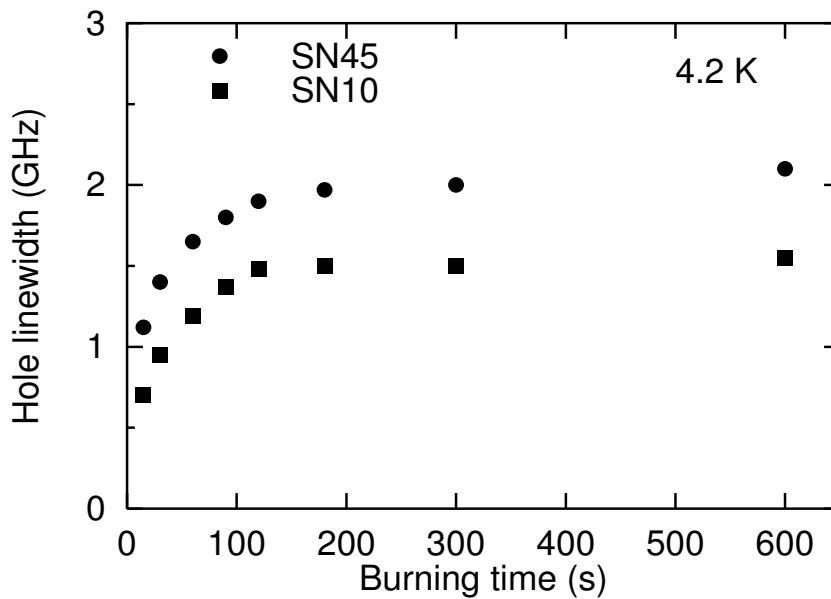Figure 3.20: Hole linewidth at 4.2 K as a function of burning time for $(100-x)SiO_2 \cdot xNa_2O \cdot 0.1Pr_2O_3$ ($x = 10$, 45) glasses.

Eq. (3.6), the homogeneous linewidth, Γ_h, is determined by calculating $H(0)/2$ from the extrapolation of hole linewidth to zero-burning time (zero-burning limit). For $90SiO_2 \cdot 10Na_2O \cdot 0.1Pr_2O_3$ glass, for example, The value of Γ_h was about 250 MHz at 4.2 K. This value is smaller by a factor of 3 with respect to that of $H(t_b)/2$ at $t_b = 300$ s as depicted in Fig 3.19. This procedure was used to determine Γ_h at each temperature.

Figure 3.21 shows the temperature dependence of Γ_h for $(100 - x)SiO_2 \cdot x$ $Na_2O \cdot 0.1Pr_2O_3$ (x=10, 45) glasses. The data points were fitted to a function of $\Gamma_h = aT^b$ by the least squares method, and the result is denoted by the solid line. The homogeneous linewidth, Γ_h, follows a $T^{1.2\pm0.1}$ dependence between
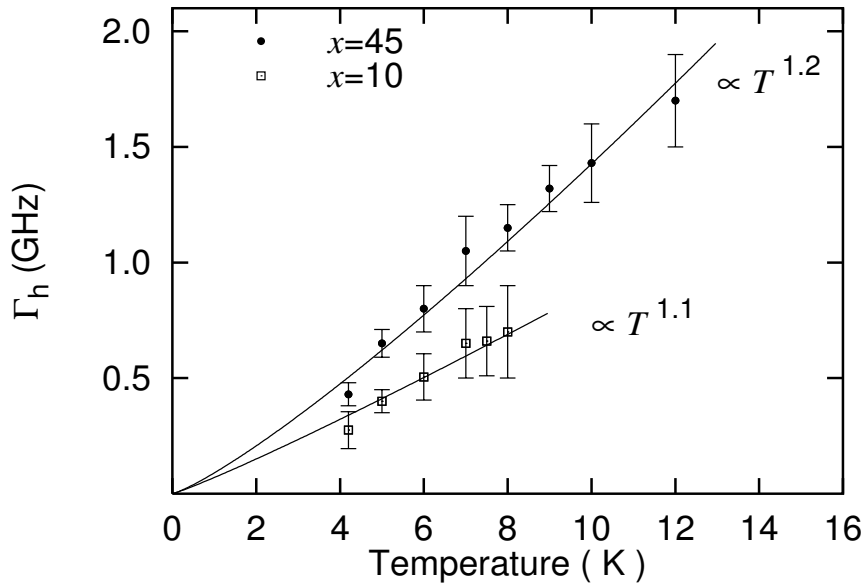
Figure 3.21: Homogeneous linewidth, Γ_h, as a function of temperature for $(100 - x)SiO_2 \cdot xNa_2O \cdot 0.1Pr_2O_3$ (x=10, 45) glasses. The burning wavelength is 604.0 nm. The solid lines represent $\Gamma_h \propto T^{1.2\pm0.1}$ for $55SiO_2 \cdot 45Na_2O \cdot 0.1Pr_2O_3$ glass, and $\Gamma_h \propto T^{1.1\pm0.1}$ for $90SiO_2 \cdot 10Na_2O \cdot 0.1Pr_2O_3$ glass.
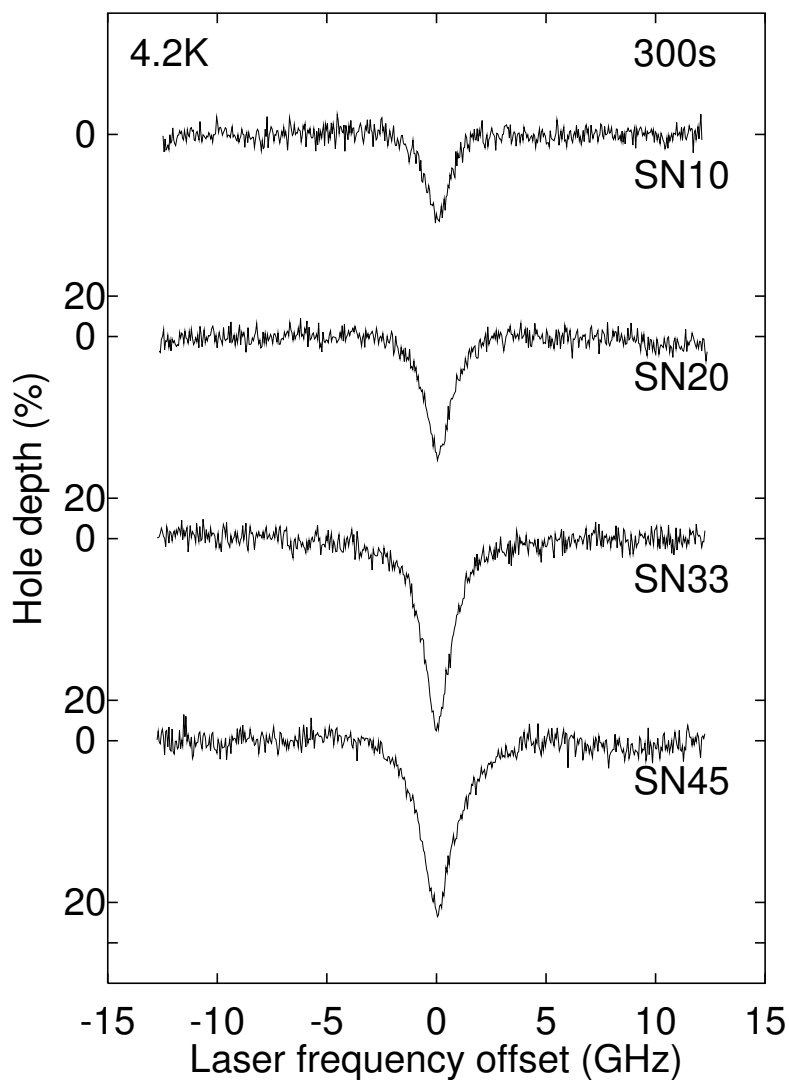
Figure 3.22: Hole spectra at 4.2 K burned in the $^1D_2 - {}^3H_4$ transition of Pr^{3+} in $(100 - x) SiO_2 \cdot x Na_2O \cdot 0.1 Pr_2O_3$ (x=10, 20, 33.3, 45) glasses. In all the spectra, the burning wavelength is 604.0 nm, and the burning time is 300 s.
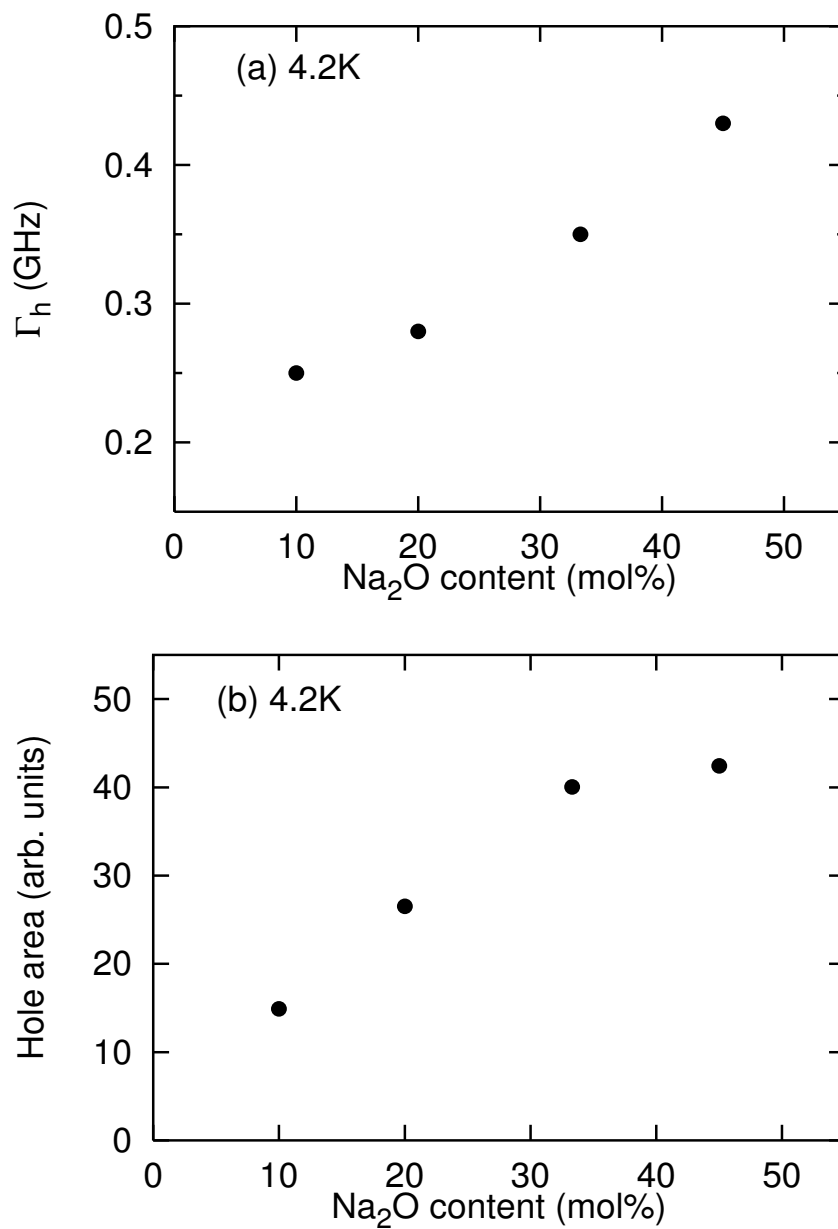
Figure 3.23: (a) Homogeneous linewidth, Γ_h, as a function of Na$_2$O content at 4.2 K. (b) Hole area at the burning time of 300 s as a function of Na$_2$O content at 4.2 K. The burning wavelength is 604 nm.

4.2 and 12 K for $55\mathrm{SiO}_2 \cdot 45\mathrm{Na}_2\mathrm{O} \cdot 0.1\mathrm{Pr}_2\mathrm{O}_3$ glass and a $T^{1.1\pm0.1}$ dependence between 4.2 and 8.0 K for $90\mathrm{SiO}_2 \cdot 10\mathrm{Na}_2\mathrm{O} \cdot 0.1\mathrm{Pr}_2\mathrm{O}_3$ glass.

The value of T_1 in Eq. (3.7) is $\sim 140\mu$s for the $^1D_2 - {}^3H_4$ transition at 604 nm as shown in Fig. 3.18. From this value of T_1, $1/2\pi T_1$ is estimated to be ~ 1 kHz, which is $4\sim5$ orders of magnitude smaller than the observed hole linewidth. Thus, the magnitude of Γ_h is governed mainly by T_2^*.

Figure 3.22 shows hole spectra for $(100-x)\,\mathrm{SiO}_2 \cdot x\mathrm{Na}_2\mathrm{O} \cdot 0.1\mathrm{Pr}_2\mathrm{O}_3$ ($x =$ 10, 20, 33.3, 45) at 4.2 K. The burning of hole was carried out at a wavelength of 604.0 nm for 300 s. The hole linewidth becomes wider and the depth deeper with an increase in $\mathrm{Na}_2\mathrm{O}$ content. From the extrapolation of the hole linewidth to zero-burning time as shown in Fig 3.20, the homogeneous linewidth was obtained. Furthermore, the hole area (hole linewidth$\times$depth) was determined at the burning time of 300 s. Figures 3.23(a) and (b) show the homogeneous linewidth and hole area as a function of $\mathrm{Na}_2\mathrm{O}$ content, respectively. Both the homogeneous linewidth and hole area tend to increase with an increase in $\mathrm{Na}_2\mathrm{O}$ content.

3.4.4   Discussion

Long-lived hole burning occurs only in the shoulder part of the absorption band at around 600 nm which corresponds to the lowest CF component of $^1D_2$ state as mentioned in the previous section. The hole lasted for more than 1 h and was burned at relatively high temperatures (~ 10 K). Such hole properties are presumably caused by a non-photochemical process which involves an optically induced rearrangement of the local environment around the optical center, unlike an optical pumping among nuclear hyperfine levels [25, 38]. The non-photochemical process is describable in terms of a double-well potential which can be modeled as the two-level system (TLS) where the interactions of the optical transition with the double-well potential or TLS are assumed to be

different in the ground and electronically excited states, respectively.

Hegarty *et al.* [39] measured the homogeneous linewidth, Γ_h, for Pr^{3+} in GeO_2 glass by means of fluorescence line narrowing (FLN), and revealed that Γ_h follows a quadratic temperature dependence above 13 K. Several theories [2,3] have shown that the quadratic temperature dependence of Γ_h above about 10 K can be explained based on a two-phonon Raman process. On the other hand, as shown in Fig. 3.21, Γ_h for both silicate glasses with $x = 10$ and 45 has a nearly linear temperature dependence below about 10 K, characteristic of phase relaxation due to the low-energy excitation modes in glasses, namely, TLS, which may be inherent in amorphous structure [26, 40]. According to the standard theory of TLS dephasing process [4–6, 41], $\Gamma_h \propto T^{1+\mu}$ if the energy dependence of TLS density of state, $\rho(E) \propto E^\mu$ and a dipolar coupling of the optical transition to TLS is assumed. As seen from Fig. 3.21, the composition of the sodium silicate glass influences the coupling strength between Pr^{3+} and its surrounding host glass, but does not affect the temperature dependence essentially.

In the optical dephasing process in which a dipole-dipole coupling between the optical center and TLS is assumed, the magnitude of Γ_h depends on not only the density and properties of TLS but also the distance between the Pr^{3+} ion and the surrounding host glass. In other words, the magnitude of Γ_h is influenced by the static crystal field around the Pr^{3+} ion as well. The variation of the static crystal field with glass composition can be evaluated from that of fluorescence lifetime which is dominated by the local structure around the Pr^{3+} ion. As shown in Fig. 3.18, the fluorescence lifetime for the $^1D_2$ state of Pr^{3+} is independent of Na_2O content. Since the energy gap between the $^1D_2$ and next lower $^1G_4$ is wide (see Fig. 3.17), the nonradiative transition due to multiphonon relaxation is expected to be negligibly small [42]. Also, in the case of an extremely low doping level of Pr^{3+} ions, the

nonradiative transition due to ion-ion interaction is assumed to be negligible, and thus, the lifetime of $^1D_2$ state is presumably dominated by the radiative transition. The variation in the lifetime of $^1D_2$ then corresponds to that of the electric dipole transition which is strongly affected by the local environment, i.e., the ligand asymmetry of rare-earth site and the bonding distance between the rare-earth ion and the ligand [43–45]. Therefore, the result in Fig. 3.18 suggests that the crystal field around Pr^{3+}, i.e., its first coordination shell remains unchanged over the whole composition. A similar concept has already been deduced from FLN studies on Eu^{3+} -doped sodium silicate glasses [46]; when the site-selective excitation is performed at a wavelength within the inhomogeneously broadened $^5D_0 - {}^7F_0$ transition of Eu^{3+}, the peak positions of individual components of the $^5D_0 \rightarrow {}^7F_1$ transition are independent of Na_2O content. Namely, the local environment around Eu^{3+} does not depend largely on the composition of the sodium silicate glass when the excitation wavelength is the same as each other. This is likely caused by the preferential coordination of the nonbridging oxygen adjacent to Na^+ to the rare-earth ion. In sodium silicate glasses, a sufficient amount of the nonbridging oxygens exist even in $90SiO_2 \cdot 10Na_2O$ glass. Therefore, it is expected that the ratio of the number of nonbridging oxygens to bridging oxygens within the first coordination shell of the rare-earth ion remains constant regardless of the Na_2O content so that the charge compensation of the trivalent rare-earth ion is accomplished. However, it should be noted that this is not the case for other conventional oxide glasses such as sodium borate, germanate and aluminosilicate glasses, owing to the change of bonding distance between the rare-earth ion and the ligand, i.e., the variation of the ratio of the number of nonbridging oxygens to bridging oxygens within its first coordination shell [46].

As shown in Fig. 3.23(a), the value of Γ_h varies with Na_2O content. Considering the fact that the decay of the $^1D_2$ fluorescence is independent of Na_2O

content, it is suggested that the variation of Γ_h with glass composition is not attributed to the effect of static crystal field due to the first coordination shell around Pr^{3+} but is influenced mainly by the density and microscopic nature of TLS. At the present stage, however, it is difficult to establish the origin of the postulated low-energy excitations, i.e., TLS. Here, it is tentatively assumed that the low-energy excitation modes in sodium silicate glasses are generated by Na^+ and/or nonbridging oxygens adjacent to Na^+ (NBO-Na^+) because they are not incorporated tightly in the glass matrix. In sodium silicate glasses, the amount of NBO-Na^+ increases monotonically with an increase in Na_2O content. This brings about an increase in the amount of NBO-Na^+ in the neighborhood of Pr^{3+}, i.e., second neighboring ions and longer-range arrangements of ions, without changing sufficiently its local environment, i.e., the first coordination shell as mentioned above. This situation enhances the electron-phonon coupling strength associated with the low-energy excitation modes, which we believe, originate from NBO-Na^+, leading to the larger value of Γ_h. In addition, as shown in Fig. 3.23(b), the hole area also increases an increase in the Na_2O content. Since the transition probability of the relevant transition of Pr^{3+} is independent of Na_2O content, the hole area is proportional to the number of ions burned by a non-photochemical process, and thus, the variation of the hole area in Fig. 3.23(b) is considered to reflect the hole-burning efficiency (η). Supposing persistent spectral hole burning (PSHB) is caused by the coupling with the low-energy excitation modes arising from NBO-Na^+, the local lattice rearrangement around Pr^{3+} takes place more readily when the number of the NBO-Na^+ is increased. Thus, the results shown in Figs. 3.23(a) and (b) can be understood by assuming that the density of state of low-energy excitation modes originating from NBO-Na^+, which may give rise to double-well potential or TLS, contributes to both Γ_h and η. Recently, Yugami *et al.* [47] demonstrated that PSHB occurs at 110 K for Eu^{3+} in Na^+-

β"-alumina which is a typical superionic conductor where Na^+ ions are mobile in the conduction plane. They carried the hole relaxation and temperature cycling measurements, and suggested that PSHB takes place by an optically activated motion of Na^+ near optical centers. The difference in hole properties between the SiO_2-Na_2O glasses and Na^+-β"-alumina, i.e., the fact that the hole disappears at lower temperatures in the SiO_2-Na_2O glasses, may come from the difference in the microscopic nature of low-energy excitation modes induced by Na^+ such as the barrier height and its distribution of double-well potential.

3.4.5   Conclusion

Low-temperature dynamical properties of SiO_2-Na_2O glasses doped with Pr^{3+} were systematically investigated by means of persistent spectral hole burning. The homogeneous linewidth of the $^1D_2 - {}^3H_4$ transition of Pr^{3+} as a function of temperature follows a $T^{1.2\pm0.1}$-dependence between 4.2 and 12 K for $55SiO_2 \cdot 45Na_2O \cdot 0.1Pr_2O_3$ glass and a $T^{1.1\pm0.1}$-dependence between 4.2 and 8.0 K for $90SiO_2 \cdot 10Na_2O \cdot 0.1Pr_2O_3$ glass. The nearly T-linear temperature dependence is consistent with the results deduced from some of theoretical models reported previously, if a dipole-dipole coupling between the Pr^{3+} ion and the two-level system is assumed. At liquid helium temperature, the homogeneous linewidth increases with an increase in Na_2O content, while the decay of $^1D_2$ fluorescence is independent of Na_2O content. From these results, it is proposed that the dependence of homogeneous linewidth on Na_2O content is not caused by the variation of local structure around Pr^{3+} but is affected mainly by the density and microscopic nature of low-energy excitations in the sodium silicate glasses. The hole-burning efficiency, as well as the homogeneous linewidth, increases with an increase in the Na_2O content. These results can be understand by assuming that the density of state of low-energy excita-

tion modes originating from Na$^+$ and/or nonbridging oxygens adjacent to Na$^+$ is responsible for the optical dephasing and persistent spectral hole burning.

References

[1] W. R. Babbit, A. Lezama, and T. W. Mossberg, Phys. Rev. B **39**, 1987 (1989).

[2] D. L. Huber, J. Non-Cryst Solids **51**, 241 (1982).

[3] D. L. Huber, J. Lumin. **36**, 327 (1987).

[4] D. L. Huber, M. M. Broer, and B. Golding, Phys. Rev. Lett. **52**, 2281 (1984).

[5] P. Reineker and K. Kassner, in *Optical Spectroscopy of Glasses*, edited by I. Zschokke (D. Reidel Publishing Company, Dordrecht, 1986), p. 65.

[6] R. Silbey and K. Kassner, J. Lumin. **36**, 283 (1987).

[7] For a review, see *Optical Linewidth in Glasses*, edited by M. J. Weber and M. D. Sturge (J. Lumin., **36**, 1987), p. 179.

[8] R. M. Macfarlane and R. M. Shelby, in *Spectroscopy of solids containing rare earth ions*, edited by A. A. Kaplyanskii and R. M. Macfarlane (North-Holland, Amsterdam, 1987), Vol. 21, p. 51.

[9] R. M. Macfarlane and R. M. Shelby, in *Persistent spectral hole burning: science and application*, edited by W. E. Moerner (Springer-Verlag, Berlin, 1988), p. 127.

[10] P. W. Anderson, B. I. Halpin, and C. M. Varma, Phylos. Mag. **25**, 1 (1972).

[11] W. A. Phillips, J. Low Temp. Phys. **7**, 351 (1972).

[12] R. M. Macfarlane and R. M. Shelby, Opt. Commun. **45**, 46 (1983).

[13] K. Hirao, S. Todoroki, and N. Soga, J. Lumin. **55**, 217 (1993).

[14] K. Hirao, S. Todoroki, D. H. Cho, and N. Soga, Opt. Lett. **18**, 1586 (1993).

[15] A. Kurita, T. Kushida, T. Izumitani, and M. Matsukawa, Opt. Lett. **19**, 314 (1994).

[16] A. Winnacker, R. M. Shelby, and R. M. Macfarlane, Opt. Lett. **10**, 350 (1985).

[17] P. Selzer, D. L. Huber, D. S. Hamilton, W. M. Yen, and M. J. Weber, Phys. Rev. Lett. **36**, 813 (1976).

[18] P. Avouris, A. Campion, and M. A. El-Sayed, J. Chem. Phys. **67**, 3397 (1977).

[19] J. R. Morgan and M. A. El-Sayed, Chem. Phys. Lett. **84**, 213 (1981).

[20] J. R. Morgan, E. P. Chock, W. D. Hopewell, M. A. El-sayed, and R. Orbach, J. Phys. Chem. **85**, 747 (1981).

[21] C. Brecher and L. A. Riseberg, Phys. Rev. B **13**, 81 (1976).

[22] K. Fujita, K. Tanaka, K. Hirao, and N. Soga, J. Appl. Phys. **81**, 924 (1997).

[23] W. Moerner, W. Lenth, and G. C. Bjorklund, in *Persistent spectral hole burning: science and application*, edited by W. Moerner (Springer-Verlag, Berlin, 1988), p. 251.

[24] R. Yano, M. Mitsunaga, and N. Uesugi, Phys. Rev. B **50**, 9031 (1994).

[25] Th. Schmidt, R. M. Macfarlane, and S. Völker, Phys. Rev. B **50**, 15707 (1994).

[26] Th. Schmidt, J. Baak, D. A. van de Straat, H. B. Brom, and S. Völker, Phys. Rev. Lett. **71**, 3031 (1993).

[27] Y. Mao, P. Gavrilovic, S. Singh, A. Bruce, and W. H. Grodkiewicz, Appl. Phys. Lett. **68**, 3677 (1996).

[28] K. Tanaka, T. Ohyagi, K. Hirao, and N. Soga, Bull. Chem. Soc. Jpn. **66**, 1121 (1993).

[29] S. Todoroki, K. Hirao, and N. Soga, J. Ceram. Soc. Jpn. **101**, 1065 (1993).

[30] K. K. Rebane and L. A. Rebane, in *Persistent spectral hole burning: science and application*, edited by W. Moerner (Springer-Verlag, Berlin, 1988), p. 17.

[31] M. M. Broer, B. Golding, W. H. Haemmerle, J. R. Simpson, and D. L. Huber, Phys. Rev. B **33**, 4160 (1986).

[32] K. Hirao and N. Soga, Yogyo-Kyokai-Shi **90**, 476 (1982).

[33] F. Durville, G. S. Dixon, and R. C. Powell, J. Lumin. **36**, 221 (1987).

[34] R. Wannemacher, J. M. A. Koedijk, and S. Völker, J. Lumin. **60-61**, 437 (1994).

[35] S. Hüfner, in *Optical Spectra of Transparent Rare Earth Compounds* (Academic, New York, 1978), p. 115.

[36] M. Tanaka and T. Kushida, Phys. Rev. B **52**, 4171 (1995).

[37] T. Suemoto, M. Namiki, and K. Koyama, Opt. Commun. **115**, 475 (1995).

[38] P. J. van der Zaag, B. C. Schokker, Th. Schmidt, and S. Völker, J. Lumin. **45**, 80 (1990).

[39] J. Hegarty and W. M. Yen, Phys. Rev. Lett. **43**, 1126 (1979).

[40] T. Okuno, K. Tanaka, K. Koyama, M. Namiki, and T. Suemoto, J. Lumin. **58**, 184 (1994).

[41] S. K. Lyo, Phys. Rev. Lett. **48**, 688 (1982).

[42] C. B. Layne, W. H. Lowdermilk, and M. J. Weber, Opt. Commun. **18**, 173 (1976).

[43] S. Tanabe, T. Ohyagi, N. Soga, and T. Hanada, Phys. Rev. B **46**, 3305 (1992).

[44] S. Tanabe, T. Ohyagi, S. Todoroki, T. Hanada, and N. Soga, J. Appl. Phys. **73**, 8451 (1993).

[45] S. Tanabe, T. Hanada, T. Ohyagi, and N. Soga, Phys. Rev. B **48**, 10591 (1993).

[46] S. Todoroki, K. Hirao, and N. Soga, J. Appl. Phys. **72**, 5853 (1992).

[47] H. Yugami, R. Yagi, S. Matsuo, and M. Ishigame, Phys. Rev. B **53**, 8283 (1996).

Chapter 4

Room-temperature persistent spectral hole burning of Eu^{3+} ions in glasses

4.1 High-temperature persistent spectral hole burning of rare-earth ions

As described in Chapter 3, persistent spectral hole-burning (PSHB) is an effective tool for performing high-resolution site-selective spectroscopy in solids in which the information of interest concerning the electronic and chemical structure of each site is extracted from the optically inhomogeneous linewidth. From a point of view of practical applications, frequency-domain optical-storage systems such as wavelength-multiplexed memories offer unique opportunities in the enhancement of optical-data density. Spectral holes can provide the frequency-selective multiple usage of a single spatial location to store information, thus introducing another dimension to the memory storage, that is, the frequency domain. Ideally, the improvement in storage density is given by the ratio Γ_{ih}/Γ_h, where Γ_{ih} is the inhomogeneous linewidth, and Γ_h is the homogeneous linewidth. In principle, this ratio can be as high as $10^6 \sim 10^7$ for the optical transitions of rare-earth ions in solids. Recently, successful demonstrations of the usage of spectral hole burning in frequency and time domain memory storage for rare-earth -doped crystals have renewed interest in developing materials suitable for memories and communication systems [1,2]. Also,

129

it was reported that moving images, as well as serial data bits, can be stored in one laser focal volume in a Y_2SiO_5:Eu^{3+} crystal by means of the holographic technique [3, 4].

On the other hand, there has been considerable effort devoted to developing materials that exhibit PSHB at higher temperatures. The occurrence of high-temperature hole burning is important for frequency-domain optical storage at $T >$77 K, which is of interest with regard to the obvious technological limitations connected with data storage at liquid-helium temperature. In addition, the possibility of burning stable holes at temperatures above 77 K permits measurements of the temperature dependence of a homogeneous linewidth over an extended temperature range and thus provides insight into the process which dominates optical dephasing in solids at higher temperatures. Hence, the search for new materials and new mechanisms for high-temperature PSHB is stimulated by the desire to broaden the breadth of the applicability of spectral hole burning as a powerful tool for high-resolution optical spectroscopy in solids as well as the need for materials with the properties required for frequency-domain optical storage.

The $^5D_0 - {}^7F_0$ transition of Eu^{3+} and its isoelectronic Sm^{2+} ions has a simple energy-level structure without degeneracy and usually shows a much narrow homogeneous linewidth compared with the inhomogeneous linewidth. Therefore, considerable attention has been focused on this transition of Eu^{3+} - and Sm^{2+} -doped materials from both fundamental and practical viewpoints [3–5]. Furthermore, glasses are considered to be more favorable as host materials for high-density optical memory devices than crystalline matrices because of its larger Γ_{ih}, and therefore higher Γ_{ih}/Γ_h. However, in order to realize the high-temperature hole-burning memory devices of glass materials, it is necessary to explore the conditions under which persistent spectral holes are burned at high temperatures. In Section 4.2, an attempt has been made to accomplish

high-temperature PSHB in Eu^{3+} -doped silicate glasses which usually exhibit the spectral hole burning only at very low temperatures.

4.2   High-temperature persistent spectral hole burning of Eu^{3+} ions in silicate glasses: new room-temperature hole-burning materials

4.2.1   Introduction

Considerable attention has been paid to persistent spectral hole burning (PSHB) of rare-earth -doped inorganic glasses since they are promising new materials for use in high-density optical memory devices. The problem for practical application, however, lies in the fact that PSHB of rare-earth ions in glasses is usually observed only at temperatures below 20 K. Recently, it was reported that Sm^{2+} in oxide and fluoride glasses shows PSHB due to photoionization of Sm^{2+} to Sm^{3+} at room temperature [6–9]. Also, recent hole-burning studies on Eu^{3+} -doped glasses revealed that the character of spectral hole burning can be controlled by the composition of the glass, by the melting atmosphere, or by the preparation of the glass. For instance, Eu^{3+} in a silicate glass usually manifested a transient hole due to optical pumping among nuclear quadrupole sublevels in the ground state only at very low temperatures below 4.2 K [10–13]. However, Eu^{3+} in sodium aluminosilicate glass ($50SiO_2 \cdot 25AlO_{3/2} \cdot 25NaO_{1/2} \cdot 1.0EuO_{3/2}$ in cation ratio) melted in air exhibited persistent holes between 4.2 and 20 K [14] as shown in Chapter 3. Furthermore, persistent holes were observed at temperatures more than 77 K for Eu^{3+} in aluminosilicate glass ($74.8SiO_2 \cdot 22.0Al_2O_3 \cdot 3.2Eu_2O_3$ in mol%) melted at 1950 °C in an inert-gas atmosphere [15] and in silica glass prepared by sol-gel method [16]. Thus, the conditions for formation of persistent holes in Eu^{3+} -doped glasses need to be examined from a viewpoint of development

of new PSHB materials which work at higher temperatures.

In the present chapter, the effect of the melting atmosphere on PSHB in Eu^{3+} -doped sodium silicate and aluminosilicate glasses is investigated, and successful observation of room-temperature PSHB in the glasses prepared under a nitrogen atmosphere is shown. In addition, a possible hole burning mechanism is discussed.

4.2.2 Experimental procedure

Glasses were prepared from reagent-grade Eu_2O_3, Na_2CO_3, Al_2O_3 and SiO_2 as starting materials. The prescribed compositions and the notations of the glasses are listed in Table 4.1. First, the raw materials were mixed thoroughly and the mixture was melted in air at 1500~1600 °C for 2 h in a platinum(80%)/rhodium(20%) crucible. Then the resultant Eu^{3+} -containing glass was remelted in a glassy carbon crucible under a nitrogen atmosphere at 1600 °C for 1 h using an electric furnace composed of a graphite heater, an insulator and a water jacket. The melt was cooled slowly to room temperature. The glass thus obtained was cut into a rectangular parallelepiped with dimensions of $10 \times 5 \times 5$ mm^3 and the glass surface was polished with CeO_2

Table 4.1: Glass composition used in this study (cation%). Each sample contains 1.0 cation% of $EuO_{3/2}$.

SiO_2	$AlO_{3/2}$	$NaO_{1/2}$	$\frac{Na_2O}{SiO_2+Na_2O}$	notation
50	25	25	–	SAN
75	0	25	0.14	SN14
48.2	0	51.8	0.35	SN35

slurry.

Fluorescence and excitation spectra were obtained with a spectrophotometer that used a Xe lamp as the light source (Hitachi 850). Spectral holes were burned into the $^5D_0 - {}^7F_0$ transition of Eu^{3+} by using a Rhodamine 6G dye laser (Spectra Physics 375B, linewidth ~ 1.3 cm^{-1}) pumped by an Ar^+ laser. A typical laser intensity during the burning was 10 W/cm^2, and the burning time ranged from 60 to 600 s. The hole was probed by means of fluorescence excitation spectroscopy by scanning the wavelength of laser beam whose power was attenuated by a factor of 200-300. Emission from the sample in the direction perpendicular to the exciting laser beam was dispersed using a monochromator equipped with a photomultiplyer (Hamamatsu Photonics R928) to select the $^5D_0 - {}^7F_2$ transition of Eu^{3+}. The sample was maintained at 77 to 300 K in a closed cycle helium-gas refrigerator (Iwatani CRT, 006-2000).

^{151}Eu Mössbauer effect measurements were carried out for the pulverized glass samples at room temperature to obtain information on the valence state of Eu. $^{151}Sm_2O_3$ with activity of 1.85 GBq was used as a 21.5 keV γ-ray source. The Mössbauer spectrum of EuF_3 was used as a standard for the isomer shift. The velocity calibration was done with the magnetic hyperfine spectrum of α-Fe obtained with a 14.4 keV γ-ray of ^{57}Co doped in rhodium.

4.2.3   Results

Figure 4.1(a) shows fluorescence spectrum at 12 K for SN14 glasses melted under a nitrogen atmosphere. Excitation was carried out at a wavelength of 465 nm, which corresponds to the $^5D_2 \leftarrow {}^7F_0$ transition of Eu^{3+}. Sharp peaks which originate from the $^5D_0 - {}^7F_J$ ($J = 0, 1, 2$) transitions of Eu^{3+} are observed in the range of 570 to 620 nm. Figure 4.1(b) shows excitation spectra of Eu^{3+} in SN14, SN35 and SAN glasses at 12 K. In this figure, the excitation
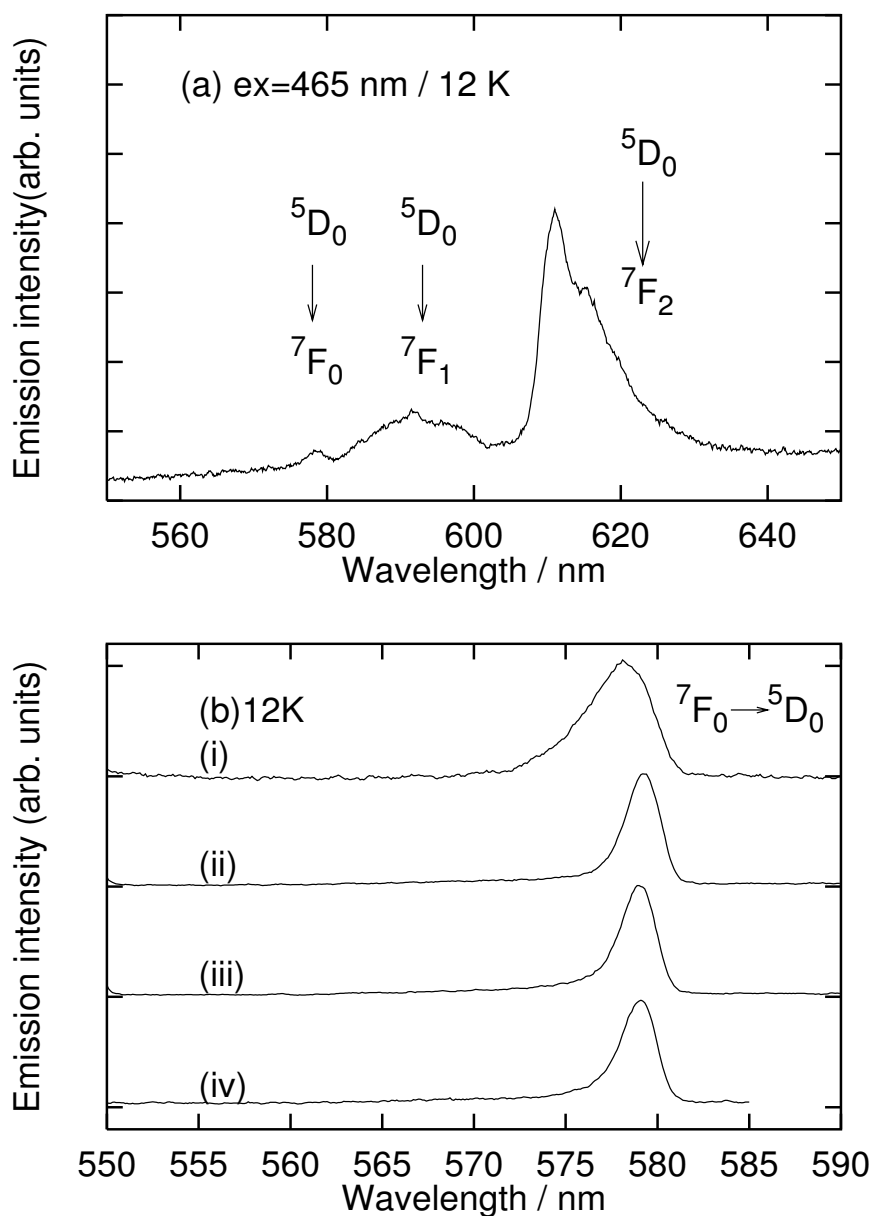
Figure 4.1: (a) Fluorescence spectrum at 12 K for SN14 glass melted under a nitrogen atmosphere. Excitation wavelength is 465 nm. (b) Excitation spectra at 12 K for Eu^{3+} in (i) SAN, (ii) SN35 and (iii) SN14 glasses melted under a nitrogen atmosphere. Curve (iv) is the excitation spectrum for Eu^{3+} in SN14 glass melted in air.

spectrum of Eu^{3+} in SN14 glass melted in air is also shown for comparison. The measurements were performed monitoring the fluorescence around 612.5 nm, which corresponds to the $^5D_0 - {}^7F_2$ transition of Eu^{3+}. A single peak due to the $^7F_0 \rightarrow {}^5D_0$ transition of Eu^{3+} is observed near 578 nm. The full width at half maximum of $^5D_0 - {}^7F_0$ transition was approximately estimated as 160 cm^{-1} for SAN glass, 80 cm^{-1} for SN14 glass and 75 cm^{-1} for SN35 glass. The inhomogeneous linewidth of the $^5D_0 - {}^7F_0$ transition is influenced by an addition of aluminum oxide, while the width is almost independent of Na_2O content. In addition, the excitation spectrum is not affected so significantly by melting atmosphere (see curves (iii)and (iv)).

Figure 4.2 shows Mössbauer spectra of SN14, SN35 and SAN glasses melted under a nitrogen atmosphere. In addition to the absorption peak that is due to Eu^{3+} ion near 0 mm/s, one that is due to Eu^{2+} appears near –13 mm/s in all the spectra. For the glass samples melted in air, on the other hand, no absorption peak that was due to Eu^{2+} was not detectable. The most common oxidation state of europium ion in ionic solids is the trivalent one with a $4f^6$ configuration. However, some amounts of trivalent europium ions in oxide glasses are readily reduced to the divalent state during melting under a nitrogen atmosphere [17]. Thus the result shown in Fig. 4.2 confirms that both Eu^{3+} and Eu^{2+} ions are present in all the samples. The fraction of absorption area of Eu^{3+} in the total absorption area was estimated to be about 50 % for SN14 glass, 50 % for SN35 glass and 20 % for SAN glass. As discussed in Chapter 1, the recoil-free fraction was considered to be smaller for Eu^{2+} than for Eu^{3+} in oxide glasses. Strictly speaking, therefore, the practical concentration of Eu^{3+} is slightly smaller than the value obtained from the fraction of absorption area. A close look at Fig. 4.2 shows that the linewidth of absorption peak of Eu^{2+} is broader than that for Eu^{3+}. This is caused by the hyperfine structure, manifesting that the spin-spin interactions among Eu^{2+} ions are
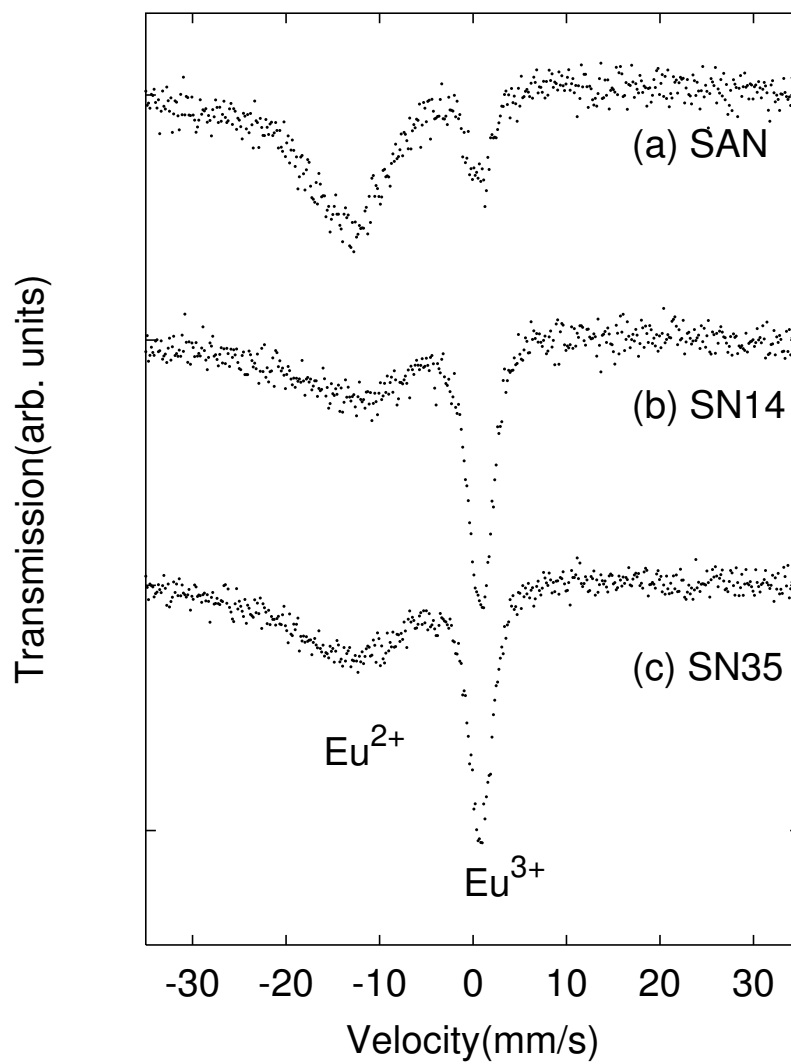
Figure 4.2: Mössbauer spectra of (a) SAN, (b) SN14 and (c) SN35 glasses melted under a nitrogen atmosphere at room temperature.

small [18]. In other words, Eu^{2+} ions are homogeneously distributed in these glasses.

Figures 4.3(a) and (b) show the excitation and difference spectra of Eu^{3+} in SAN glass melted under a nitrogen atmosphere before and after irradiation with a dye laser at 77 K, 180 K and room temperature, respectively. Holes are observed in all the spectra. As the temperature is raised, the hole width becomes broader and the depth shallower. In addition, the position of the hole varies when the wavelength of laser is changed (see Fig. 4.4(a)). The variation in hole linewidth with temperature above 77 K is probably dominated by a two-phonon Raman process. The width of the hole is about 3 cm^{-1} at 77 K and 20 cm^{-1} at 300 K. The ratio of the inhomogeneous linewidth (Γ_{ih}) to the homogeneous linewidth (Γ_h) is estimated to be nearly 100 at 77 K and 8 at 300 K under an assumption that the hole width is equal to twice the homogeneous linewidth. This value is a lower limit of Γ_{ih}/Γ_h due to the power broadening with respect to the hole linewidth. Laser linewidth also contributes to the hole width. At the present stage, the quality of our spectra is not good enough for accurate extrapolation to zero burn power. Hence, no attempt has been made to estimate temperature dependence of homogeneous linewidth. Figure 4.4(b) shows the burning-time dependence of hole depth of Eu^{3+} in the reduced aluminosilicate glass at 300 K. The increase in hole depth is rapid when the burning time is short but gradually slows down. The nonexponential dependence of hole depth on burning time is characteristic of persistent hole-burning phenomenon in glasses and clearly indicates that a distribution of hole-burning efficiency exists; Eu^{3+} ions for which holes are easily burned are the principal contributors to the hole spectrum.

Figure 4.5 shows excitation spectra for the $^5D_0 - {}^7F_0$ transition of Eu^{3+} in SN14 glasses melted under a nitrogen atmosphere before and after irradiation with a dye laser at 77 K, 130 K, 200 K and 300 K. The burning was performed
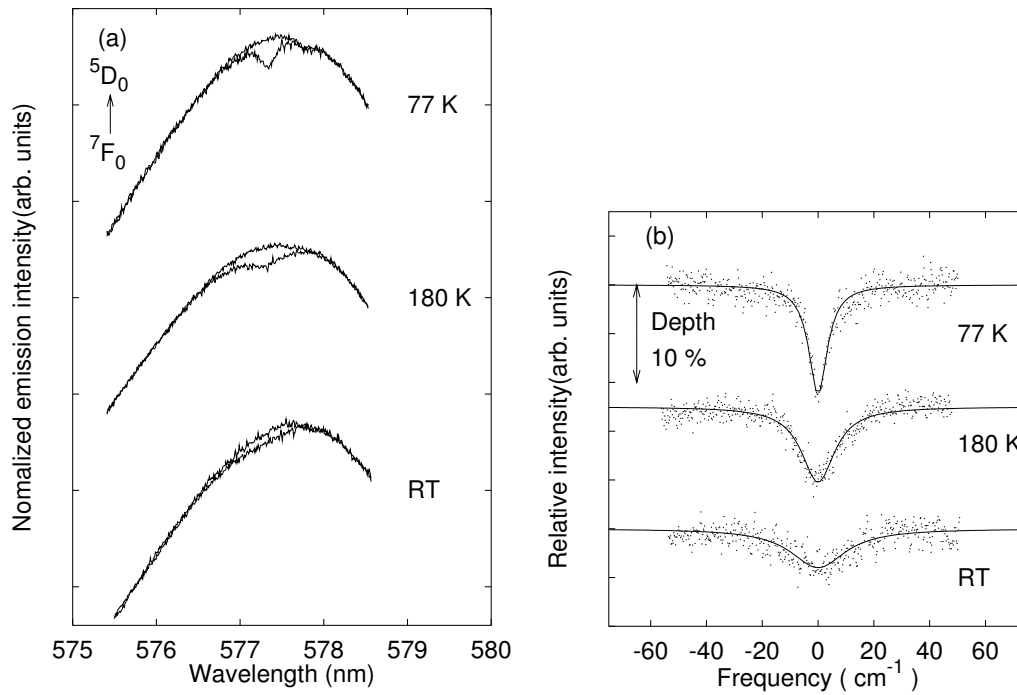
Figure 4.3: (a) Excitation and (b) difference spectra at 77 K, 180 K and room temperature for SAN glass melted under a nitrogen atmosphere before and after irradiation with a dye laser at 577.3 nm ($\sim$20 W/cm$^2\times$600 s). In Fig. 4.3(b), the solid curves represent Lorentzian functions fitted to the data points (dots).
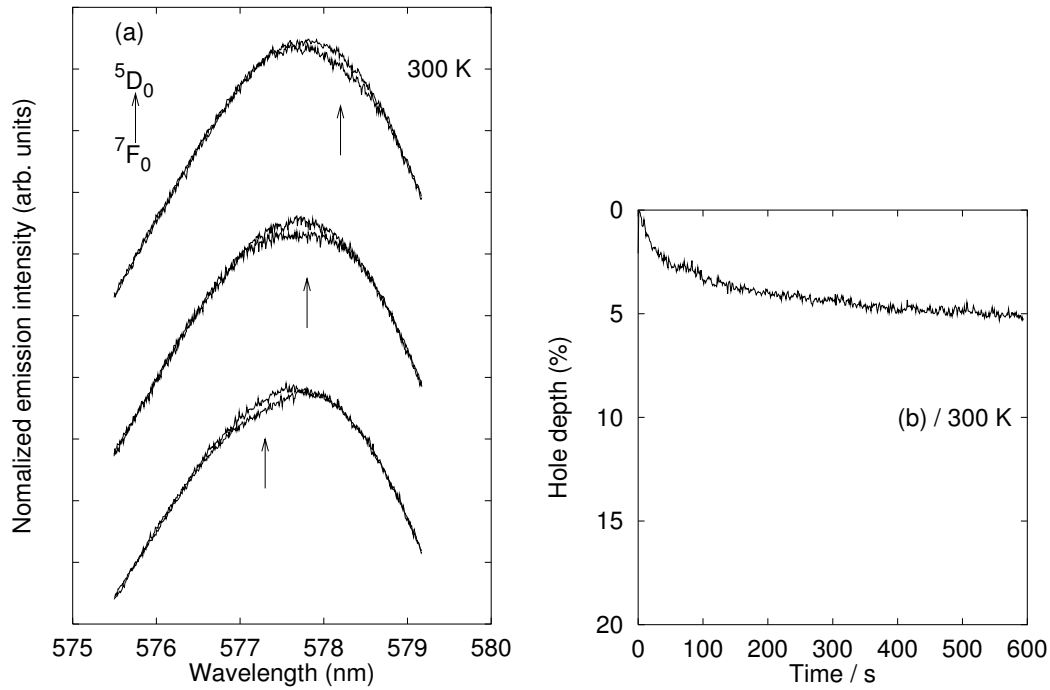
Figure 4.4: (a) Excitation spectra at room temperature for SAN glass melted under a nitrogen atmosphere before and after irradiation with a dye laser at 577.3, 577.8 and 578.2 nm ($\sim$20 W/cm$^2\times$600 s). The wavelength of laser is indicated by arrows in the figure. (b) Burning time dependence of hole depth at 300 K with laser irradiation at 577.3 nm obtained by monitoring $^5D_0$ – $^7F_2$ transition.
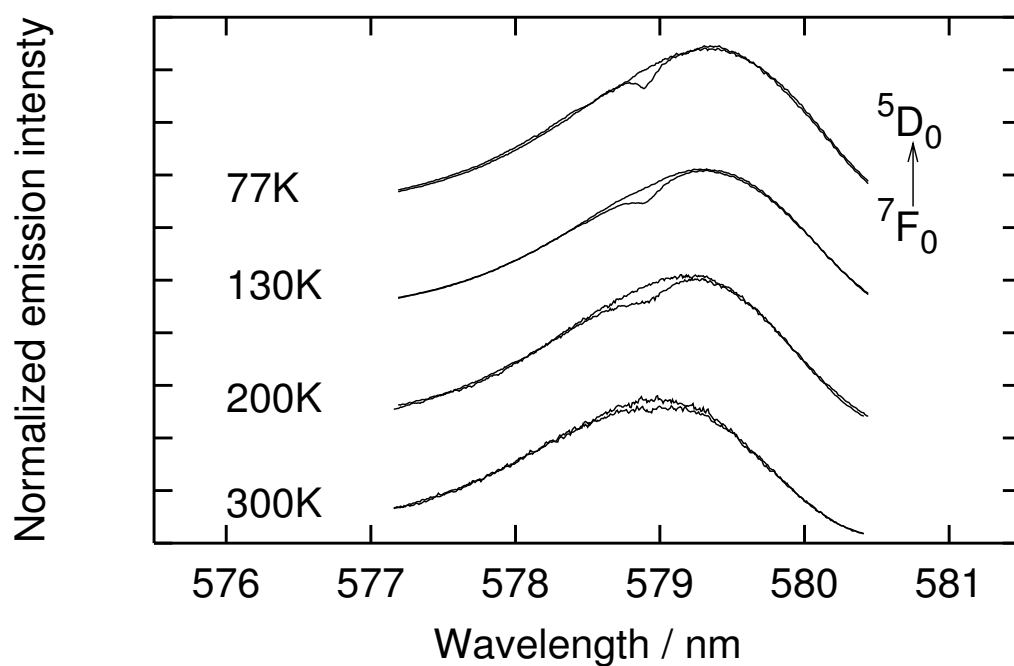
Figure 4.5: Excitation spectra at 77 K, 130 K, 200 K and room temperature for SN14 glass melted under a nitrogen atmosphere before and after irradiation with a dye laser at 579.4 nm under 10 W/cm^2×600s.
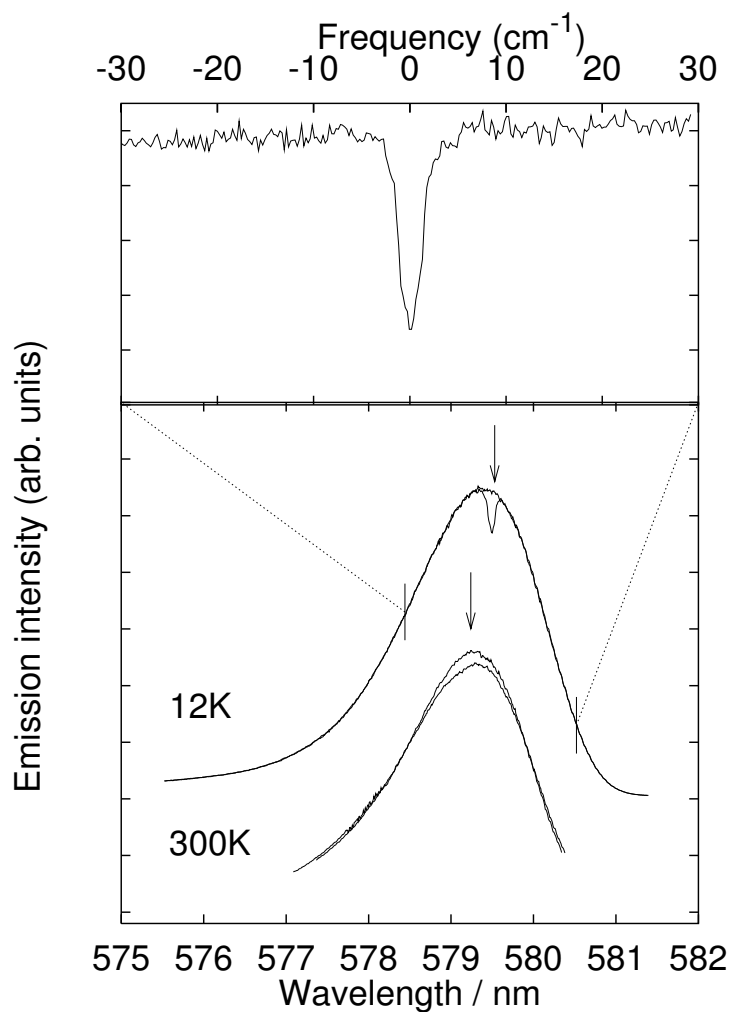
Figure 4.6: Bottom: Excitation spectra at 12 K and 300 K for SN35 glass before and after irradiation with a dye laser at 579.6 nm and 579.4 nm, respectively. Top: The difference signal between excitation spectra before and after buring at 12 K.

at a wavelength of 578.9 nm under 10 W/cm² irradiation for 600 s. A hole was burned at each of these temperatures. Figure 4.6 shows excitation spectra for SN35 glass obtained at 12 K and 300 K before and after hole burning. The burning condition is the same as in Fig. 4.5. The hole width is about 1.6 cm^{-1} at 12 K. The value is comparable to laser linewidth. Moreover, a broad and shallow hole is burned at 300 K at the burning wavelength denoted by the arrow.

Figure 4.7 shows hole spectra at 77 K for Eu^{3+} in SN14, SN35 and SAN glasses melted under a nitrogen atmosphere. The burning was performed at a wavelength of 579.4 nm under 10 W/cm² irradiation for 60 s. A single Lorenzian was approximately fitted to the hole spectrum. The hole width and

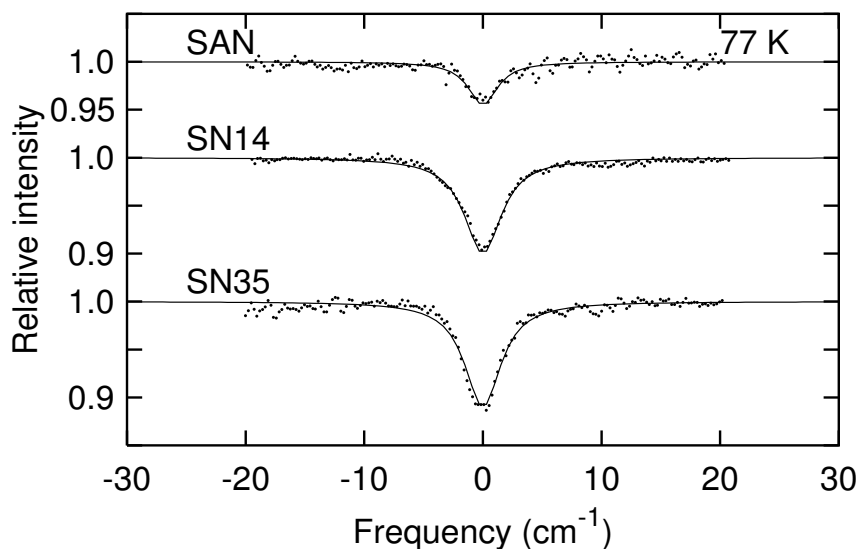
Figure 4.7: Hole spectra at 77 K for SAN, SN14 and SN35 glasses melted under a nitrogen atmosphere at 579.4 nm (10 W/cm²×60 s). The solid lines stand for Lorenzian functions fitted to the experimental data points (filled circles).
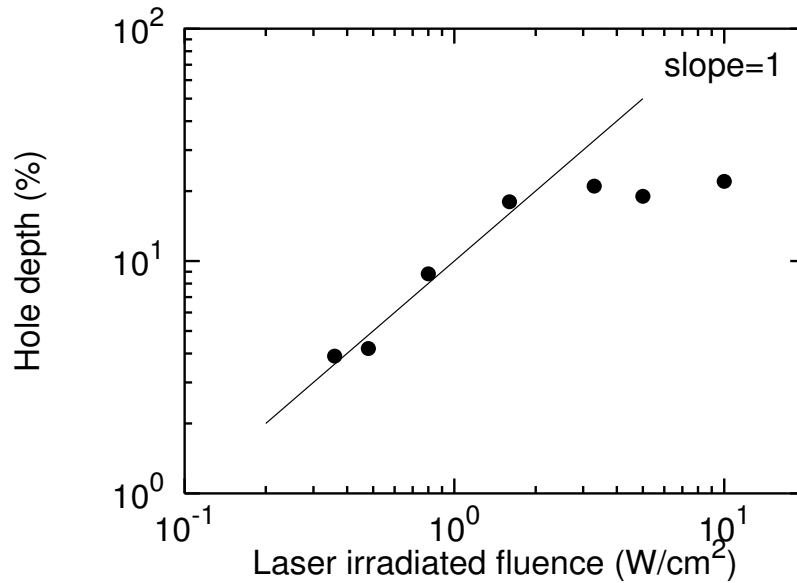
Figure 4.8: Laser fluence dependence of the hole depth at 579.4 nm for SN35 glass at 77 K. The burning time is 300 s. The slope of solid line is 1.0.

depth for SAN glass are about 3 cm^{-1} and 5 %, respectively. The hole width and depth for SN14 and SN35 glasses are nearly identical with each other, i.e., 4 cm^{-1} and 10 %, respectively. Thus the results mean that the hole-burning efficiency (width×depth) for SN14 glass is larger than that for SAN glass, while the efficiencies for SN14 and SN35 glasses are nearly the same as each other. For the SN35 glass, ∼3 % deep hole was easily burned after 1 s of irradiation at 579.4nm (20 W/cm^2) at 77 K.

Figure 4.8 shows the hole depth for SN35 glass as a function of laser fluence at 77 K. The laser-irradiation time is 300 s. The hole depth increases linearly with the burning intensity at the initial stage where shallow holes are burned.

4.2.4 Discussion

Hole-burning occurs when a frequency-selected subset of optical active ions is modified via a certain process, resulting in a change of the optical absorption spectrum. The spectral hole burning can take place through a variety of mechanisms; change of valence state due to photochemical process, modification of optical transition frequency through a change in the local structure, or population storage in the electronic excited state and/or in hyperfine levels of ground state. According to Macfarlane and Shelby [10], transient hole burning of Eu^{3+} -doped silicate glass occurs by an optical pumping mechanism which is due to a redistribution of population among nuclear quadrupole levels at low temperatures of $T < 4.2$ K. In addition, persistent holes were not burned at $T > 4.2$ K for the Eu^{3+} -doped silicate glass [10–14]. In fact, the hole burning experiments on SN14 glass prepared in air that had the same composition as reported here were carried out, and it was revealed that no persistent hole was burned even at low temperature like 4.2 K [14,19]. Therefore, the present experimental results indicate that the hole with room-temperature stability can be burned for Eu^{3+} in various silicate glasses prepared by only changing the melting atmosphere.

In Figure 4.9, curve(a) shows hole spectrum for SN35 glass obtained immediately after the hole burning. The burning of the hole was performed at 578.9 nm under 10 W/cm^2 irradiation for 600 s. Curve(b) is an excitation spectrum at 2 h after hole burning. It is evident that the hole lasts for 2 h. However, we observed erasure of hole with irradiation by an Ar^+ laser (514.5 nm, 10 $W/cm^2 \times 600$ s) after hole burning at 77 K. The green light was not utilized directly as an excitation light for the energy level of Eu^{3+} but corresponds to the absorption tail of the $4f^7 \rightarrow 4f^6 5d$ transition of Eu^{2+}. Curve(c) is a hole spectrum for SN35 glass burned with the same condition as in curve(a). Curve(d) is an excitation spectrum taken after burning with an Ar^+ laser.

The measurement was made with the Ar^+ laser at 514.5 nm overlapping the dye laser. The irradiation by Ar^+ laser at 514.5 nm after burning partially refills the previous hole. Further, the erasure of the hole is also caused partly by the formation of multiple holes within the inhomogeneous profile of the $^5D_0 - {}^7F_0$ transition of Eu^{3+}. Figure 4.10 shows the multiple hole spectra for SN35 glass under 10 W/cm^2 irradiation by the dye laser for 60 s at 77 K. It is obvious that the earlier holes are partially refilled when the later holes are burned. This is a one-photon erasure.

Holes with room-temperature stability for rare-earth -doped materials have been burned by photo-oxidation by means of two-photon or one-photon processes [6–9, 20–22]. For Eu^{3+} in solids it was reported that photoreduction of Eu^{3+} to Eu^{2+} via two-photon absorption occurred in $KBr:Eu^{3+}$ by irradiation of visible laser light with a wavelength of 455 to 475 nm [23]. Although the detailed mechanism of hole burning for Eu^{3+} ions in the present reduced glasses is unclear, a possible hole-burning mechanism can be depicted as follows. First the linear dependence of hole depth on the burning intensity suggests that the occurrence of hole in this glass system is not caused by a two-photon process observed by Yamada and Ohno [23] for Eu^{3+} -doped crystal, but by a single-photon process. The change only in the melting atmosphere produces some amounts of Eu^{2+} ions and leads to a persistent hole with high-temperature stability. Furthermore, erasure of the hole occurs by irradiation of Ar^+ laser light corresponding to the $4f^7 \rightarrow 4f^65d$ absorption tail of Eu^{2+} or by irradiation of a dye laser, which creates new holes in the excitation spectrum of the $^5D_0 - {}^7F_0$ transition of Eu^{3+}. All the experimental facts imply that non-photochemical processes are probably not important as the hole-burning mechanism. A plausible hole-burning mechanism is photoinduced reduction of Eu^{3+} to Eu^{2+} by means of a single-photon process; the released positive hole is trapped by Eu^{2+} which is originally present in the glass. The easy erasure

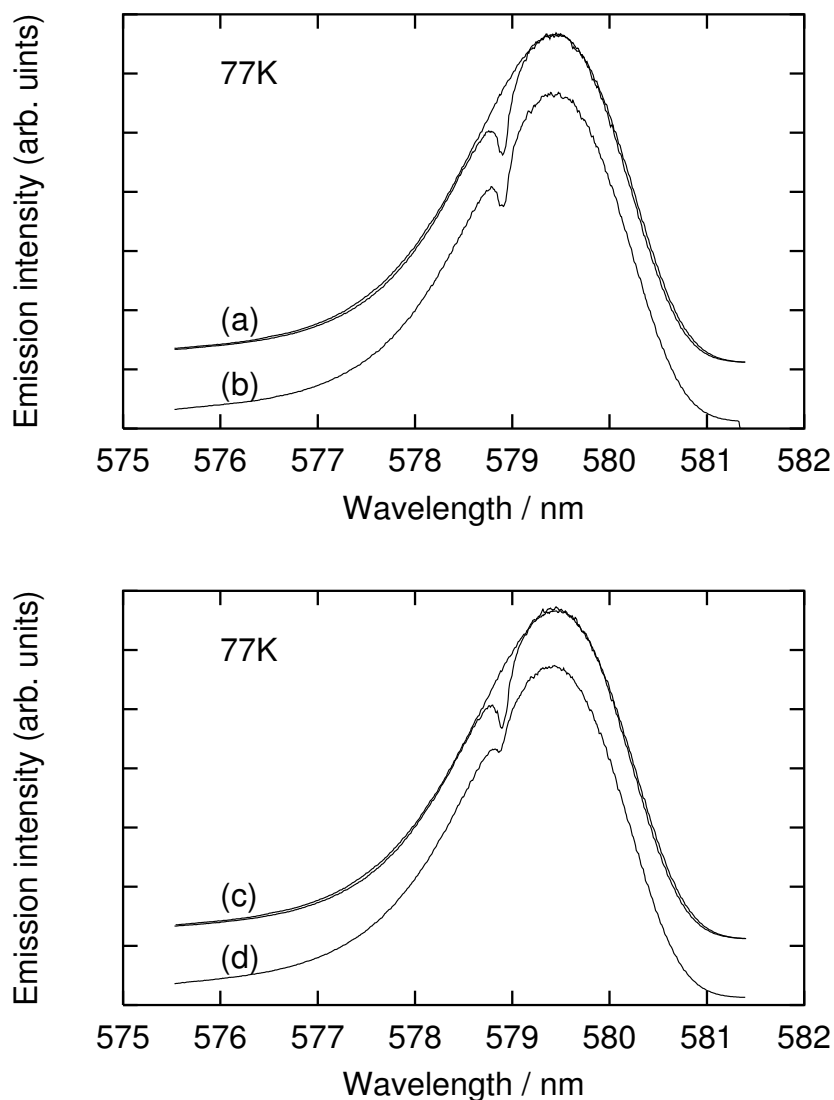Figure 4.9: (a) and (c) Excitation spectra for Eu^{3+} in SN35 glass melted under a nitrogen atmosphere before and after irradiation with a dye laser at 77 K. Excitation wavelength is 578.9 nm (10 W/cm^2×600 s). (b) Excitation spectrum at 2 h after burning. (d) Effect of irradiation with an Ar$^+$ laser light (514.5 nm) on excitation spectrum after burning. Curves (b) and (d) are shifted downward properly for clarity.
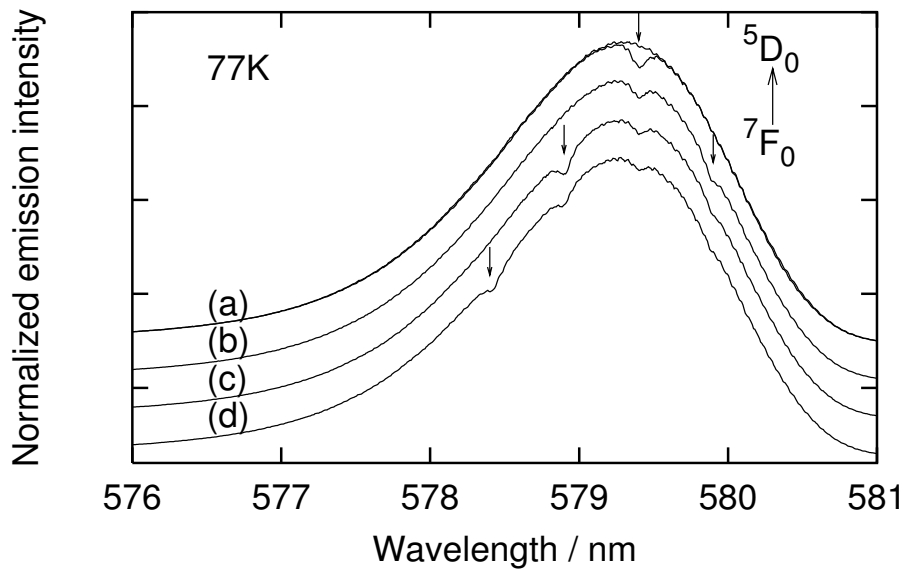
Figure 4.10: Multipule hole spectra at 77 K for the $^5D_0$ $-^7F_0$ transition of Eu^{3+} in SN35 glass melted under a nitrogen atmosphere under 10 W/cm^2×60 s. (a) Excitation spectra before and after burning at 579.4 nm. Curves of (b), (c) and (d) are excitation spectra after burning at 579.9 nm, 578.9 nm and 578.4 nm, respectively; these curves are shifted downward for clarity.

of the hole shown in Figs. 4.9 (curve(d)) and 4.10 presumably takes place as a result of the conversion of Eu^{2+} into Eu^{3+}; Eu^{2+} which traps the positive hole acts as an electron donor or a hole acceptor because Eu^{2+} is unstable in the glass.

It is well known that optical properties of trivalent rare-earth -doped glass is dominated more efficiently by the local structure than by the average structure of glass. This is so because rare-earth ions have a trivalent positive charge, and hence, they tend to be preferentially coordinated by non-bridging oxygens (NBO) rather than by bridging oxygens (BO) [24]. In sodium silicate

glass the amount of NBO increases with an increase in Na_2O content. In the present composition range, however, the NBO adjacent to Na^+ ions (NBO– Na^+) exist sufficient quantity even in SN14 glass, and Eu^{3+} ions can be preferentially coordinated by the NBO-Na^+, leading to absence of a large degree of dependence of the inhomogeneous linewidth of $^5D_0$ –$^7F_0$ transition on glass compositions as shown in Fig. 4.1(b). On the other hand, the introduction of Al_2O_3 into Eu^{3+} -doped sodium silicate glass largely modifies the local structure around Eu^{3+} [14, 24]. As the content of Al_2O_3 increases until the concentration ratio of Al_2O_3 to Na_2O is 1:1, NBO-Na^+, by which Eu^{3+} ions are coordinated, are gradually consumed to form Al-O-Si bridging oxide ions; the Al^{3+} ions form AlO_4^- and the negative charge of AlO_4 group is compensated by the Na^+ ion. This structural change is consistent with the fact that the inhomogeneous linewidth of the $^5D_0 - {}^7F_0$ transition is larger in sodium aluminosilicate glass than in sodium silicate glass, as shown in Fig. 4.1(b). That is, the local structure is rigid in sodium aluminosilicate glass because of the lack of NBO, so that Eu^{3+} ions must occupy a variety of sites, whereas the local structure is flexible in sodium silicate glasses owing to the presence of NBO, so that the NBO coordinate Eu^{3+} ions more readily and the site-to-site variation becomes small. In addition to the local structure around Eu^{3+} in sodium silicate and aluminosilicate glasses, a spatial distribution of Eu^{3+} and Eu^{2+} is found to be related to the hole-burning efficiency of Eu^{3+} as demonstrated in Fig. 4.7, because the hole burning probably takes place through photon-assisted tunneling to a local trap which we believe is predominantly an Eu^{2+} ion, as mentioned above. Whereas Eu^{3+} ions are preferentially coordinated by NBO-Na^+, divalent rare-earth ions such as Eu^{2+} are rather homogeneously distributed as a network modifying cation in oxide glasses [17, 18, 25, 26], evidence of which is provided by the observation of a broader spectrum in ^{151}Eu Mössbauer spectrum, i.e., the hyperfine structure of Eu^{2+} as seen from Fig. 4.2. In sodium

silicate glasses (SN14 and SN35), such a situation may bring about the existence of Eu^{3+} that is coordinated by NBO adjacent to Eu^{2+}, where the tunneling is highly probable. The resultant persistent hole burning would result in more efficient spatial redistribution of the europium ions between their electric charge states, Eu^{3+} and Eu^{2+}. Further experiments, however, are needed to clarify the hole-burning process completely.

4.2.5   Conclusion

A persistent spectral hole was burned into $^5D_0 - {}^7F_0$ transition of Eu^{3+} in various silicate glasses melted under a nitrogen atmosphere. The persistent hole was observed at 77 to 300 K and lasted for at least 2 h. An interesting characteristic of the hole burning in the present glass systems is the fact that the holes with high thermal stability are generated only by changes in the melting atmosphere. The hole-burning efficiency at 77 K is influenced by the composition of the glass; the hole area is much larger in sodium silicate glass than in sodium aluminosilicate glass, whereas the hole area almost remains constant with an increase in Na_2O content in sodium silicate glasses. As a mechanism of hole burning with room-temperature stability, photoinduced reduction of Eu^{3+} is proposed.

References

[1] H. Lin, T. Wang, and T. W. Mossberg, Opt. Lett. **20**, 1658 (1995).

[2] X. A. Shen, E. Chiang, and R. Kachru, Opt. Lett. **19**, 1246 (1994).

[3] M. Mitsunaga, N. Uesugi, H. Sasaki, and K. Karaki, Opt. Lett. **19**, 752 (1994).

[4] H. Sasaki, K. Karaki, M. Mitsunaga, and N. Uesugi, J. Lumin. **64**, 273 (1995).

[5] M. Tanaka and T. Kushida, Phys. Rev. B **52**, 4171 (1995).

[6] K. Hirao, S. Todoroki, and N. Soga, J. Lumin. **55**, 217 (1993).

[7] K. Hirao, S. Todoroki, D. H. Cho, and N. Soga, Opt. Lett. **18**, 1586 (1993).

[8] A. Kurita, T. Kushida, T. Izumitani, and M. Matsukawa, Opt. Lett. **19**, 314 (1994).

[9] M. Nogami, Y. Abe, K. Hirao, and D. H. Cho, Appl. Phys. Lett. **66**, 2952 (1995).

[10] R. M. Macfarlane and R. M. Shelby, Opt. Commun. **45**, 46 (1983).

[11] Th. Schmidt, R. M. Macfarlane, and S. Völker, Phys. Rev. B **50**, 15707 (1994).

[12] R. Wannemacher, J. M. A. Koedijk, and S. Völker, J. Lumin. **60-61**, 437 (1994).

[13] P. J. van der Zaag, B. C. Schokker, Th. Schmidt, and S. Völker, J. Lumin. **45**, 80 (1990).

[14] K. Fujita, K. Hirao, K. Tanaka, N. Soga, and H. Sasaki, J. Appl. Phys. **82**, 5114 (1997).

[15] Y. Mao, P. Gavrilovic, S. Singh, A. Bruce, and W. H. Grodkiewicz, Appl. Phys. Lett. **68**, 3677 (1996).

[16] M. Nogami and Y. Abe, Appl. Phys. Lett. **71**, 3465 (1997).

[17] K. Tanaka, T. Ohyagi, K. Hirao, and N. Soga, Bull. Chem. Soc. Jpn. **66**, 1121 (1993).

[18] M. Winterer, E. Morsen, B. D. Mosel, and W. Muller-Warmuth, J. Phys. C **20**, 5389 (1987).

[19] K. Fujita, K. Hirao, K. Tanaka, N. Soga, and H. Sasaki, Jpn. J. Appl. Phys. **37**, 2267 (1998).

[20] A. Winnacker, R. M. Shelby, and R. M. Macfarlane, Opt. Lett. **10**, 350 (1985).

[21] R. Jaaniso and H. Bill, Europhys. Lett. **16**, 569 (1991).

[22] D. M. Boey, R. M. Macfarlane, Y. Sun, and R. S. Meltzer, Phys. Rev. B **54**, 6263 (1996).

[23] Y. Yamada and S. Ohno, Chem. Lett., 465 (1991).

[24] S. Todoroki, K. Hirao, and N. Soga, J. Ceram. Soc. Jpn. **101**, 1065 (1993).

[25] K. Fujita, K. Tanaka, K. Hirao, and N. Soga, J. Appl. Phys. **81**, 924 (1997).

[26] K. Fujita, K. Tanaka, K. Hirao, and N. Soga, J. Am. Ceram. Soc. **81**, 1845 (1998).

Chapter 5

Magneto-optical properties of Eu^{2+} ions in glasses

5.1 Principle and application of Faraday effect

According to Maxwell's theory, light is composed of both right and left circularly polarized waves which are superposed and have the same frequency. The two waves travel at the same speed in a material in the absence of a magnetic field, thereby a net rotation of the plane of polarization being zero. When a magnetic field, H, is applied parallel to the light beam, the incident linearly polarized light emerges as elliptically polarized light with the major axis of the ellipse rotated through an angle θ as illustrated in Fig. 5.1. The presence of magnetic field brings about two resonance frequencies through a spin-orbital coupling, and these frequencies correspond to right and left circularly polarized light. The difference in real index of refraction for these frequencies $\Delta n = n_r - n_l$ gives rise to the Faraday rotation,

$$\theta = \omega(l/2c)\Delta n, \tag{5.1}$$

where l is the sample thickness, c is the velocity of light, and ω is the angular frequency of light. The difference in absorption coefficients is the circular dichroism and leads to the ellipticity.

In 1845, Faraday has observed that a glass specimen placed in a magnetic field becomes optically active, i.e., the plane of polarization of a light beam
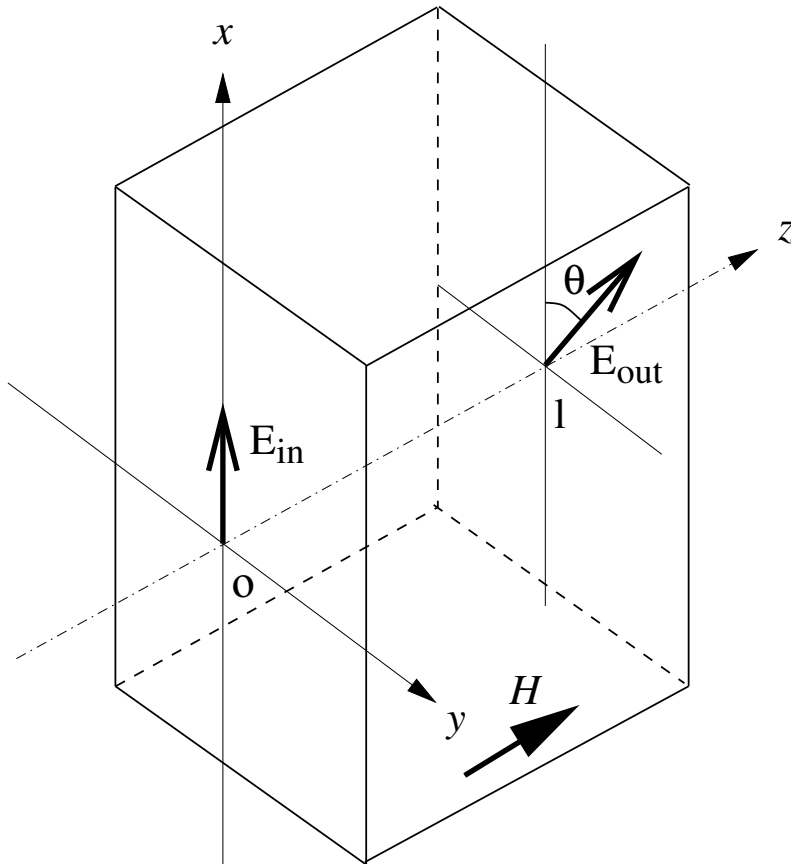
Figure 5.1: Schematic illustration of Faraday rotation. The magnetic field, H, is imposed on a material of sample thickness, l. Here, the magnetic field and the direction of propagation of the light are taken along the positive z axis. When the angle of rotation, θ, is clockwise (positive angle), as light propagates away from the viewer in the direction of magnetic field, the rotation is caused by a diamagnetic transition. If the rotation is in the opposite direction (negative angle), then it is a paramagnetic rotation.

Polarizer Faraday rotator Polarizer
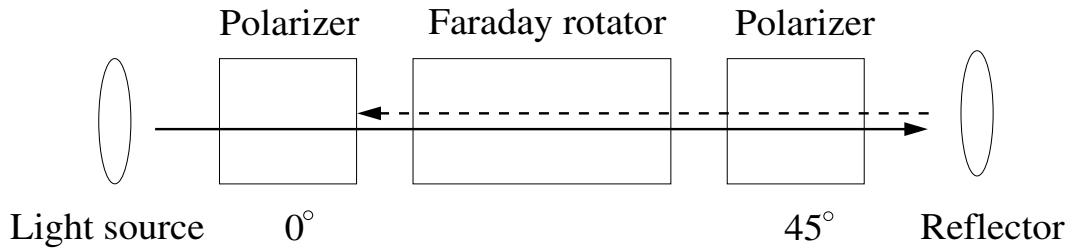
Light source 0° 45° Reflector

Figure 5.2: Schematic illustration of light isolator.

transmitted through a glass object is rotated. Since the discovery of the Faraday effect, several interesting devices have been fabricated, including optical isolators, optical modulators, sensors of electric current, sensors of magnetic field and so forth. In particular, the optical isolators are commonly used in advanced optical systems. A typical light isolator is presented in Fig. 5.2. The two polarizers are oriented at 45° to each other and placed on both sides of a Faraday rotator. An incident light beam is polarized by the first polarizer and passes through the Faraday rotator. The plane of polarization is then rotated 45°. The light transmitted successfully passes through the second polarizer. However, the light reflected back toward the rotator is blocked at the first polarizer because the plane of polarization is rotated an additional 45° such that the plane is 90° to the orientation of the first polarizer. Consequently, the light isolator is utilized in optics systems to prevent backward reflection of light.

5.1.1 Faraday effect of rare-earth ions in glasses

It is well known that single-crystalline ferrites with garnet structure such as $Y_3Fe_5O_{12}$ [1] and $Gd_2BiFe_5O_{12}$ [2] exhibit extremely large Faraday effects. In addition to the large magnetization, the optical absorbance is low in the infrared range. Therefore, they have very large magneto-optical figures of

merit (this parameter is defined as the Faraday rotation angle divided by the absorbance), leading to their practical applications at the wavelength of 1.3 or 1.5 μm for optical communication. However, the magneto-optical figures of merit become low in the visible range because of the high optical absorbance. Namely, the practical use of the ferrite crystals is limited to the infrared range. Candidates for promising materials which work well in the visible region are rare-earth -containing inorganic glasses.

Many studies have been carried out regarding the Faraday effect of rare-earth -containing oxide, fluoride and oxyfluoride glasses so far [3–13]. Nowadays, it is well known that Ce^{3+}, Pr^{3+}, Tb^{3+}, Dy^{3+} and Eu^{2+} bring about large Faraday effects in the visible range. The mechanism of Faraday effect in these glasses was analyzed in terms of a theory established by Van Vleck and Hebb [14], and it was revealed that the $4f^n \rightarrow 4f^{n-1}5d$ transition of rare-earth ions leads to the Faraday effect [3, 4]. In particular, the glasses containing a large amount of Eu^{2+} ions show rather large Faraday effects in the visible range compared with the glasses containing trivalent rare-earth ions, as first demonstrated by Shafer and Suits [10]. They ascribed the large Faraday rotation angle of Eu^{2+} -containing aluminoborate glasses to the long effective wavelength of $4f^7 \rightarrow 4f^65d$ transition as well as the large magnetic moment of Eu^{2+}. In Section 5.2, the relationship between local structure and Faraday effect of oxide glasses containing a large amount of Eu^{2+} ions is clarified in order to design magneto-optical materials which work effectively in the visible range.

5.2 Local structure and Faraday effect of oxide glasses containing Eu^{2+} ions

5.2.1 Introduction

There are many applications of glass materials which contain rare-earth ions utilizing their forced electric dipole $4f^n \to 4f^n$ transitions; for example, laser glasses, fiber amplifiers, upconversion glasses, and so on. Besides the $4f^n \to 4f^n$ transitions, the allowed electric dipole transitions between $4f^n$ and $4f^{n-1}5d$ states manifest interesting optical and magneto-optical properties. Recently, photostimulated luminescence has been observed for X-ray irradiated glasses codoped with Eu^{2+} and Sm^{3+} ions [15]. When the X-ray irradiated glasses are stimulated by a He-Ne laser (632nm), intense emission is observed at the wavelength corresponding to the $4f^65d - 4f^7$ transition of Eu^{2+}. Consequently, the glasses become promising materials for a two-dimensional X-ray imaging sensor.

Another interesting phenomenon relevant to $4f^n \to 4f^{n-1}5d$ is Faraday effect, which generally occurs by the orientation of ensembles of magnetic dipoles induced by an external magnetic field. The glasses containing a large amount of rare-earth ions such as Ce^{3+}, Pr^{3+}, Tb^{3+} and Eu^{2+} exhibit large Faraday effects in the visible to ultraviolet range. However, the study of the Faraday effect of Eu^{2+} ions in glasses is limited in a few cases in contrast to the Faraday effect of trivalent rare-earth ions. One reason for this may come from the difficulty in converting Eu^{3+} into Eu^{2+} ions. For a comprehensive understanding of the Faraday effect of Eu^{2+} in oxide glasses, knowledge of the electronic structure of Eu^{2+} is required, since the outer $5d$ level is influenced to a much greater extent by the ligand field of the ion than the $4f$ level shielded by outer orbitals. As described in Chapter 1, ^{151}Eu Mössbauer effect measurements were carried

out for sodium borate and alkali silicate glasses containing a large amount of Eu^{2+} ions to examine the chemical and electronic structure of Eu^{2+}. In the present investigation, the dependence of Faraday rotation angle on the glass compositions for these glasses is measured, and the relationship between local structure and Faraday effect of Eu^{2+} is discussed. In addition, the magneto-optical figure of merit, which is an important factor from a practical viewpoint, is estimated in the wavelength range of 550 to 800 nm.

5.2.2   Experimental procedure

Glasses were prepared from reagent-grade Eu_2O_3, Li_2CO_3, Na_2CO_3, K_2CO_3, B_2O_3, Al_2O_3 and SiO_2 as starting materials. The prescribed compositions and their notations were the same as listed in Table 1.2. The glass was cut into a plate and the both surfaces were polished. The sample thickness was determined using a micrometer. The Faraday rotation angle was measured at room temperature using a commercial system for the Faraday and Kerr effects (JASCO, Model K-250). The light source was a Xe lamp. The wavelength was varied from 850 to 350 nm. The external magnetic field was fixed to be 15 kOe. Optical absorption spectra were measured at room temperature using a spectrophotometer (Hitachi 330). Density of the glass samples was measured by means of the Archimedes' method with kerosene as the immersion liquid to calculate the number density of Eu^{2+} ions incorporated into each of the glass samples. The isomer shift evaluated from ^{151}Eu Mössbauer spectroscopy was the same value as in Table 1.3.

5.2.3   Results

The paramegnetic Faraday rotation angle, θ, is expressed by

$$\theta = VHl, \tag{5.2}$$

where V is the Verdet constant, H is the external magnetic field and l is the optical path length in the sample. The wavelength dependence of Verdet constant is shown for xEuO$\cdot$($100 - x$)(0.1Na$_2$O$\cdot0.9$B$_2$O$_3$) glasses with $x = 10, 15, 20$ mol% in Fig. 5.3. The Verdet constant manifests negative values over the wavelength region between 400 and 850 nm. The magnitude of Verdet constant increases with a decrease in the wavelength. This tendency is the same as observed for other glasses containing rare-earth ions. The Verdet constants of sodium borate and alkali silicate glasses at a wavelength of 600 nm obtained from Eq. (5.2) are summarized in Table 5.1. It should be noted that the practical concentration of EuO in alkali silicate glasses is less than a nominal concentration as shown in Table 1.3. Nonetheless, the magnitude of Verdet constant of alkali silicate glasses is larger compared with the value of sodium
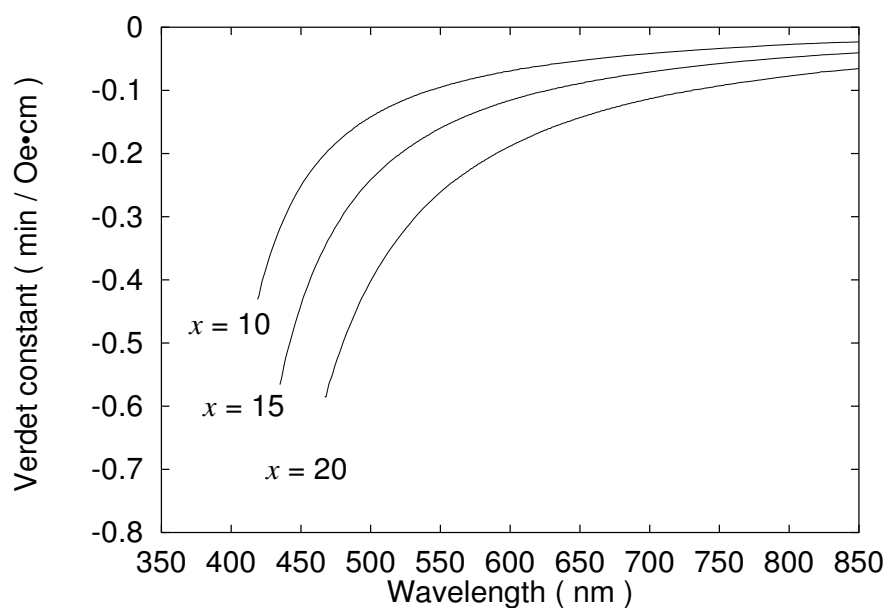

Figure 5.3: Wavelength dependence of Verdet constant for xEuO$\cdot$($100 - x$)(0.1Na$_2$O$\cdot0.9$B$_2$O$_3$) glasses with $x = 10, 15, 20$ mol%.

Table 5.1: Verdet constant, V, of sodium borate and alkali silicate glasses containing Eu^{2+} ions at a wavelength of 600 nm. The Verdet constants of other glasses containing rare-earth ions are also shown for comparison [3, 4, 10]

Notation	Glass composition (mol%)	Verdet constant (min/Oe·cm)
90BN15E	$15EuO·85(0.10Na_2O·0.90B_2O_3)$	-0.115
70BN15E	$15EuO·85(0.30Na_2O·0.70B_2O_3)$	-0.200
90BN20E	$20EuO·80(0.10Na_2O·0.90B_2O_3)$	-0.188
75B25E	$25EuO·75B_2O_3$	-0.279
70B30E	$30EuO·70B_2O_3$	-0.363
78SN10E	$10EuO·90(0.22Na_2O·0.78SiO_2)$	-0.177
78SN16E	$16.2EuO·83.8(0.22Na_2O·0.78SiO_2)$	-0.305
78SN20E	$20EuO·80(0.22Na_2O·0.78SiO_2)$	-0.350
78SN30E	$30EuO·70(0.22Na_2O·0.78SiO_2)$	-0.569
78SL20E	$20EuO·80(0.22Li_2O·0.78SiO_2)$	-0.332
78SK20E	$20EuO·80(0.22K_2O·0.78SiO_2)$	-0.234
67SAN20E	$20EuO·80(0.22Na_2O·0.11Al_2O_3·0.67SiO_2)$	-0.303
56SAN20E	$20EuO·80(0.22Na_2O·0.22Al_2O_3·0.56SiO_2)$	-0.241
	$34.2EuO·14.8Al_2O_3·50.7B_2O_3$ [a]	-0.478
	$25.4Tb_2O_3·74.6P_2O_5$ [b]	-0.206
	$28.5Dy_2O_3·71.5P_2O_5$ [b]	-0.217
	$14.3Tb_2O_3·14.3Pr_2O_3·71.4B_2O_3$ [c]	-0.348
	$15.1Dy_2O_3·15.1Pr_2O_3·69.8B_2O_3$ [c]	-0.332

[a] Cited from Ref. [10]. The practical concentration of Eu^{2+} is 30.5 mol%.

[b] Cited from Ref. [4].

[c] Cited from Ref. [3].

Table 5.2: Density, d, and number of Eu^{2+} ions per unit volume, N, for some of sodium borate and alkali silicate glasses.

Notation	$d\,(\,\mathrm{g/cm^3}\,)$	$N\,(\,10^{21}\mathrm{cm^{-3}}\,)$
90BN15E	2.83	3.1
70BN15E	3.10	3.4
90BN20E	3.10	4.2
78SN10E	2.85	2.0
78SN16E	3.22	3.3
78SN20E	3.94	4.9
78SN30E	4.14	6.4
78SL20E	3.66	4.7
78SK20E	3.47	3.4
67SAN20E	3.50	4.2
56SAN20E	3.45	4.1

borate glasses when the nominal concentration of EuO remains constant.

Table 5.2 shows the density for some of sodium borate and alkali silicate glasses. This table also shows the number of Eu^{2+} ions per unit volume estimated from the density, composition of the glass, and fraction of Eu^{2+} ions in the total number of europium ions (see Table 1.3).

5.2.4   Discussion

According to a theory derived by Van Vleck and Hebb [14] for the Faraday effect of paramagnets, the Verdet constant is given by

$$V = (4\pi^2\nu^2\chi/g\mu_B ch)\sum_{i,j}C_{ij}(\nu^2 - \nu_{ij}^2)^{-1}, \tag{5.3}$$

where ν is the frequency of the light, χ is the magnetic susceptibility , g is the Landé factor, μ_B is the Bohr magneton, c is the velocity of light, h is the Planck constant, ν_{ij} is the transition frequency and C_{ij} is a parameter related to the transition probability. The subscript i and j represent all the quantum numbers except the magnetic quantum number of the ground and excited states. Eq. (5.3) can be expressed approximately as follows:

$$V^{-1} = \frac{g\mu_B ch}{4\pi^2\chi C_t}\left(1 - \frac{\lambda^2}{\lambda_t^2}\right), \tag{5.4}$$

where λ is the wavelength of the incident light, C_t is the effective transition probability and λ_t is the effective transition wavelength. The magnetic susceptibility in Eqs. (5.3) and (5.4) is expressed by the following relation:

$$\chi = \frac{Np_{eff}^2\mu_B^2}{3\mu_0 k(T - \theta_P)}, \tag{5.5}$$

where θ_P is the paramagnetic Curie temperature, N is the number of magnetic ions per unit volume, p_{eff} is the effective number of Bohr magneton, μ_B is the Bohr magneton, μ_0 is the magnetic permeability of vacuum, k is the Boltzmann constant and T is the temperature. The paramagnetic Curie temperature of oxide and fluoride glasses containing rare-earth ions is much lower than the room temperature. For instance, Schoenes *et al.* [11] measured the temperature dependence of magnetic susceptibility for silicate glass with $Eu_{0.12}^{2+}Eu_{0.02}^{3+}Si_{0.31}O_{0.55}$ composition, and revealed that the paramagnetic Curie temperature of the glass is 1 K or so. This fact indicates that superexchange

interaction among rare-earth ions is very small due to the shielding effect of outer electrons on the $4f$ electrons. Hence, it is reasonably assumed that $\theta_P = 0$ for the oxide glasses containing Eu^{2+} ions. Thus, the magnetic susceptibility, χ, at room temperature can be calculated from the number density of Eu^{2+} ions, N in Table 5.2 by using Eq. (5.5).

Figures 5.4 and 5.5 show the relationship between V^{-1} and λ^2 for 15EuO·85 $\{x\mathrm{Na_2O}\cdot(1-x)\,\mathrm{B_2O_3}\}$ glasses with $x = 0.1$, 0.2 and 0.3 and $x\mathrm{EuO}\cdot(100-x)(0.22\mathrm{Na_2O}\cdot0.78\mathrm{SiO_2})$ glasses with $x = 10$, 16.2, 20 and 30 mol%, respectively. The linear relationship is observed for all the glass samples as expected from Eq. (5.4). In other words, the Faraday effect of the present glasses can be interpreted based on the Van Vleck-Hebb theory. From the intercept be-
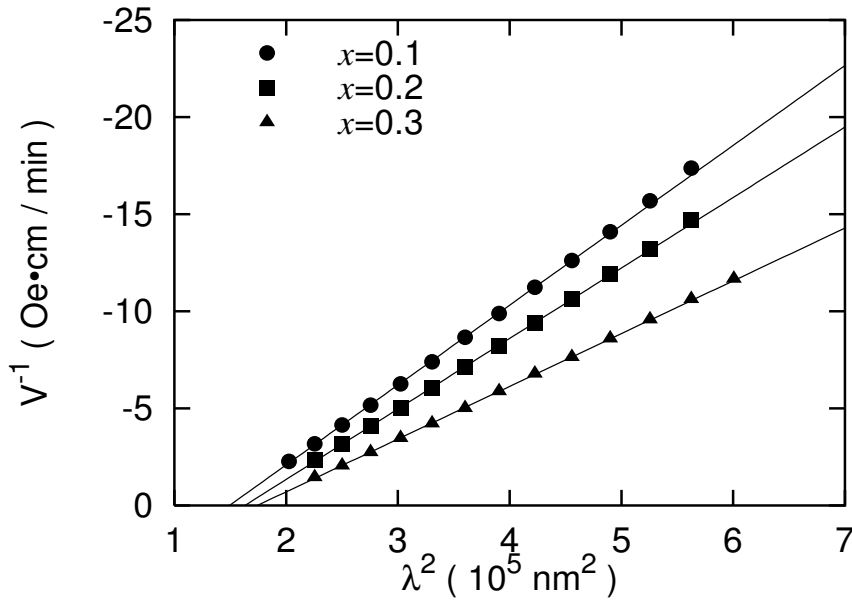

Figure 5.4: Relation between inverse Verdet constant and square of wavelength for 15EuO·85$\{x\mathrm{Na_2O}\cdot(1-x)\,\mathrm{B_2O_3}\}$ glasses with $x = 0.1$, 0.2 and 0.3. The solid lines were drawn by using the least squares method.
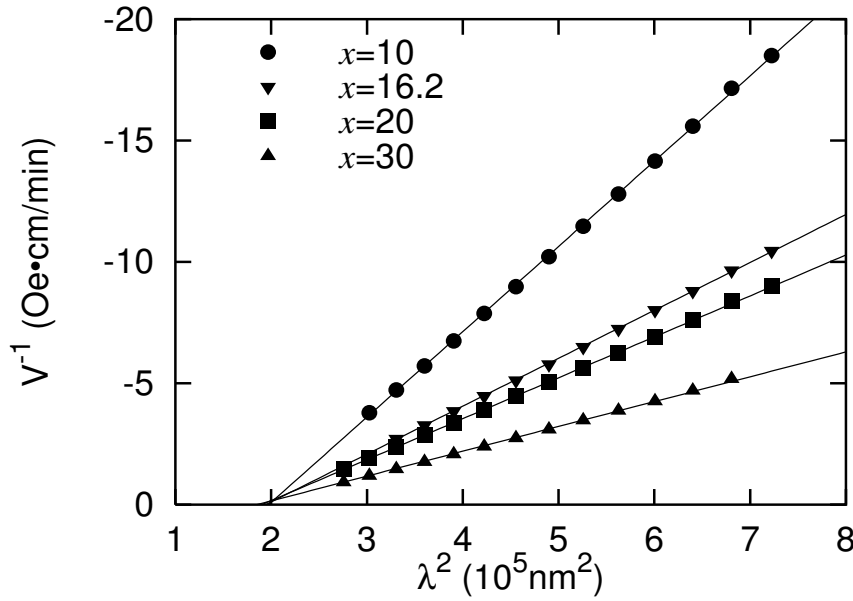
Figure 5.5: Relation between inverse Verdet constant and square of wavelength for xEuO·$(100 - x)(0.22\text{Na}_2\text{O}\cdot0.78\text{SiO}_2)$ glasses with $x = 10$, 16.2, 20 and 30 mol%. The solid lines were drawn by using the least squares method.

tween the straight line and the abscissa, the effective transition wavelength, λ_t, was evaluated. Furthermore, the effective transition probability, C_t, was estimated from the slope of the line by using Eqs. (5.4) and (5.5). Here, the presence of Eu^{3+} ions was ignored because the paramagnetic Faraday effect of Eu^{3+} ions is small in the visible range [3, 4]. For instance, the Verdet constants for $\text{Eu}(\text{PO}_3)_3$ compound were reported to be –0.006 min/Oe·cm and –0.003 min/Oe·cm at 500 and 600 nm, respectively [4]. The results of the analyses are summarized in Table 5.3. Both λ_t and C_t of the alkali silicate glasses are larger than those of the sodium borate glasses. As easily found from Eq. (5.4), for a given λ, where $\lambda > \lambda_t$, the magnitude of Verdet constant, i.e., $|V|$ increases with an increase in λ_t and C_t. Hence, the large λ_t and C_t

Table 5.3: Effective transition wavelength, λ_t, and effective transition probability, C_t, for some of sodium botrate and alkali silicate glasses.

Notation	λ_t (nm)	C_t (10^{-45}J·cm³)
90BN15E	386	3.2
70BN15E	417	3.8
90BN20E	388	3.5
78SN10E	444	4.4
78SN16E	441	4.8
78SN20E	437	3.8
78SN30E	430	5.0
78SL20E	432	4.3
78SK20E	438	4.1
67SAN20E	434	4.0
56SAN20E	414	3.9

lead to the large magnitude of Verdet constant of the alkali silicate glasses. The magnitude of Verdet constant of 78SN30E glass is 0.569 mm/Oe·cm at a wavelength of 600 nm as shown in Table 5.1. This value is the largest among the glasses containing rare-earth ions reported so far.

The variation of effective transition wavelength with glass composition is connected with the change of average electron density of oxide ions around an Eu^{2+} ion since the energy levels of $5d$ orbitals are significantly affected by the crystal field around the Eu^{2+} ion. Figure 5.6 shows the relationship between the inverse effective transition wavelength and the isomer shift evaluated from ^{151}Eu Mössbauer spectroscopy. As revealed by Eq. (1.3), the isomer shift approximately reflects $6s$ electron density at the Eu^{2+} ion site, and the
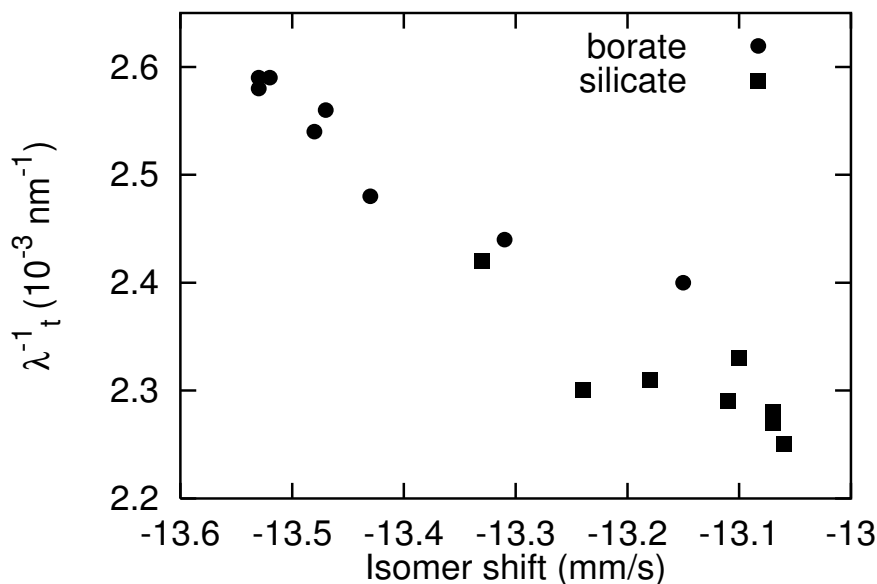

Figure 5.6: Relationship between inverse effective transition wavelength, λ_t^{-1}, and isomer shift deduced from Mössbauer spectra for sodium borate and alkali silicate glasses containing Eu^{2+} ions.

$4f^6 5d$

$4f^7({}^8S_{7/2})$

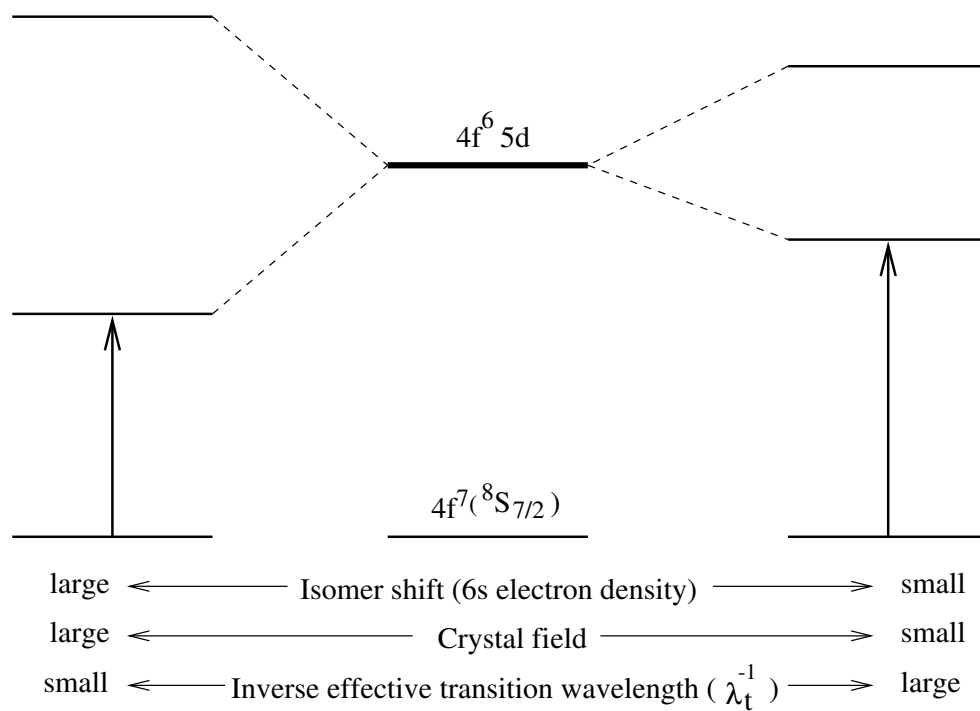| large | $\longleftarrow$ Isomer shift (6s electron density) $\longrightarrow$ | small |
| large | $\longleftarrow$ Crystal field $\longrightarrow$ | small |
| small | $\longleftarrow$ Inverse effective transition wavelength (λ_t^{-1}) $\longrightarrow$ | large |

Figure 5.7: Schematic illustration of the relationship between inverse effective transition wavelength and isomer shift.

isomer shift increases as the $6s$ electron density increases because the nuclear radius of the excited state minus that of the ground state is positive. As shown in Fig. 5.6, the effective transition wavelength correlates with the isomer shift. Since the increase in the isomer shift reflects an increase in the electron-donation power of oxide ions surrounding an Eu^{2+} ion, the large value of isomer shift results in a large splitting of $5d$ levels of an Eu^{2+} ion according to the crystal field theory. Consequently, the effective transition wavelength which corresponds to the transition from the $4f^7$ ground state ($^8S_{7/2}$) to the lowest $5d$ level increases with an increase in the isomer shift irrespective of the glass composition. This situation is presented in Fig. 5.7.

From a point of view of practical applications, the magneto-optical figure of merit defined as θ/α, where θ is the Faraday rotation angle and α is the absorbance, is an important factor. Figure 5.8 shows optical absorption
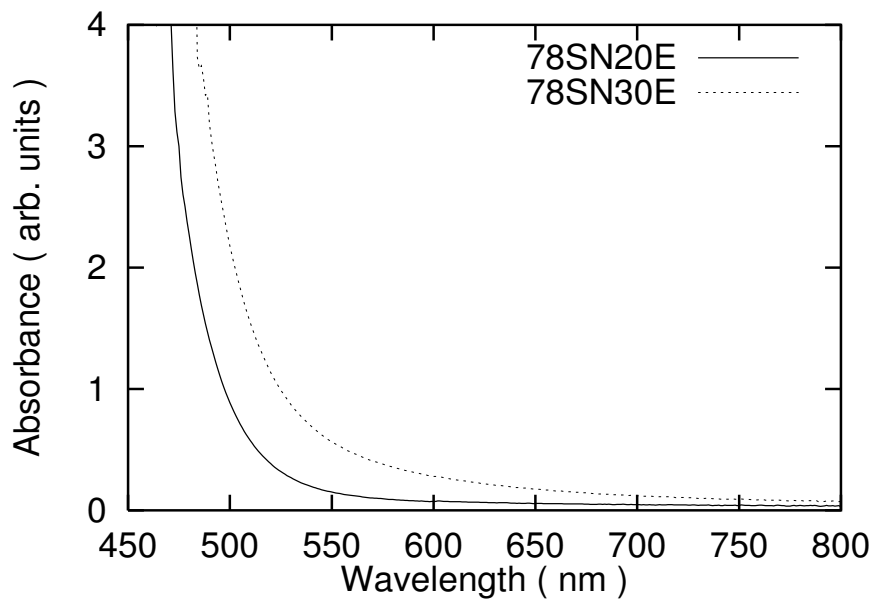

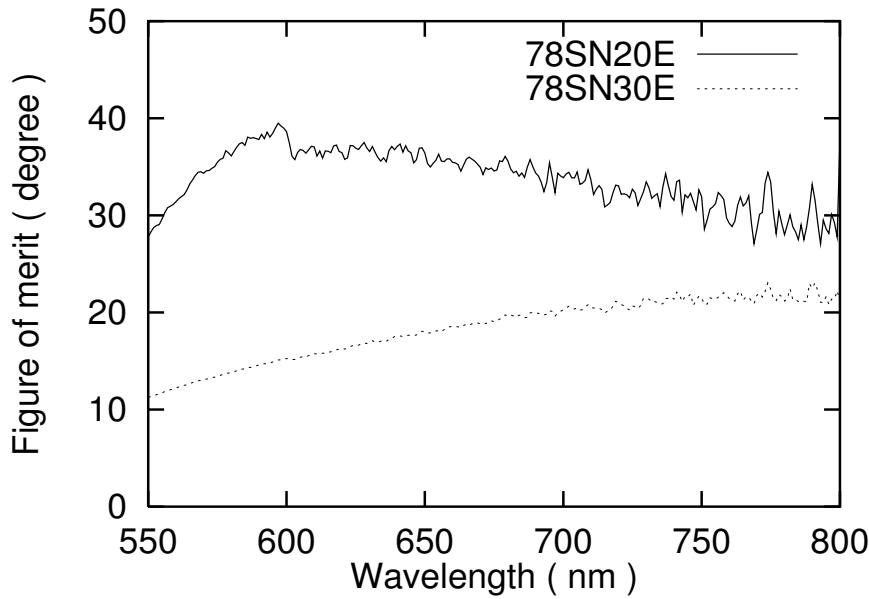Figure 5.8: Optical absorption spectra for 78SN20E and 78SN30E glasses.

Figure 5.9: Magneto-optical figure of merit for 78SN20E and 78SN30E glasses in a wavelength range of 500 to 800 nm.

spectra for 78SN20E and 78SN30E glasses. No absorption peak is recognized in the wavelength region longer than 550 nm. The intense band at around 500 nm is ascribed to the $4f^7 \rightarrow 4f^6 5d$ transition of Eu^{2+}. From the data of optical absorption in Fig. 5.8 and the Faraday rotation angle, the magneto-optical figure of merit was calculated. The results are shown in Fig. 5.9. The magneto-optical figure of merit for 78SN20E glass is about 30 to 40° in the wavelength range between 550 to 800 nm, which is obtained under the applied external magnetic field of 15 kOe. This value is about 10 times and 1.5 times larger than the magneto-optical figure of merit for $Y_3Fe_5O_{12}$ and $Gd_2BiFe_5O_{12}$ crystals in this wavelength range, respectively. The magneto-optical figure of merit of 78SN30E glass is smaller than that of 78SN20E glass because of the somewhat larger absorbance. Nonetheless, the magneto-optical figure of merit

of 78SN30E glass excells that of $Y_3Fe_5O_{12}$ crystal.

5.2.5   Conclusion

The relationship between local structure and Faraday effect of sodium borate
and alkali silicate glasses containing a large amount of Eu^{2+} ions was clar-
ified. The effective transition wavelength calculated using Van Vleck-Hebb
theory increases monotonically with an increase in the isomer shift of ^{151}Eu
Mössbauer spectrum. This phenomenon suggests that the splitting of the $5d$
levels of Eu^{2+} increases with an increase in the electron density of oxide ions,
leading to the longer wavelength of the transition from the $4f$ ground state
to the lowest $5d$ level. The electron density of oxide ions around an Eu^{2+} ion
is higher in the alkali silicate glasses than in the sodium borate glasses. As a
result, the effective transition wavelength of the $4f^7 \rightarrow 4f^6 5d$ transition which
causes the Faraday effect of Eu^{2+} in the alkali silicate glasses becomes longer.
Besides, the effective transition probability for the $4f^7 \rightarrow 4f^6 5d$ transition is
higher in the alkali silicate glasses compared with the sodium borate glasses.
Both the long effective transition wavelength and high effective transition prob-
ability bring about the large magnitude of Verdet constant of the alkali silicate
glasses. The optical absorption of these glasses is low in the wavelength range
of 550 to 800 nm. Consequently, the glasses possess a large magneto-optical
figure of merit in this wavelength range.

References

[1] J. F. Dillon, Jr., J. Appl. Phys. **39**, 922 (1968).

[2] H. Takeuchi, Jpn. J. Appl. Phys. **39**, 1903 (1975).

[3] C. B. Rubinstein, S. B. Berger, L. G. V. Uitert, and W. A. Bonner, J. Appl. Phys. **35**, 2338 (1964).

[4] S. B. Berger, C. B. Rubinstein, C. R. Kurkjian, and A. W. Treptow, Phys. Rev. **133**, A723 (1964).

[5] L. D. Pye, S. C. Cherukuri, J. Mansfield, and T. Loretz, J. Non-Cryst. Solids **56**, 99 (1983).

[6] V. Letellier, A. Seignac, A. L. Floch, and M. Matecki, J. Non-Cryst. Solids **111**, 55 (1989).

[7] J. T. Kohli and J. E. Shelby, Phys. Chem. Glasses **32**, 109 (1991).

[8] G. T. Petrovskii, I. S. Edelman, T. V. Zarubina, A. V. Malakhovskii, V. N. Zabluda, and M. Y. Ivanov, J. Non-Cryst. Solids **130**, 35 (1991).

[9] J. Qiu, K. Tanaka, and K. Hirao, J. Am. Ceram. Soc. **80**, 2696 (1997)

[10] M. W. Shafer and J. C. Suits, J. Am. Ceram. Soc. **49**, 261 (1966).

[11] J. Shoenes, E. Kaldis, W. Thöni, and P. Wachter, Phys. Status Solidi A **51**, 173 (1979).

[12] J. Qiu, K. Tanaka, N. Sugimoto, and K. Hirao, J. Non-Cryst. Solids **213-214**, 193 (1997).

[13] D. R. MacFarlane, C. R. Bradbury, P. J. Newman, and J. Javorniczky, J. Non-Cryst. Solids **213-214**, 199 (1997).

[14] J. H. V. Vleck and M. H. Hebb, Phys. Rev. **46**, 17 (1934).

[15] J. Qiu, Y. Iwabuchi, and K. Hirao, Phys. Chem. Glasses **38**, 66 (1997).

Summary

In the present thesis, optical properties of rare-earth ions in oxide glasses were investigated by means of high-resolution spectroscopies such as persistent spectral hole burning and fluorescence line narrowing technique. Besides, local structure, magneto-optical properties and correlation between them of oxide glasses containing divalent rare-earth ions were examined utilizing the measurements of ^{151}Eu Mössbauer and Faraday effects. The results obtained are summarized as follows.

In General introduction, the general background and purpose of the present study were outlined. Some interesting phenomena and experimental results of rare-earth ions in inorganic glasses were reviewed and the unresolved problems concerning the local structure and the optical and magneto-optical properties were described.

In Chapter 1, the sodium borate and alkali silicate glasses containing Eu^{2+} ions were prepared under a reducing atmosphere and ^{151}Eu Mössbauer effect measurements were performed at room temperature for these glasses to examine the chemical state of Eu^{2+} ions as well as the fraction of the number of Eu^{2+} ions in the total number of europium ions. For the sodium borate glasses, the Mössbauer spectra indicated that most of the europium ions are present as a divalent oxidation state. In dilute Eu^{2+} -containing borate glasses, spectra were split due to paramagnetic hyperfine interactions in the glasses with low and high sodium contents. In condensed Eu^{2+} -containing borate glasses, line broadening resulted from the contribution of quadrupole splitting due to

asymmetrical oxygen coordination around an Eu^{2+} ion and the contribution of inhomogeneous broadening due to site-to-site variation. The compositional dependence of isomer shift and quadrupole interaction was related with the structural changes in borate glass. The variation of isomer shift correlated well with the optical basicity of glass, and the trend was explained in terms of the covalent admixture with $6s$ character. As for the alkali silicate glasses, the Mössbauer spectra revealed that about 80 % of europium ions are present as the divalent oxidation state. The isomer shift and quadrupole interaction for the alkali silicate glasses were larger than those for the borate glasses with low sodium contents. This fact was explained by considering that Eu^{2+} ions incorporated into the silicate glass break the Si-O-Si bonds and create non-bridging oxygens. The $Eu-O$ bond in the alkali silicate glasses along with the sodium borate glasses was more ionic than that in $EuTiO_3$ or $EuZrO_3$, where the oxygen coordination number for Eu^{2+} is twelve. Therefore the average coordination number for Eu^{2+} in the present oxide glasses was estimated to be twelve, indicating that Eu^{2+} ions act as a network modifying cation.

In Chapter 2, a fluorescence line narrowing technique was carried out for sodium borate glasses containing Sm^{2+} and its isoelectronic Eu^{3+} ions under a pulsed tunable dye laser excitation. In order to obtain site-dependent information, measurements were made by exciting the inhomogeneously broadened $^5D_0 - {}^7F_0$ transition at 10 K. Not only the line-narrowing fluorescence of $^5D_0 \rightarrow {}^7F_1$ transition but also the temporal changes of the emission lines were investigated as a function of excitation energy, and the dynamics of excited states for both ions were compared with each other. As a result, the site-to-site variations of the inhomogeneously broadening of $^5D_0 - {}^7F_0$ transitions were attributed to the apparent difference in the local structure between Sm^{2+} and Eu^{3+} ions doped in borate glasses with Na_2O contents from 10 to 20 mol%. Also, a decrease in concentration of rare-earth ion caused a more significant

effect on the Eu^{3+} ion than on the Sm^{2+} ion at high-excitation energy. Based on the phenomenon, it was concluded that the difference in the local environment between Sm^{2+} and Eu^{3+} ions is mainly ascribable to the difference in the valence and ionic radius.

In Chapter 3, hole-burning spectroscopy was carried out for glasses with compositions of $(75-x)SiO_2 \cdot xAlO_{3/2} \cdot 25NaO_{1/2} \cdot 1.0EuO_{3/2}$ ($x = 0$, 10, 15, 20, 25, 35) in cation ratio. Persistent hole was burned in the $^5D_0 - ^7F_0$ transition of Eu^{3+} at temperatures between 4.2 and 20 K in aluminosilicate glasses, while the hole burning was not observed above 4.2 K in silicate glass. In other words, the introduction of Al^{3+} ion in silicate glass promoted the formation of stable hole. The hole was stable for more than 1 h and was accompanied with no antiholes, suggesting that the persistent hole burning occurred by an optically induced rearrangement of local structure around Eu^{3+}. Besides, the homogeneous linewidth showed a T-linear dependence between 4.2 and 8 K and a nearly T^2-dependence at $T > 8$ K. The temperature dependence of homogeneous linewidth was explained both by the Raman process involving localized vibrations and by the dynamical process associated with low-energy excitations like two-level system.

Also, the hole-burning spectroscopy was applied to the $^1D_2 - ^3H_4$ transition of Pr^{3+} in binary sodium silicate glasses, and the effect of Na_2O on the persistent spectral hole burning was investigated systematically. The homogeneous linewidth showed a nearly T-linear dependence irrespective of glass composition below about 10 K, characteristic of phase relaxation due to the dynamical process associated with low-energy excitations in glasses. The homogeneous linewidth increased with an increase in Na_2O content at 4.2 K. On the contrary, the fluorescence lifetime for the $^1D_2$ state of Pr^{3+} was independent of Na_2O content. Namely, the variation of homogeneous linewidth with the compositions of sodium silicate glasses is not attributed to the change of static crystal

field around Pr^{3+} but is influenced by the density and property of low-energy excitation modes in the glass structure. The hole-burning efficiency increased with the increase in Na_2O content as well. These results were interpreted by assuming that the low-energy excitation modes originating from Na^+ and/or nonbridging oxygen adjacent to Na^+ contribute to the optical dephasing and persistent spectral hole burning.

In Chapter 4, the conditions for the possibility of high-temperature persistent spectral hole burning were examined for Eu^{3+} -doped silicate glasses. The persistent spectral hole burning was observed at 77 to 300 K for $^5D_0 - {}^7F_0$ transition of Eu^{3+} in silicate and aluminosilicate glasses melted in a nitrogen atmosphere. The spectral hole was undiminished in intensity for 2 h in the dark. On the other hand, the persistent spectral hole burning was not observed above 77 K when the glasses were melted in air. In other words, the formation of hole with high thermal stability was accomplished only by a change in the melting atmosphere. A novel and striking result was that the persistent hole was burned at room temperature; the room-temperature persistent hole burning was observed for the first time in Eu^{3+} -doped organic and inorganic materials. ^{151}Eu Mössbauer spectra indicated that both Eu^{3+} and Eu^{2+} ions exist in the glasses prepared under a nitrogen atmosphere. As for the glasses melted in air, almost all of europium ions were present as Eu^{3+} ions. In addition to these results, the studies on erasure of the persistent hole led to suggestions that hole burning occurs by photoinduced reduction of Eu^{3+} to Eu^{2+} and that the positive hole generated by photoreduction is trapped by Eu^{2+} which is present in the glasses prepared in a nitrogen atmosphere.

In Chapter 5, the wavelength dependence of the Verdet constant in the visible range was determined at room temperature for sodium borate and alkali silicate glasses containing a large amount of Eu^{2+} ions. The effective transition wavelength and effective transition probability were calculated based on the

theory derived by Van Vleck and Hebb. The effective transition wavelength correlated well with the isomer shift of ^{151}Eu Mössbauer spectrum. The ^{151}Eu Mössbauer spectra revealed that the $6s$ electron density is higher in the alkali silicate glasses than in the sodium borate glasses. The high electron density leads to the large splitting of $5d$ orbitals of Eu^{2+}. As a result, the effective transition wavelength of the $4f^7 \rightarrow 4f^6 5d$ transition which brings about Faraday effect of Eu^{2+} became rather long in the alkali silicate glasses. In addition to the long effective transition wavelength, the high effective transition probability was found to contribute to the large magnitude of Verdet constant of the alkali silicate glasses. The optical absorption was low in the wavelength range of 550 to 800 nm. Consequently, large magneto-optical figures of merit in the visible range were realized in the alkali silicate glasses containing a large amount of Eu^{2+} ions.

List of publications

Chapter 1

"Mössbauer Spectroscopy of Borate Glasses Containing Divalent Europium Ions",

K. Fujita, K. Tanaka, K. Hirao and N. Soga,

J. Am. Ceram. Soc. **81**, 1845-1851 (1998).

Chapter 2

"Fluorescence Line Narrowing Spectroscopy of Sm^{2+} and Eu^{3+} in Sodium Borate Glasses",

K. Fujita, K. Tanaka, K. Hirao and N. Soga,

J. Appl. Phys. **81**, 924-930 (1997).

Chapter 3

"Persistent Spectral Hole Burning of Eu^{3+} Ions in Sodium Aluminosilicate Glasses",

K. Fujita, K. Hirao, K. Tanaka, N. Soga and H. Sasaki,

J. Appl. Phys. **82**, 5114-5120 (1997).

"Persistent Spectral Hole Burning of Eu^{3+} Ions in Silicate Glasses",

K. Fujita, K. Hirao, K. Tanaka, N. Soga and H. Sasaki,

Jpn. J. Appl. Phys. **37**, 1, 2267-2270 (1998).

"**Effect of Sodium Ion on Persistent Spectral Hole Burning in Pr^{3+}-Doped Silicate Glasses**",

K. Fujita, K. Tanaka, K. Hirao and H. Sasaki,

submitted to Phys. Rev. B

Chapter 4

"**Room-Temperature Persistent Spectral Hole Burning of Eu^{3+} in Sodium Aluminosilicate Glasses**",

K. Fujita, K. Tanaka, K. Hirao and N. Soga,

Opt. Lett. **23**, 543-545 (1998).

"**High-Temperature Persistent Spectral Hole Burning of Eu^{3+} Ions in Silicate Glasses: New Room-Temperature Hole-Burning Materials**",

K. Fujita, K. Tanaka, K. Hirao and N. Soga,

J. Opt. Soc. Am. B **15**, 2700-2705 (1998).

Chapter 5

"**Faraday Effect of Sodium Borate Glasses Containing Divalent Europium Ions**",

K. Tanaka, K. Fujita, N. Soga, J. Qiu and K. Hirao,

J. Appl. Phys. **82**, 840-844 (1997).

"**Large Faraday Effect and Local Structure of Alkali Silicate Glasses Containing Divalent Europium Ions**",

K. Tanaka, K. Fujita, N. Matsuoka, K. Hirao and N. Soga,

J. Mater. Res. **13**, 1989-1995 (1998).

Related publications

"Photochemical Hole Burning and Local Structural Changes in Sm^{2+} -Doped Borate Glasses",

D. H. Cho, K. Hirao, K. Fujita and N. Soga,

J. Am. Ceram. Soc. **79**, 327-332 (1996).

"The Faraday Effect and Magneto-Optical Figure of Merit in the Visible Region for Lithium Borate Glasses Containing Pr^{3+}",

K. Tanaka, N. Tatehata, K. Fujita and N. Soga,

J. Phys. D **31**, 2622-2627 (1998).

"Full Color Triboluminescence of Rare-Earth -Doped Hexacelsian $(BaAl_2Si_2O_8)$",

T. Ishihara, K. Tanaka, K. Fujita, K. Hirao and N. Soga,

Solid State Commun. **107**, 763-767 (1998).

Proceedings of International Conference

"Room-Temperature Persistent Hole Burning of Sm^{2+} in Aluminoborate Glasses",

K. Hirao, K. Fujita, D. H. Cho and N. Soga,

Proceedings of International Symposium on Optical Memory, 9-10 (1994).

"Room Temperature Operation of Photo-Chemical Hole Burning",

D. H. Cho, K. Hirao, K. Fujita and N. Soga,

Proceedings of Fifth Optoelectronics Conference, 442-443 (1994).

"Persistent Spectral Hole Burning of Eu^{3+} Ions in Silicate Glasses",

K. Hirao, K. Fujita, K. Tanaka, N. Soga and H. Sasaki,

Proceedings of Joint Magneto-Optical Recording International Symposium and International Symposium on Optical Memory, 152-153 (1997).

Acknowledgments